Phase transitions in the early universe

Michael Nee
Keble College
University of Oxford

This dissertation is submitted for the degree of
Doctor of Philosophy in Theoretical Physics

Trinity 2023

Abstract

Phase transitions are a generic prediction of models in particle physics. In the Standard Model, for example, there are two phase transitions: the QCD confinement transition and the electroweak phase transition, both occurring in the very early stages of the universe. Many extensions to the Standard Model predict new phase transitions, all occurring at very high temperatures. Depending on how these transitions proceed they may lead to signatures which can be detected today, offering a way to probe the early stages of the universe.

This thesis is on phase transitions and their impacts on early universe cosmology. Chapter 1 is an overview of the physics of phase transitions, both in the Standard Model and extensions of it. The different phases of gauge theories are described before discussing the phase transitions in the Standard Model and general features of phase transitions in theories beyond the Standard Model. The cosmological implications of these transitions is then summarised, with a focus on the production of topological defects, the gravitational wave signal and constraints from supercooling.

Chapter 2 focuses on the confining transition in Randall-Sundrum models. The transition places severe cosmological constraints on the model, meaning the model is only marginally under parametric control as an effective field theory. In this chapter a mechanism is presented which circumvents the problematic phase transition by making the confined phase metastable at high temperatures. The phenomenological features of the model, in particular dark matter production, are also presented in this chapter.

Everyday phase transitions are often catalysed by the presence of defects or impurities in the material, leading to an enhanced transition rate. In cosmology, however, phase transitions are typically considered to proceed from a homogeneous initial state. In chapter 3 the possibility that magnetic monopoles could act as catalysts for cosmological phase transitions is considered, and an algorithm developed to solve the field equations describing the transition. A similar idea is pursued in chapter 4 for the case of domain walls catalysing the electroweak phase transition.

Acknowledgements

I would primarily like to thank my supervisor, Prateek Agrawal, for his guidance and supervision over the last few years. Much of what I have learnt can be attributed to him, and working together has broadened my perspective on what it means to be a physicist. I would also like to thank the theory group at Oxford for many interesting discussions and for making it an enjoyable place to work. I am also grateful to family and friends for their support and encouragement over the years.

Statement of Originality

This thesis is the work of the author unless otherwise stated. No part has been submitted for any other qualification. Chapter 1 is an original review of the relevant scientific literature, while Chapter 2 is based partially on the collaborative work:

P. Agrawal, M. Nee, *Avoided Deconfinement in Randall-Sundrum Models, JHEP 2021, 105 (2021)*

Some sections of Chapter 2 are based on the manuscript:

M. Nee, *Meso-tuned WIMPs and Avoided Deconfinement, submitted for publication*

Chapters 3 and 4 are based respectively on the collaborative works:

P. Agrawal, M. Nee, *The Boring Monopole, SciPost Phys. 13, 049 (2022)*

P. Agrawal, S. Blasi, A. Mariotti, M. Nee, *Domain Wall Catalysed Electroweak Phase Transition, unsubmitted*

Contents

Chapter 1

Introduction

Theories in particle physics are defined by a gauge group and a spectrum of particles, with interactions that may be restricted by the imposition of global symmetries. However, often this information alone is inadequate to describe the phenomenology of the model. An example of this is the Standard Model (SM) itself. The SM is based on the gauge group $SU(3)_c \times SU(2)_{\text{ew}} \times U(1)_Y$ and the fermion spectrum consists of three generations of leptons and quarks. However, at low energies the particles we observe are the electrons and hadrons which interact via the gauge group $U(1)_{\text{em}}$. The electroweak gauge bosons are too heavy to be seen outside of colliders and the quarks and gluons are hidden from the low energy observer.

The resolution to the apparent discrepancy between the fundamental degrees of freedom and the observed world comes from the low energy phases of the SM. Quantum chromodynamics (QCD) is in the confined phase, meaning that quarks and gluons are bound into colour-neutral hadrons, while the electroweak sector is higgsed, generating masses for the weak gauge bosons and fermions of the SM. Electromagnetism is in the coulomb phase, leading to the long-range electromagnetic force between charged particles.

This situation changes at high temperatures – QCD deconfines at $T \sim 100$ MeV and gluons and quarks interact as free particles, while electroweak symmetry is restored at $T \sim 100$ GeV and the SM becomes massless. This is an expectation for theories beyond the Standard Model (BSM) as well, in general a theory appears very different at high temperatures. Such high temperatures aren't seen in the universe today, even in extreme astrophysical environments, but were almost certainly reached during the early universe.

Cosmological observations, particularly of the cosmic microwave background (CMB), indicate that the early universe was described by a homogeneous and isotropic distribution of matter and radiation. Moreover, the SM was in near-perfect thermal equilibrium at the time of the CMB. Extrapolating backwards in time indicates the early universe was described by a thermal state, with increasing temperature as we look further back. The high temperatures reached mean that new physics at high scales, inaccessible to current experiments, almost certainly played a role during the early universe.

This also means there are two phase transitions which occur in the SM alone. There are also many theories beyond the standard model (BSM) which lead to phase transitions which would also play a role in cosmology. Non-abelian gauge theories which are asymptotically free will confine at some scale if they are not higgsed, grand unified theories (GUTs) [1–3] are higgsed to the SM at a high scale and global symmetries may also be spontaneously broken, such as the Peccei-Quinn symmetry in axion models [4, 5]. For the model to be consistent with experiments these phase transitions typically need to occur at scales of order the electroweak scale or above.

The rate at which the phase transition proceeds largely determines the phenomenological consequences of the transition. In theories of electroweak baryogenesis [6] the rate strongly influences the final baryon asymmetry, while in Randall-Sundrum models [7] the rate of the confining transition must be sufficiently rapid to avoid an eternally inflating phase [8], leading to strong bounds on the model. These phase transitions occur around the TeV scale and lead to a potentially observable gravitational wave signal with features that depend strongly on the phase transition rate [9, 10]. The study of phase transitions and their signatures can tell us about theories at scales which we have no way of accessing at colliders.

This chapter begins by discussing the SM and the low energy phases of the SM. Section 1.2 is a basic overview of early universe cosmology and a discussion of some of the indications cosmological observations give us about new physics relevant during the early universe. The details of the phase transitions in the SM are discussed in section 1.3, while phase transitions more generally are discussed in section 1.4. In section 1.5 the possible consequences of early universe phase transitions are discussed.

1.1 The Standard Model

The SM describes the interactions of all the fundamental particles that are known to exist. The theory is based on the gauge group $SU(3)_c \times SU(2)_{\text{ew}} \times U(1)_Y$, a fermion spectrum consisting of three families of quarks and leptons and the higgs doublet. The Lagrangian defining the SM is given by

$$\begin{aligned}\mathcal{L}_{\text{SM}} = &-\frac{1}{4g_s^2}\,\text{tr}\,G_{\mu\nu}G^{\mu\nu} - \frac{1}{4g^2}\,\text{tr}\,W_{\mu\nu}W^{\mu\nu} - \frac{1}{4g'^2}B_{\mu\nu}B^{\mu\nu} \\ &+ D_\mu H^\dagger D^\mu H - V(H) \\ &+ \sum_{j=1}^{3} i\bar{L}^j \not{D} L^j + i\bar{l}^j \not{D} l^j - \sum_{k=1}^{3} Y_l^{jk}\bar{L}^j H l^k \\ &+ \sum_{j=1}^{3} i\bar{Q}^j \not{D} Q^j + i\bar{u}^j \not{D} u^j + i\bar{d}^j \not{D} d^j - \sum_{k=1}^{3} Y_u^{jk}\bar{Q}^j \tilde{H} u^k - Y_d^j \bar{Q}^j H d^k\,.\end{aligned} \tag{1.1}$$

In equation (1.1):

- the first line describes the gauge field strengths, with g_s, g, g' are the gauge couplings of $SU(3)_C, SU(2)_{\text{ew}}$ and $U(1)_Y$ respectively;

- the second line is the Lagrangian for the higgs, with scalar potential V:

$$V(H) = \lambda\left(H^\dagger H - \frac{1}{2}v_{\text{ew}}^2\right)^2\,; \tag{1.2}$$

- the third line describes the leptons, where j labels the generation, L is the lepton doublet and l the right-handed singlets, Y_l is the lepton yukawa matrix;

- similarly, the fourth line describes the quarks, j again labels the generation, Q is the quark doublet and u, d the $SU(2)$ singlet up-and down- type quarks, Y_u and Y_d are the respective yukawa matrices;

- the covariant derivatives are $D_\mu\phi = \left(\partial_\mu + i\sum_a t^a A_\mu^a\right)\phi$, where t^a is the generator for the representation of the gauge group ϕ transforms under[1], with A_μ^a the associated gauge field.

[1]Here ϕ refers to an arbitrary field, not necessarily a scalar.

At first glance, the Lagrangian (1.1) appears to have very little to do with the real world. Almost all of the visible sector today is in hadrons (protons and neutrons), which don't appear in (1.1), as well as electrons. They interact via the electromagnetic force and all have mass, despite there being no explicit masses in (1.1). Gluons and quarks are not observed as free particles and the weak and hypercharge interactions are also obscure at low energies due to the masses of the electroweak gauge bosons. The resolution to the discrepancy between the degrees of freedom appearing in (1.1) and the world around us comes from identifying the low energy phases of the SM.

1.1.1 Low temperature phases of the SM

The different phases of the SM gauge groups lead to different forces between charged particles. Electromagnetism leads to a long-range force which falls as r^{-2}, the weak interactions are short-ranged and the strong interactions are unobservable at low energies as the observable states are colour-neutral bound states – the baryons and mesons. The explanation for this is that each gauge sector is in a different phase, causing them to appear very different from each other. A summary of the potential generated between two (electrically) charged particles in each of the phases relevant for this thesis is [11]:

Phase	Potential
Coulomb	$V(r) \propto \frac{1}{r}$
Higgsed	$V(r) \propto c + \frac{e^{-mr}}{r}$
Confined	$V(r) \propto r$

where c is a constant and m is the mass of the gauge field in the higgsed phase.

Phases are distinguished by an order parameter ϕ, a field whose expectation value vanishes in one phase and is non-zero in the other. If the order parameter transforms in a representation R of a global symmetry group G, $\phi \to \phi' = R(g)\phi$, then in the $\phi = 0$ phase the symmetry is manifest, while in the $\phi \neq 0$ phase the symmetry is not respected by the ground state and is said to be spontaneously broken. The symmetry also implies that ϕ, ϕ' are degenerate vacuum states. This leads to the existence of massless goldstone modes, which parametrise fluctuations along the ground state of the potential.

The same language can be used to describe gauge theories in the higgsed phase, where the order parameter is a scalar field in a representation of the gauge group. The difference is that ϕ and ϕ' represent the same state if related by a gauge transformation, so there

is only one physically distinct vacuum state. This means there are no massless goldstone modes, in contrast to the case of a broken global symmetry. A robust consequence of higgsing is the generation of mass terms for gauge bosons

$$M_{ab}^2 A_\mu^a A^{b,\mu} = A_\mu^a A^{b,\mu} t_{np}^a t_{pm}^b \phi_n \phi_m \,, \tag{1.3}$$

where t^a are the symmetry generators of the gauge group, and A_μ^a the associated gauge fields. The gauge boson masses in the higgsed phase leads to the exponential fall off in the force between charged particles at large distances.

Electroweak Theory

The order parameter for the electroweak sector of the SM is the higgs doublet, H, which is in the $(\mathbf{1}, \mathbf{2}, 1/2)$ representation of the SM gauge group. The tree-level higgs potential is given in equation (1.2) and is minimised for $\langle H \rangle = \frac{1}{\sqrt{2}} (0 \quad v_{\rm ew})^T$ (in unitary gauge). The resulting mass terms for the electroweak gauge bosons are

$$\mathcal{L}_{\rm mass} = \frac{1}{4} \left(g \tau^a W_\mu^a \langle H \rangle + g' B_\mu \langle H \rangle \right)^\dagger \left(g \tau^b W^{b,\mu} + g' B^\mu \right) \langle H \rangle \tag{1.4}$$

where τ^a are the Pauli matrices which generate $SU(2)$. In terms of the mass eigenstates this becomes:

$$\mathcal{L}_{\rm mass} = \frac{g^2 v_{\rm ew}^2}{4} W_\mu^+ W^{-\mu} + \frac{(g^2 + g'^2) v_{\rm ew}^2}{8} Z_\mu Z^\mu \tag{1.5}$$

with the photon, A_μ, remaining massless. The overall pattern of higgsing is $SU(2)_{\rm ew} \times U(1)_Y \to U(1)_{\rm em}$, where the combination of generators $T_3 + Y$ is unbroken by the higgs expectation value (vev) and corresponds to electric charge [12].

As the $W^\pm$ and Z gauge bosons are massive they induce a yukawa-type potential between charged fermions

$$V_{\rm yuk} \sim \frac{e^{-Mr}}{r} \,, \tag{1.6}$$

while the photon leads to a long range force described by the coulomb potential

$$V_{\rm coul} \sim \frac{e^2}{r} \,. \tag{1.7}$$

Furthermore, due to the yukawa terms in the SM Lagrangian, the fermion fields ψ also gain a mass from the higgs, given by

$$m_\psi = \frac{y_\psi}{\sqrt{2}} v_{\rm ew} \,. \tag{1.8}$$

This explains why the SM fermions are massive despite there being no explicit mass terms in equation (1.1), with the hierarchies in masses inherited from hierarchies in the yukawa couplings.

QCD: Confinement and Chiral Symmetry Breaking

It is less clear how to proceed with QCD. The low energy states of the QCD sector are the baryons and mesons, which are all neutral under $SU(3)_c$, indicating that colour charges are confined. The description of the confined phase is complicated by the fact that there is no fundamental field which serves as an order parameter for confinement and the QCD coupling, $\alpha_s = g_s^2/4\pi$, is large in the IR, taking us outside the regime where perturbation theory is valid. This can be seen from the 1-loop β-function for the coupling in an $SU(N)$ gauge theory:

$$\beta(\alpha_s) = \frac{\partial \alpha_s}{\partial \log \mu} = -\frac{\alpha_s^2}{2\pi}\left(\frac{11N}{3} - \frac{2n_f}{3}\right) , \tag{1.9}$$

where n_f is the number of quark flavours with masses below the scale μ. For QCD $N = 3, n_f \leq 6$, and the β-function is negative, indicating that α_s grows at low energies and ultimately diverges at a scale $\Lambda_{\rm QCD} \sim 200$ MeV. The low energy phase of QCD is therefore governed by strong coupling dynamics. While the details of low energy QCD are less precisely known than for the electroweak sector, some statements can still be made about the confined phase.

The potential that leads to confining behaviour is:

$$V(r) = \sigma r \,, \tag{1.10}$$

where σ is the string tension. Conceptually, this is due to the field lines of the gluons forming a flux tube between a pair of quarks, as shown in figure 1.1. The energy in the flux tube (or string) grows linearly with its length, leading to the potential (1.10). If we imagine pulling two quarks (or a quark and antiquark) away from each other, at

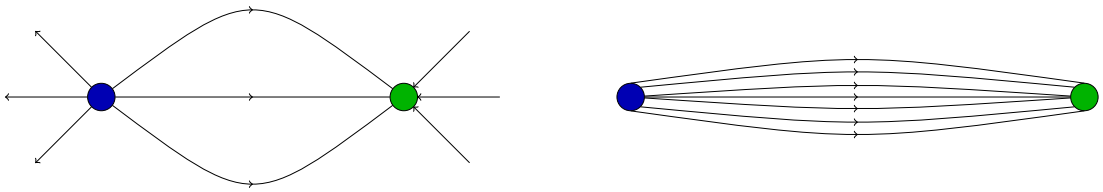

Figure 1.1: Field lines between charges in the coulomb phase (left) and the confined phase (right). In the confined phase the field strength is confined to a cylindrical region stretching between the two charges.

distances $r \gtrsim 2m_q/\sigma$ there is enough energy between the pair to produce a quark/antiquark pair from the vacuum, explaining why a potential of the form (1.10) implies that only colour-neutral bound states are observed.

The order parameter for confinement is only well-defined in the case where there are no light quarks. In this case, we can define the Wilson loop W as the integral of the gluon field A^a_μ around a closed contour C [13]:

$$W(C) = \mathrm{tr} \exp\left(\oint_C igt^a A^a_\mu dx^\mu\right) . \tag{1.11}$$

The exponent of the Wilson loop can be thought of as the field generated by an infinitely heavy probe quark/antiquark pair which are created in vacuum, travel along separate paths, then are annihilated at a later time. In the confined phase there is a flux tube which connects the two quarks implying that the field lines are constant across the area of the minimal surface bounded by C, leading to the area law for the confined phase

$$W(C) \propto e^{-\sigma A} . \tag{1.12}$$

In the higgs phase, by contrast, the field lines decay exponentially away from the probe quarks, leading to a perimeter law for the Wilson loop

$$W(C) \propto e^{-\Lambda P} , \tag{1.13}$$

so the asymptotic behaviour of Wilson loops distinguishes between the phases of the theory.

At finite temperature we can define a local order parameter by considering Wilson loops which vary in the euclidean time direction, known as Polyakov loops [14]:

$$P = \mathrm{tr} \exp\left(\int_0^\beta d\tau igt^a A^a_0(\tau, \vec{x})\right) , \tag{1.14}$$

where $\tau \sim \tau + \beta$ and β is the inverse temperature. The expectation value of the Polyakov loop is related to the free energy F of adding a single probe quark to the vacuum, $\langle P \rangle \sim e^{-\beta F}$. In the confined phase, $F \to \infty$ so $\langle P \rangle = 0$, while in the deconfined phase the energy cost of creating a free quark is finite, so $\langle P \rangle \neq 0$.

The symmetry which is broken by the vev of P is the $\mathbb{Z}_N$ centre symmetry. Under a gauge transformation $\Omega(\tau, \vec{x})$ such that

$$A^a_\mu \to \Omega^{-1} A^a_\mu \Omega + \Omega^{-1} \partial_\mu \Omega \,, \tag{1.15}$$

we have:

$$\exp\left(\int_0^\beta d\tau i g t^a A^a_0(\tau, \vec{x})\right) \to \Omega^{-1}(\beta, \vec{x}) \exp\left(\int_0^\beta d\tau i g t^a A^a_0(\tau, \vec{x})\right) \Omega(0, \vec{x}) \,. \tag{1.16}$$

Because of the trace in equation (1.14), P is gauge invariant for periodic gauge transformations $\Omega(\beta, \vec{x}) = \Omega(0, \vec{x})$. However, we can also consider gauge transformations which are twisted by an element c of the centre of the gauge group[2] $\Omega(\beta, \vec{x}) = c\Omega(0, \vec{x})$. Then $P \to cP$, so the deconfined phase spontaneously breaks the centre symmetry which is restored in the confined phase.

The use of the Polyakov loop as an order parameter for confinement breaks down when there are lights quarks, as is the case for QCD. This is because for a large Wilson loop there is sufficient energy to create a quark/antiquark pair from the vacuum, thus 'breaking' the Wilson loop, recovering the perimeter law in the confined phase and restoring a non-zero expectation value for P. The intuitive picture of strings binding together coloured particles is still expected to hold, however.

In addition to quark confinement, the low energy phase of QCD also breaks the chiral symmetry of the quark sector. The QCD Lagrangian if we neglect the yukawa couplings has a global symmetry

$$G_\chi = SU(n_f)_L \times SU(n_f)_R \times U(1)_B \,, \tag{1.17}$$

where $n_f = 6$ is the number of quark flavours and $U(1)_B$ is the baryon number symmetry. Under G_χ the quark fields transform as

$$Q^j \to e^{i\alpha} L_{jk} Q^k \,, \qquad u^j \to e^{i\alpha} R_{jk} u^k \,, \qquad d^j \to e^{i\alpha} R_{jk} d^k \,, \tag{1.18}$$

[2]The centre of a group G is the set of elements which commute with all other elements of G. For the case of $SU(N)$ the centre is isomorphic to $\mathbb{Z}_N$.

where $L \in SU(n_f)_L, R \in SU(n_f)_R$ and α is a $U(1)_B$ phase. Below the electroweak scale the G_χ is explicitly broken by the quark masses. As the u, d masses are small ($m_u, m_d \ll \Lambda_{\rm QCD}$) the restriction to $n_f = 2$ case involving just the u, d quarks is only weakly broken. The $n_f = 3$ case can still be considered an approximate symmetry, although the explicit breaking due to the strange quark mass is more significant as $m_s \sim \Lambda_{\rm QCD}$.

There are general arguments which can be made to show that confinement implies G_χ must be spontaneously broken at low energies. While $SU(n_f)_L$ and $SU(n_f)_R$ are symmetries of the Lagrangian they are both anomalous. The anomaly coefficients for the $SU(n_f)_L^3$ and $SU(n_f)_L^2 \times U(1)_B$ anomalies are:

$$\mathcal{A}(SU(n_f)_L^3) = \mathcal{A}(SU(n_f)_L^2 \times U(1)_B) = N\,, \tag{1.19}$$

with the opposite sign for $L \to R$. From anomaly matching arguments these coefficients must be the same in the low energy phase as in the UV [15]. This can be seen by considering what would happen if we add massless 'spectator' fermions which cancel the anomalies involving $SU(n_f)_L$ and couple the $SU(n_f)_L$ current to a gauge field. As the spectator fermions couple only to the $SU(n_f)_L$ gauge fields and the new gauge coupling can be taken to be small, the spectator fermions don't influence the low-energy phase of the SM. Considering the effective theory below the QCD scale, the $SU(n_f)_L$ anomalies must also vanish. There there are two ways this could happen:

1. $SU(n_f)_L$ is spontaneously broken by QCD dynamics, so the $SU(n_f)_L$ gauge bosons are heavy and don't appear in the effective theory.

2. $SU(n_f)_L$ is unbroken and the anomaly produced by the spectator fermions is cancelled by some other massless fermions present in the low energy phase of QCD.

In the confined phase of QCD the only fermions are the baryons, which all have mass $m \gtrsim \Lambda_{\rm QCD}$. The second option is therefore not viable, implying that G_χ must be spontaneously broken in the confined phase of QCD.

The order parameter for the breaking of G_χ is the chiral condensate

$$\langle \bar{U}^j u^k \rangle = \langle \bar{D}^j d^k \rangle \simeq \delta^{jk} \times (200{\rm MeV})^3\,, \tag{1.20}$$

and the symmetry breaking pattern is

$$SU(n_f)_L \times SU(n_f)_R \times U(1)_B \to SU(n_f)_V \times U(1)_B \,, \tag{1.21}$$

where $SU(n_f)_V$ is the diagonal subgroup of $SU(n_f)_L \times SU(n_f)_R$. The goldstone bosons are the mesons, which are massive due to the different masses and electric charges of the quarks, both of which explicitly break $SU(n_f)_V$.

1.1.2 Symmetry Restoration

It is a general expectation is that at high temperatures symmetries are restored [16–19]. There are many examples of this in condensed matter systems, and the SM is no different. To see this for the electroweak sector, we notice that the free energy of a relativistic species $m \ll T$ is given by

$$F_B = -\frac{\pi^2 T^4}{90} + \frac{m^2 T^2}{24} + \dots \,, \qquad F_F = -\frac{7\pi^2 T^4}{720} + \frac{m^2 T^2}{48} + \dots \,, \tag{1.22}$$

for bosons and fermions respectively. In the SM all fields all masses are proportional to $\langle H \rangle$ so the second term in each of the above expansions contributes a $T^2 H^\dagger H$ term with positive coefficient to the effective potential for the higgs. At temperatures of order $T \sim 140\,\text{GeV}$ the $H^\dagger H$ term becomes positive and $H = 0$ is the only minimum of the potential, restoring electroweak symmetry.

These temperatures are far above the temperatures typical seen in the universe today, even in extreme environments. As discussed in the following section, the early universe is described by a thermal bath of particles at high temperature, possibly up to $T \sim 10^{16}$ GeV. This means that the SM likely underwent two phase transitions during the early parts of the universe, and depending what new physics exists and the maximum temperatures reached there could have been many more. The following section is devoted to reviewing the aspects of early universe cosmology which are most relevant for the later discussion of phase transitions.

1.2 Early Universe Cosmology

The most precise experimental probe of cosmology comes from observations of the cosmic microwave background (CMB) [20]. The CMB is a snapshot of the radiation emitted at the time of photon decoupling, and shows a universe composed of matter and radiation which is flat, homogeneous and isotropic [21]. The CMB radiation is also a near perfect blackbody spectrum, indicating that the SM was in thermal equilibrium in the early universe.

These observations strongly constrain the allowed geometry of the universe. The most general metric satisfying the properties of homogeneity, isotropy and flatness is the Friedmann-Robertson-Walker (FRW) metric:

$$ds^2 = dt^2 - a^2(t)\left(dr^2 + r^2 d\Omega\right) , \tag{1.23}$$

where $a(t)$ is the scale factor. Homogeneity and isotropy also imply that the stress tensor must be that of a perfect fluid:

$$T_{\mu\nu} = \text{diag}\left(\rho, p, p, p\right) , \tag{1.24}$$

where ρ is the energy density and p the pressure of the fluid. The equations of motion governing the system then take the form

$$H^2 \equiv \left(\frac{\dot{a}}{a}\right)^2 = \frac{8\pi}{3M_P^2}\rho\,, \qquad\qquad \dot{\rho} = 3H\left(\rho + p\right) . \tag{1.25}$$

The CMB also gives a good indication of the content of the universe at that time [22]. It depicts a universe composed of baryons, photons and dark matter (DM) with comparable energy densities, and a cosmological constant contribution that only becomes relevant at late times. As the energy density in radiation falls faster than matter with increasing a, extrapolating backwards from the CMB we expect a universe that is dominated by radiation, with energy density and hubble rate given by:

$$H = \sqrt{\frac{4\pi^3 g_*}{45}}\frac{T^2}{M_P} \qquad\qquad \rho_r = \frac{\pi^2}{30}g_*(T)T^4\,. \tag{1.26}$$

where $g_*(T)$ counts the effective number of relativistic species[3].

[3] In the SM, $g_* \sim 100$ at high temperatures and $g_* \sim 10$ just below the QCD scale, with a sharp decrease in g_* at the QCD phase transition.

A striking feature of the CMB is that the signal displays correlations between regions which appear not to have been in causal contact. This observation, combined with the observed flatness of the universe, can be explained by an initial period of exponential expansion known as inflation [23]. The basic idea of inflation is that at very early stages the universe is dominated by a cosmological constant, $\rho = \Lambda_I^4 > 0$, leading to the evolution

$$a(t) = e^{H_I t}, \quad \text{where} \quad H_I = \sqrt{\frac{8\pi}{3}} \frac{\Lambda_I^2}{M_P}. \tag{1.27}$$

The exponential expansion during this period means causally disconnected regions of the CMB were in contact during the initial stages of inflation, and also dilutes any curvature component to the energy density. In order to explain the CMB the scale factor must have grown by around a factor $\sim e^{60}$ during this period.

As particle number densities scale inversely with the volume ($\propto a^{-3}$), the universe is essentially empty during the final stages of inflation. At the end of inflation, the universe is repopulated as the energy density driving the exponential expansion decays to radiation, typically via the decay of a scalar field known as the inflaton. This sets the initial temperature of the radiation-dominated universe (or reheating temperature, T_r), which is given by[4]:

$$T_r = \left(\frac{30}{\pi^2 g_*(T_r)}\right)^{1/4} \Lambda_I. \tag{1.28}$$

The scale of inflation, Λ_I is an unknown quantity, although is bounded from above by $\sim 10^{16}$ GeV by the lack of observation of tensor modes in the CMB [24].

1.2.1 Cosmology and physics beyond the standard model

As already mentioned in passing, CMB measurements provide evidence for what lies beyond the Standard Model. Large scale correlations in the CMB require a mechanism, such as inflation, to generate the right initial conditions for the radiation dominated era, and the CMB provides evidence for the existence of dark matter and a net baryon number. Each of these phenomena require new physics beyond the standard model to explain[5]. These observations are some of the most robust evidence for new physics, and indicate that BSM physics played an important role in the early universe.

[4] Here we assume a rapid reheating process.

[5] Although the higgs boson could lead to an inflationary phase if the higgs has a large coupling to the Ricci scalar [25].

An independent experimental probe of the content of the universe is Big Bang Nucleosynthesis (BBN). The period of BBN is the earliest moment of the universe's history that we can observe, and refers to the process by which the primordial abundances of the light elements ^{3}He, ^{4}He, D and ^{7}Li are produced. These abundances depend sensitively on both the baryon asymmetry and g_* at temperatures of around $T \sim 1$ MeV, providing a good indication of the composition of the universe at this temperature. In particular, the baryon asymmetry inferred from BBN agrees with the CMB measurement, and the value of g_* is consistent with the SM prediction. This indicates that the baryon asymmetry must have been produced by some mechanism operating at temperatures at least above the MeV scale, and any additional degrees of freedom must not contribute significantly to the radiation energy density at $T \sim 1$ MeV.

Perhaps the most obvious shortcoming of the SM is that it fails to explain the existence of dark matter (DM) [22]. Observations from a range of sources – galaxy rotation curves [26], observations of the bullet cluster [27], the growth of density perturbations and measurements of CMB anisotropies – require the existence of a pressureless form of matter which has around 5 times the energy density of ordinary matter. The dominant effect of the DM in the late universe comes from its gravitational interactions, which act to hold galaxies together. In order to explain these observations the DM need not interact in any other way – either with the SM or with itself. However, the DM abundance must have been set by some mechanism at play during the early universe, meaning the particle properties of DM were important at early times.

The baryon asymmetry is another unexplained feature of the universe that points to a cosmological origin. For an asymmetry to be produced there must be interactions that violate baryon number, violate both C & CP, and occur out of equilibrium [28]. The electroweak phase transition in the SM satisfies these conditions [6, 29], however, the lack of CP violation in the SM and the fact that the electroweak phase transition is not first order (implying departures from equilibrium are small) means that the asymmetry produced within the SM alone is negligible [30]. The electroweak phase transition can be modified to better satisfy these conditions, or another mechanism may be at play.

In any case, the production of a net baryon number requires a mechanism outside the SM to operate at high temperatures.

Furthermore, models of baryogenesis are difficult to accommodate if the universe never reached temperatures above the electroweak scale. This indicates that the universe almost certainly reached temperatures high enough to be in the deconfined phase of QCD and the electroweak symmetric phase. The SM thus predicts the occurrence of two phase transitions in the early universe, although many BSM models introduce others. The following sections are devoted to describing the details of the transitions in the SM and beyond.

1.3 Phase transitions in the SM

Phase transitions are characterised by an order parameter ϕ which evolves from $\phi = 0$ in the symmetric phase to $\phi \neq 0$ in the broken phase. The critical temperature, T_c, defines the boundary between the two phases. A phase transition can be classified as either first order or a continuous transition depending on the evolution of ϕ at the critical point:

- First order phase transitions occur when close to the critical temperature there are two local minima separated by a potential barrier. As T falls below T_c the low temperature vacuum becomes the global (true) minimum of the potential, and the transition proceeds through a tunnelling process to the new minimum.

- Continuous phase transitions are defined by the absence of a potential barrier between the phases. As T falls below T_c, ϕ evolves continuously from $\phi = 0$ to a non-zero value in the broken phase. If physical parameters vary smoothly across the transition then the transition is known as a crossover, if there is a discontinuous evolution then it is termed a second order transition.

The general form of the potentials which give rise to each case are shown in figure 1.2. It turns out that in the SM, both phase transitions are crossovers [31, 32].

At the onset of a phase transition, the order parameter ϕ is correlated over a distance ξ, known as the correlation length. At large r the two-point correlation function $\langle\phi(0)\phi(r)\rangle$ decreases exponentially with a characteristic length scale given by ξ, leading to the definition

$$\xi = -\lim_{r\to\infty}\left[\frac{r}{\log\left(\langle\phi(0)\phi(r)\rangle\right)}\right]. \tag{1.29}$$

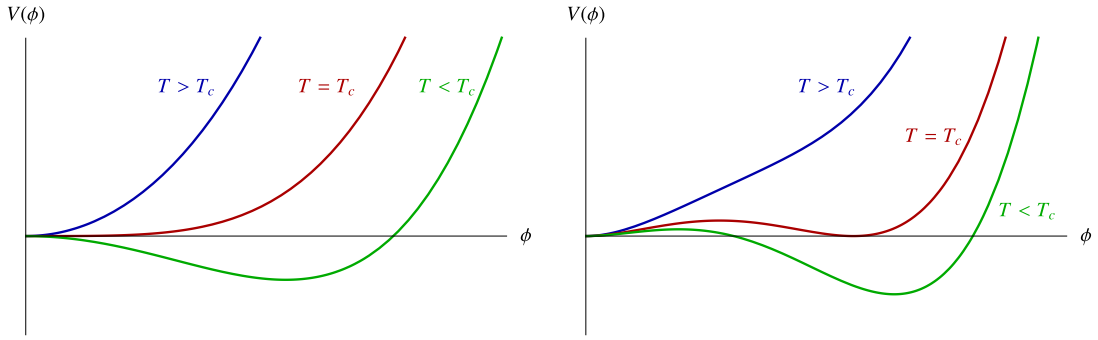

Figure 1.2: Plots show an example potential $V(\phi)$ for a continuous (left panel) and first order (right panel) transition. In both cases $\phi = 0$ is the only minimum for $T > T_c$ while at the critical temperature a new minimum appears. For a continuous transition at $T < T_c$, $\phi = 0$ becomes a maximum and there is no barrier between $\phi = 0$ and the new minimum at $\phi \neq 0$. In the first order case $\phi = 0$ is still a local minimum below T_c and there is a barrier between the two minima.

If the correlation function displays a power law dependence on the separation r then the correlation length diverges, which is behaviour characteristic of a second order phase transition. This corresponds to a massless excitation at the critical point. During a first order phase transition the correlation length remains finite throughout the transition.

1.3.1 Electroweak Phase Transition

The higgs potential receives corrections at finite temperature from all particles which couple to the higgs and are in thermal equilibrium at the time of the phase transition. To incorporate the effects of temperature on the higgs, we need to determine the 1-loop effective potential. To do this we choose a gauge where the vev. of the higgs is given by $H = \frac{1}{\sqrt{2}} \begin{pmatrix} 0 & h \end{pmatrix}^T$. In terms of h the tree level potential is

$$V(h) = \frac{\lambda}{4} \left(h^2 - v_{\text{ew}}^2 \right)^2 . \tag{1.30}$$

The corrections to V come from resumming 1-loop diagrams with n external higgs legs, to each of which we associate a power of h. The end result is

$$\Delta V = \sum_{ij} \frac{i}{2} \log \det \left[\frac{\delta^2 \mathcal{L}_{\text{SM}}(h)}{\delta \phi_i \delta \phi_j} \right] \tag{1.31}$$

where ϕ_i is a generic field (not necessarily a scalar) and $\mathcal{L}_{\text{SM}}(h)$ refers to the SM Lagrangian with the higgs field fixed to a constant value h. The corrections can be split into a temperature-independent and a finite temperature piece, leading to:

$$V_{\text{eff}}(h, T) = V_{\text{ew}}(h) + V_{\text{CW}}(h) + V_T(h, T) , \tag{1.32}$$

where the zero-temperature component $V_{\rm CW}$ is the Coleman-Weinberg potential [33]. This contribution is:

$$V_{\rm CW}(h) = \frac{1}{2}\sum_i \int \frac{d^4k}{(2\pi)^4} \log\left[k^2 + m_i^2(h)\right] \tag{1.33}$$

where the sum is over all SM species and $m_i(h)$ is the mass of field i when the higgs takes the value h. The finite temperature component is determined by Wick-rotating to euclidean signature and transforming the k^0 integral to a sum over Matsubara frequencies $\omega_n = 2\pi n/\beta$:

$$\int \frac{dk^0}{2\pi} f(k^0) \to \frac{1}{\beta}\sum_n f(\omega_n)\,, \tag{1.34}$$

ultimately leading to [34, 35]:

$$V_{\rm CW}(\phi) = \sum_i (-1)^F \frac{g_i m_i^4(\phi)}{64\pi^2}\left[\log\left(\frac{m_i^2(\phi)}{\mu^2}\right) - c_i\right]\,, \tag{1.35}$$

$$V_T(\phi) = \sum_i (-1)^F \frac{g_i T^4}{2\pi^2} J_{B/F}\left(\frac{m_i^2(\phi)}{T^2}\right)\,, \tag{1.36}$$

after removing the divergent pieces. In equations (1.35) & (1.36)

- μ is a renormalisation scale, taken to be around the electroweak scale;
- g_i is the number of internal degrees of freedom and F is the fermion number (either 1 or 0) of a species, while $c_i = 3/2$ (for scalars/fermions), $5/2$ (for vectors);
- the thermal integrals are given by:

$$J_{B/F}(x) = \int_0^\infty dy y^2 \log\left[1 \mp \exp\left(-\sqrt{x^2+y^2}\right)\right]\,. \tag{1.37}$$

The integrals (1.37) have no known closed form, but can be conveniently approximated in the high-temperature limit:

$$\begin{aligned} J_B(x \ll 1) &\simeq -\frac{\pi^2}{45} + \frac{\pi^2 x^2}{12} - \frac{\pi x^3}{6} - \frac{x^4}{32}\log\left(\frac{x^2}{\pi^2 e^{3/2-2\gamma_E}}\right)\,, \\ J_F(x \ll 1) &\simeq \frac{7\pi^4}{3600} - \frac{\pi^2 x^2}{24} - \frac{x^4}{32}\log\left(\frac{x^2}{16\pi^2 e^{3/2-2\gamma_E}}\right)\,. \end{aligned} \tag{1.38}$$

The effective potential for the higgs in the SM is shown in figure 1.3 for a range of temperatures. The results show there is no potential barrier when the temperature crosses T_c, indicating that the transition is continuous. This is confirmed by lattice studies which show that the transition in the SM is a crossover [31, 36–40].

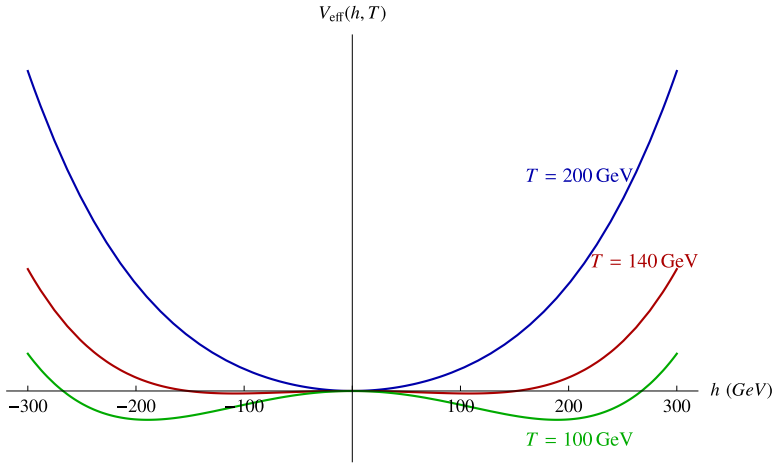

Figure 1.3: Effective potential for the radial component (h) of the higgs in the SM for temperatures $T = 200$ GeV (blue), $T = 140$ GeV (red), $T = 100$ GeV (green).

1.3.2 QCD Phase Transition

For an $SU(N)$ the order of the confinement or chiral phase transition depends both on N and the number of light quarks, n_f [41, 42]. Here we examine the phase transition for arbitrary N and n_f and specialise to the QCD case in some places. As we are interested in the regime where the low energy phase is at strong coupling, we restrict to the case where $n_f < 11N/2$ so the theory is asymptotically free.

The basic idea is to construct an effective theory for the order parameter of the phase transition (the quark condensate for the chiral transition and the Polyakov loop for the confinement transition) and analyse the renormalisation group flow of the couplings. If there is a stable fixed point for the couplings in the IR then in general the phase transition will be continuous, while if there is no stable fixed point the transition is believed to be first order, although there are exceptions to this rule [43]. These considerations indicate that for $n_f \geq 3$ the chiral transition is first order, while for $n_f = 0$, $N \geq 3$ the confinement transition is first order.

In QCD $N = 3$ but the value of n_f is less clear, complicating the analysis. The u and d quarks are unambiguously light compared to Λ_{QCD}, but as $m_s \sim \Lambda_{\text{QCD}}$ it is not obvious whether it should be considered light. Furthermore, it turns out the for $n_f = 2$ the chiral symmetry breaking transition is second order, while for $n_f = 3$ it is first order, so this distinction is important when determining the order of the transition. Ultimately

lattice studies are needed to determine the nature of the QCD phase transition, which indicate the transition is a crossover [44]. The SM therefore lies in an intermediate regime between large and small n_f where the phase transition is a crossover.

Confinement

To discuss the confinement transition we consider the limit where $n_f = 0$. As discussed in section 1.1.1 the relevant order parameter is the Polyakov loop P, defined in equation (1.14). As P is charged under a $\mathbb{Z}_N$ symmetry, for $N = 2$ the only terms in the potential are quadratic and quartic in P, so the transition is second order. For $N = 3$ there is also an allowed cubic term, so the phase transition could be first order, which is expected to be the case [41]. Adding light quarks to the theory ($n_f \neq 0$) explicitly breaks the $\mathbb{Z}_N$ symmetry. This is because the Polyakov loop can break through the nucleation of a quark anti-quark pair. If the quarks are heavy, this effect decouples as the nucleation process becomes exponentially suppressed. This means for $n_f > 0$ it is no longer correct to talk about the confinement transition and instead we should consider chiral symmetry breaking.

Chiral Symmetry Breaking

For the case of the chiral phase transition the symmetry breaking pattern is

$$G_\chi = SU(n_f)_L \times SU(n_f)_R \times U(1)_B \to SU(n_f)_V \times U(1)_B \,, \tag{1.39}$$

where $SU(n_f)_V$ is the diagonal subgroup of $SU(n_f)_L \times SU(n_f)_R$. The order parameter is the matrix

$$\Phi_{ij} = \langle \bar{Q}_i q_j \rangle \,, \tag{1.40}$$

which is an $n_f \times n_f$ matrix that transforms as $\Phi \to L^\dagger \Phi R$ under $SU(n_f)_L \times SU(n_f)_R$ where $L \in SU(n_f)_L, R \in SU(n_f)_R$. For $n_f = 1$ there is no symmetry breaking and the transition is second order, the only symmetry of the theory is $U(1)_B$ which remains unbroken in both phases.

For $n_f \geq 2$ we can write down the most general effective potential based on symmetry considerations (following the notation of [42] and ignoring possible quark mass terms):

$$V(\Phi) = \frac{m_\Phi^2}{2} \operatorname{tr} \Phi^\dagger \Phi + \frac{\pi^2 g_1}{3} \left(\operatorname{tr} \Phi^\dagger \Phi \right)^2 + \frac{\pi^2 g_2}{3} \operatorname{tr} \left(\Phi^\dagger \Phi \right)^2 + c \left(\det \Phi^\dagger + \det \Phi \right) . \tag{1.41}$$

The determinant term and coefficient c are related to the $U(1)_A$ anomaly of QCD and vanish for $n_f = 0$ or in the limit of large-N [45, 46]. For c sufficiently small the β-functions for the couplings g_1, g_2 in the $\epsilon = 4 - d$ expansion are

$$\beta_1 = -\epsilon g_1 + \frac{(n_f^2+4)}{3} g_1^2 + \frac{4n_f}{3} g_1 g_2 + g_2^2\,, \qquad \beta_2 = -\epsilon g_2 + 2g_1 g_2 + \frac{2n_f}{3} g_2^2\,. \tag{1.42}$$

There is a stable, weakly coupled fixed point in the IR only for $n_f \leq \sqrt{3}$, implying by the reasoning above that the chiral phase transition should be first order for any $n_f > \sqrt{3}$. When $c \sim 1$ then by a similar the $n_f = 2$ transition is continuous but the transition remains first order for $n_f \geq 3$.

While these arguments have loopholes to them, the results presented here for the confinement and chiral transitions have been confirmed in lattice simulations of QCD [32, 44, 47]. The final results for QCD-like theories is:

- For $n_f = 0$ the phase transition is a confining transition with the Polyakov loop serving as an order parameter. The phase transition is first order for $N \geq 3$.

- For $n_f \neq 0$ the phase transition will be first order if $n_f \geq 3$. If the coupling c in equation (1.41) is $\mathcal{O}(1)$ then for $n_f \leq 2$ the transition is continuous, while if $c \ll 1$ the $n_f = 2$ transition will be first order [48]. c is related to the chiral anomaly and is $\mathcal{O}(1)$ in QCD but suppressed in the large-N limit [46]. In the SM $c \sim 1$ and $n_f = 2$ and lattice studies show that the transition is a crossover.

1.4 BSM and first order transitions

We have discussed the two phase transitions which occur within the SM, however, there are many plausible scenarios for BSM physics which would lead to phase transitions in the early universe. If the SM is any guide to what lies beyond whatever completes the SM likely contains new gauge sectors. As discussed in the previous section this typically means the UV and IR phases of the theory are different, implying a phase transition at some scale. The order of the phase transition will depend on the details of the model, for the confinement transition this is the number of colours N and the number of light fermions, n_f, while for a higgsing transition this depends on the couplings of the order parameter to other fields at finite temperature.

As an example, for a new sector described by an $SU(N)$ gauge group with n_f fermions in the fundamental representation the β-function (1.9) will be negative for $n_f < 11N/2$. The general expectation is that the gauge group will confine at the scale where the coupling grows large, unless there is a higgsing transition before the theory reaches strong coupling. As mentioned above, the confining phase transition will be first order if $n_f = 0$ and $N \geq 3$, while for $n_f \geq 3$ the chiral symmetry breaking transition will be first order [42].

Grand unified theories embed the SM into a single non-abelian gauge group in the UV, which is then higgsed to the SM [1–3], leading to a phase transition in the early universe if T_r is above the GUT scale. Global symmetries can also be spontaneously broken in a similar manner and lead to a phase transition, for example the Peccei-Quinn phase transition in some axion models. At weak coupling these phase transitions can be analysed using the finite-T effective potential, as was done for the electroweak phase transition. If there is a barrier between the two minima at T_c then the phase transition will be first order, otherwise it will be second order.

Another possibility is that the electroweak phase transition is first order [49–53]. A simple realisation of this is in the SM with an additional singlet scalar S, with new Lagrangian terms

$$\mathcal{L}_S = \frac{1}{2}(\partial S)^2 - \frac{\kappa}{2}H^\dagger H S^2 - \frac{\eta}{4}S^4 + \frac{m^2}{2}S^2 \,. \tag{1.43}$$

At high temperatures the minimum of the scalar potential is $(h, S) = (0, 0)$ and the regime of interest is where the breaking occurs in the S direction first, after which $(h, S) = (0, \pm v_s)$, before the phase transition to the SM vacuum $(h, S) = (v_{\rm ew}, 0)$. The second step of the phase transition is first order if κ is sufficiently large. Making the EWPT first requires new field (typically scalars) coupled to the higgs in such a way to introduce a potential barrier between the minima of the higgs potential, either through a two-step transition such as the one described above or by generating a cubic term for the higgs through loop effects.

1.4.1 Holography and confinement phase transitions

The AdS/CFT correspondence offers another way to study confining transitions. The correspondence (or holography) is a duality between certain conformal field theories in the large-N limit [45] and gravitational theories on an AdS background in higher

Figure 1.4: Schematic of the RS model with the IR and UV branes shown in red and blue respectively. The green lines show lines of constant x^μ. Figure from ref. [54].

dimensions [55–57]. The canonical example is that of type IIB string theory on an $\mathrm{AdS}_5 \times S^5$ which is dual to an $SU(N)$ Yang-Mills theory with $\mathcal{N} = 4$ supersymmetry in four dimensions [55]. While holography has been studied in many contexts, for the purposes of this thesis our interest is in holography as a tool to study confinement. The reason it is useful for doing so is that typically when one side of the duality is strongly coupled the other is weakly interacting. If the CFT is at strong coupling, then the gravitational theory is well described by classical gravity.

In exactly conformal theories, however, there can be no phase transitions due to the scale symmetry of the theory. Scale symmetry is the invariance under the scaling of spatial co-ordinates:

$$x^\mu \to \lambda x^\mu \,, \tag{1.44}$$

under which a CFT operator transform as $\phi \to \lambda^{-\Delta}\phi$, where Δ is known as the scaling dimension of ϕ. Under the transformation (1.44) the temperature scales as $T \to T/\lambda$, so invariance under (1.44) implies that the phase of a CFT must be the same for all temperatures, at least in an infinite volume [58]. However, by deforming a CFT in a way that breaks scale invariance, we can construct approximately conformal theories which do allow a phase transition that can be analysed using holography.

Holographic constructions where the two sides of the duality are precisely known typically involve string compactifications with some number of compact internal dimensions [59–62]. Instead of considering a complete model, here we instead consider the

Randall-Sundrum (RS) model [7, 63] – a 5d theory of fields propagating on an AdS background. This can be thought of as an approximation to a more complete holographic theory [64–68] that will allow us to make statements about confinement phase transitions in (approximately) conformal large-N theories.

The metric of the RS model is the 5d AdS metric:

$$ds^2 = \frac{1}{(kz)^2}\left(\eta_{\mu\nu}dx^\mu dx^\nu - dz^2\right) \tag{1.45}$$

where k is the curvature scale and the extra dimension (z) is cut-off by two branes (the IR and UV branes) at $z_{\rm ir}$ and $z_{\rm uv}$, see figure 1.4. A rescaling $z \to \lambda z, x^\mu \to \lambda x^\mu$ leaves the metric invariant, which is the gravitational description of scale invariance in the CFT, and $1/z$ can be thought of as the energy scale of the CFT. The two branes cut off the spacetime at both ends, which indicate that scale symmetry is broken at a UV scale ($z_{\rm uv}^{-1}$) and an IR scale ($z_{\rm ir}^{-1}$) [69, 70].

The UV cut-off corresponds to including gravity in the conformal field theory, with the corresponding scale being the Planck scale of the CFT [71]. The coupling to gravity breaks scale invariance at the Planck scale, but below this scale the effective theory is conformal down to the IR scale. The IR scale is generated spontaneously by a marginal operator which runs. For scales between $z_{\rm uv}^{-1}$ and $z_{\rm ir}^{-1}$ the running is small and this can be treated as a perturbation to the conformal background, while the running becomes large near the scale $z_{\rm ir}^{-1}$ and scale symmetry is no longer a good approximation. In the gravitational theory this corresponds to adding a scalar field which has a non-trivial background profile in the z direction [72]. This generates a potential for $z_{\rm ir}$ which is then dynamically selected to minimise the potential. The scale generated is identified with the confinement scale of the CFT, and the RS model is a gravitational description of the confined phase of a CFT.

The phases of a gravitational theory come from studying the partition function. In the saddle point approximation the euclidean path integral can be approximated as

$$Z = \sum_{\bar{g}} e^{-S_E[\bar{g}]}\,, \tag{1.46}$$

where $\bar{g}$ are the metric solutions to Einstein's equations. Static solutions represent possible phases of the theory and the euclidean action gives

$$S_E[\bar{g}] = \beta F \tag{1.47}$$

where F is the free energy of a given phase. The preferred phase at a given temperature is the one with the lowest free energy, as it will exponentially dominate the partition function (1.46).

At high temperatures the RS model described above is not the preferred phase of the gravitational theory. The free energy of the RS phase goes like $F_{RS} \sim \epsilon^{3/2} z_{\rm ir}^{-4}$, where ϵ is a small parameter related to the breaking of scale invariance [8]. Instead the high temperature phase is the AdS-Schwarzschild (AdS-S) phase, whose free energy scales like $F_{AdS-S} \sim N^2 T^4$ where N is the large-N parameter of the CFT. The scaling of the free energies matches what is expected from a a confinement transition – in the deconfined phase the free energy scales as $F \sim N^2 T^4$ as there are N^2 massless gluons, while in the confined phase $F \sim \Lambda^4$, where Λ is the confinement scale. In the AdS-S phase the IR brane of the RS model is replaced with a black hole horizon.

The phase transition corresponds to the appearance of the IR brane from behind the AdS-S horizon [8, 58, 73] and is first order. This agrees with the discussion above, where confinement transition in Yang-Mills theory with no quarks is a first order transition. Due to the approximate scale invariance of the theory the phase transition is strongly suppressed and can lead to problems with the cosmology of the model, as discussed in more detail in chapter 2.

1.4.2 General formalism for First Order Phase Transitions

First order phase transitions proceed in a very different manner to their second order counterparts. Rather than the field continuously evolving from the false to true vacuum, a first order phase transition occurs when there is a potential barrier which separates the false vacuum from the true vacuum. If the barrier height between the vacua is large the transition is said to be strongly first order, which is the regime which is relevant for the phase transitions studied in this thesis.

In this case the transition proceeds through an exponentially suppressed tunnelling process where a spherical bubble of true vacuum is nucleated inside the false vacuum background [74]. The suppressed transition rate means that bubbles are being nucleated very slowly and will grow to a macroscopic size before meeting. This can lead to significant

gravitational wave production when they eventually collide, or an eternally inflating universe if that transition proceeds too slowly. These implications are discussed in greater detail in section 1.5, for this section a general discussion of how to calculate the rate of a first order transition is presented.

The basic picture of a first order phase transition is that bubbles of true vacuum are being nucleated at a rate per unit volume $\Gamma(T)$. The interior of the bubble contains the true vacuum ($\phi_{\rm tv}$), while the relevant field(s) asymptote to their false vacuum value ($\phi_{\rm fv}$) outside the bubble. The bubble wall refers to the intermediate region where the field(s) interpolate between the two vacua. As the true vacuum is at a lower point on the potential than the surrounding false vacuum, there is an outwards pressure which causes the bubble to expand after being nucleated. For a sufficiently rapid transition the bubbles will eventually meet and collide, leaving the universe in the true vacuum state.

The transition rate is given by [75, 76]:

$$\Gamma(T) = A(T) \exp\left(-B(T)\right) , \tag{1.48}$$

where $B(T)$ is the euclidean action evaluated on the bounce solution to the field equations, ϕ_b:

$$B(T) = S_E[\phi_b] - S_E[\phi_{\rm fv}] . \tag{1.49}$$

The bounce solution satisfies the euclidean equation of motion

$$\ddot{\phi}_b + \nabla^2 \phi_b = \frac{dV(\phi_b, T)}{d\phi_b} , \tag{1.50}$$

where V is the effective potential. There are multiple solutions to equation (1.50); the bounce is the solution satisfying the boundary conditions

$$\dot{\phi}_b(\tau = 0, \vec{x}) = 0 , \qquad \phi_b(2\pi/T, \vec{x}) = \phi(\tau, |\vec{x}| \to \infty) = \phi_{\rm fv} , \tag{1.51}$$

where τ is the euclidean time. The case where multiple fields evolve during the phase transition is a straightforward generalisation of the above equations, where now equation (1.50) will be a set of coupled PDE's for the relevant set of fields.

In the $T \to 0$ limit it can be shown (given some mild assumptions on the form of V) that the solution to (1.50) which minimises the action is always a function of the

$O(4)$ symmetric combination of co-ordinates $\rho = \sqrt{\tau^2 + r^2}$ [77]. In the high-T limit the solution which minimises the action is τ-independent [78] and depends only on r. In some cases there is also an intermediate regime where ϕ_b depends independently on τ and r, although this is not always the case.

In the limit where the energy difference between the vacua is small relative to the barrier height, the solution to the equation of motion (1.50) takes a particularly simple form. In this case the friction terms in (1.50) can be ignored and the solution described solely in terms of the bubble radius R_b. The radius and action for the $O(4)$ symmetric bounce are:

$$R_b = \frac{3\sigma}{\epsilon}\,, \qquad\qquad B = \frac{27\pi^2\sigma^4}{2\epsilon^3}\,, \tag{1.52}$$

where:

$$\sigma = \int_{\phi_{\rm fv}}^{\phi_{\rm tv}} d\phi \sqrt{2\left(V(\phi) - V(\phi_{\rm fv})\right)}\,, \qquad\qquad \epsilon = V(\phi_{\rm fv}) - V(\phi_{\rm tv})\,. \tag{1.53}$$

The approximation is only valid close to the critical temperature, but gives an indication as to the dependence of the bounce on the shape of the potential. Close to T_c the minima of the potential become degenerate, $\epsilon \to 0$, and the bounce diverges. This indicates that the transition rate is highly suppressed close to the critical temperature. For a potential with a large barrier separating the minima σ becomes large, again suppressing the transition rate.

The general behaviour of the bounce action depends on whether or not the barrier separating the vacua persist down to $T = 0$ or not. As $T \to T_c$ from below, $B(T)$ diverges as $\phi_{\rm fv}$ becomes the true ground state of the potential. For most cases of interest the bounce solution close to T_c is the high-temperature solution, which goes like

$$B(T) = S_3(T)/T\,. \tag{1.54}$$

If the potential barrier between $\phi_{\rm tv}$ and $\phi_{\rm fv}$ disappears below some $\bar{T}$ then $B(T)$ vanishes as $T \to \bar{T}$ and the transition becomes second order. If the barrier between the minima persists for small T then $S_3(T)$ will decreases as T drops below T_c before reaching a constant value as the thermal corrections to the potential become negligible. Below this point $B(T) \propto 1/T$, so begins increasing at lower T until the $O(4)$ symmetric solution begins to dominate. These scenarios for $B(T)$ are shown in figure 1.5.

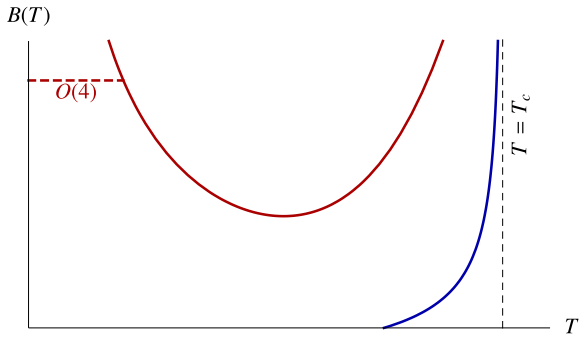

Figure 1.5: Plot showing the possible behaviours of the bounce action as a function of temperature. The blue curve shows the case where there is barrier in the potential near T_c which disappears as $T \to 0$, which can be seen as the bounce action goes to zero. The red curve shows the case where the barrier persists to $T = 0$. At low temperature the $O(3)$ symmetric bounce goes like $B \propto 1/T$ but at some temperature the solution with smallest action will be the $O(4)$ symmetric bounce (dashed red line). At the critical temperature (vertical dashed line) the bounce action for each solution diverges.

The prefactor, $A(T)$, in equation (1.48) is given by the determinant of quadratic fluctuations around the bounce solution, with the negative mode removed [76]. As it is a sub-leading effect, we will usually estimate it on dimensional grounds as $A(T) \sim \max\left(T^4, v^4\right)$, where v is a typical scale of the transition (usually the vev of the scalar field in the low temperature phase).

1.5 Cosmological Implications of first order phase transitions

In this section we review some of the impacts that BSM phase transitions can have on cosmology. In section 1.5.1 we discuss cosmological bounds which come from requiring that phase transitions complete before a period of exponential expansion of the universe begins. Section 1.5.2 is devoted to determining the gravitational wave signal produced in a first order phase transition and section 1.5.3 discusses the production of topological defects in cosmological phase transitions.

1.5.1 Supercooling

If the universe were static then a phase transition would always complete in a finite time period, regardless of the transition rate. In an expanding universe, however, the expansion of the false vacuum can be faster than the expansion of the bubble walls, leading to a

universe which remains mostly in the false vacuum. This is because $\phi_{\rm fv}$ is not the true minimum of the potential, so the cosmological constant receives a contribution from $V(\phi_{\rm fv})$. This can be problematic for supercooled phase transitions and leads to strong bounds on some models, such as the holographic phase transitions discussed in section 1.4.1.

To be consistent with present-day observations, the energy density in the cosmological constant (Λ) today must be [22]

$$\rho_\Lambda \sim (40\,\text{meV})^4 \,, \tag{1.55}$$

which is negligibly small in comparison to the energy densities relevant for the early universe. This means that Λ in the low energy vacuum ($\phi_{\rm tv}$) must be effectively zero, implying that $V(\phi_{\rm fv})$ gives a positive contribution to Λ in the false vacuum phase. Assuming the phase transition takes place during radiation domination, the Hubble rate in the false vacuum then must be

$$H^2(T) = \left(\frac{\dot{a}}{a}\right)^2 = \frac{8\pi}{3M_P^2}\left(\frac{\pi^2 g_* T^4}{30} + V(\phi_{\rm fv})\right) . \tag{1.56}$$

The cosmological constant term will begin to dominate once the temperature drops below $T \sim V(\phi_{\rm fv})^{1/4}$ and the universe will enter an inflationary phase if the phase transition has not yet completed. If the transition rate Γ is small compared to H^4 bubbles will never meet, even though they are continuously being nucleated and expanding [79]. This leads to a universe filled with very large expanding bubbles of true vacuum, where the false vacuum region between bubbles is expanding exponentially.

The co-moving volume occupied at time t by a bubble nucleated at early time t' is:

$$V(t,t') = \frac{4\pi}{3}\left(\int_{t'}^{t} dt'' \frac{v_w}{a(t'')}\right)^3 . \tag{1.57}$$

In the radiation era $a \sim t^{1/2}$, so the volume is always increasing, $V \propto t^{3/2}$. For bubbles nucleated in the inflationary phase, $a \sim e^{Ht}$ and the volume (1.57) approaches a constant at late times

$$\lim_{t\to\infty} V(t,t') = \frac{4\pi v_w^3}{3H^3} e^{-3Ht'} . \tag{1.58}$$

Here we see that in the radiation era even if bubbles are being nucleated very slowly they will eventually come to fill the universe, but this is not true in the inflationary phase. The fraction of space remaining in the false vacuum at time t is then given by [79–81]:

$$p(t) = e^{-I(t)} = \exp\left[-\int_{t_c}^{t} dt' \Gamma(t') a^3(t') V(t,t')\right], \tag{1.59}$$

where v_w is the bubble wall velocity. In the radiation dominated era the integral $I(t)$ can be approximated as

$$I(t) \to \frac{4\pi v_w^3 \Gamma(t)}{15 H(t)^4} \tag{1.60}$$

at late times. Then the the universe will be predominantly in the true vacuum phase when

$$\Gamma(t) > H(t)^4\,, \tag{1.61}$$

or when the rate is such that there is one bubble being nucleated per Hubble patch per Hubble time. This allows us to define a nucleation temperature, T_n, as the temperature when the condition (1.61) is first satisfied.

If the universe enters an inflationary phase, the vanishing of $p(t)$ is no longer a sufficient condition for the transition to complete. Assuming Γ is constant then in this regime

$$I(t) = \frac{4\pi v_w^3 \Gamma t}{3H^3}\,, \tag{1.62}$$

implying that $p(t)$ goes to zero at late times. However, this condition does not guarantee that bubbles will meet and collide. A second necessary condition for this to occur is that the physical volume of false vacuum $V_\mathrm{fv} \propto a^3(t) p(t)$ is decreasing [82], which requires

$$3H - \frac{dI}{dt} < 0\,. \tag{1.63}$$

Using the late-time expression (1.62) this translates into a bound

$$\frac{\Gamma}{H^4} > \frac{9}{4\pi}\,. \tag{1.64}$$

In both cases, a heuristic condition for the phase transition to complete is

$$\Gamma(T_\mathrm{n}) = H(T_\mathrm{n})^4\,, \tag{1.65}$$

for some nucleation temperature $T_{\rm n}$. Assuming the prefactor $A(T)$ in equation (1.48) is of order T^4 this translates into a condition on the bounce action

$$B(T) < 4\log\left(\frac{T}{H(T)}\right) = 4\log\left(\frac{M_P}{T}\right) - 2\log\left(\frac{4\pi^3 g_*}{45}\right) \tag{1.66}$$

where the second equality assumes radiation domination.

1.5.2 Gravitational Waves

The first detection of gravitational waves by the LIGO collaboration [83] has led to a number of proposed experiments which aim to proposed to detect gravitational waves over a range of frequencies [84–97]. Some of these experiments are sensitive to the gravitational wave signal from a first order phase transition in the early universe [9,10], a detection which would offer the first direct probe of the pre-BBN universe. In this section the features of the gravitational wave signal produced during a phase transition are discussed.

A first order phase transition can also lead to a gravitational wave signal which may be observed in upcoming experiments. There are three sources of gravitational waves during a phase transition:

1. collisions between bubbles [98–101];

2. sound waves in the thermal plasma generated by the motion of the bubble walls [102–104]; and

3. turbulent motion of the plasma induced by bubble walls [105–110].

The signal generated is typically dominated by one of the three contributions, with the dominant contribution depending on the temperature, the transition rate and the bubble wall velocity. An analytic derivation of the signal is not possible, and simulations are needed to determine the gravitational wave signal. Due to the vastly different length scales in the problem simplifications are required in order to simulate the transition [111], and the exact signal is not precisely known. Turbulence is the least understood contribution to the signal [10] and for that reason we focus on the signal from bubble collisions and sound waves.

An important parameter in the calculation of the gravitational wave signal is the inverse timescale β, defined as:

$$\beta := -\left.\frac{d}{dt}B(T)\right|_{T_\mathrm{n}} = H(T_\mathrm{n})T_\mathrm{n}\left.\frac{dB}{dT}\right|_{T_\mathrm{n}}, \tag{1.67}$$

where β^{-1} corresponds to the average time for two bubbles nucleated at different points to collide. Another important quantity is the latent heat, normalised to the radiation energy density:

$$\alpha(T) = \frac{1}{\rho_\mathrm{r}(T)}\left(\Delta V - \frac{1}{4}\frac{\mathrm{d}\Delta V}{\mathrm{d}T}\right), \tag{1.68}$$

where $\Delta V = V(\phi_\mathrm{fv}) - V(\phi_\mathrm{tv})$ is the difference in the potential evaluated at the two vacua. Equation (1.68) should be evaluated at the percolation temperature T_p, which is the temperature when the entire universe is in the true vacuum, but in most cases $T_\mathrm{p} \simeq T_\mathrm{n}$ so T_n is often used in (1.68).

Bubble wall velocity

The final important quantity for determining the gravitational wave signal is the velocity of the bubble walls, v_w, as they move through the plasma. The wall velocity depends on a balance between the energy released during the transition and the friction on the bubble walls exerted by the plasma. The general expression for the evolution of the wall velocity is

$$\frac{d|\vec{v}|}{dt} = \frac{1}{\gamma^3\sigma}\left(\Delta V - \mathcal{P}\right) \tag{1.69}$$

where $\mathcal{P}$ is the friction pressure, γ is the lorentz factor of the wall and σ the wall tension. At leading order in the couplings the pressure is generated by particles whose mass changes as they cross the wall and is given by [112]

$$\mathcal{P}_{1\to1} \simeq \sum_i \left(m_{i,\mathrm{tv}}^2 - m_{i,\mathrm{fv}}^2\right)T^2, \tag{1.70}$$

where the sum is over thermalised species. This is a result of energy conservation, as a particle which gains mass as it crosses the wall must slow down, implying there is a backreaction on the bubble wall. If ΔV is larger than the pressure $\mathcal{P}_{1\to1}$ as $\gamma \to \infty$ then the wall will continue to accelerate and 'run away', with v_w approaching 1.

In some cases, there are also splitting transitions which can be the dominant source of friction on the bubble wall in the relativistic limit. This comes from splitting ($1 \to 2$ processes) of gauge bosons as they cross the bubble wall and appears at a higher order in couplings, where the additional suppression is overcome by a large γ factor. It is only relevant if the scalar field which varies across the phase boundary generates a mass for gauge bosons which are thermalised in the plasma. For the SM higgs, the electroweak gauge bosons induce a pressure which scales as [113]:

$$\mathcal{P}_{1\to 2} \simeq \gamma g^2 M_W T^3 \,, \tag{1.71}$$

limiting the maximum possible lorentz boost of the wall to be $\gamma_{\max} \sim T/g^2 M_W \sim \mathcal{O}(10)$. In most cases the bubbles rapidly accelerate to relativistic speeds, so if present this source of friction typically dominates despite being at a lower order in couplings. Depending on the particle content and the couplings of the scalar fields undergoing the transition, there can be other sources of pressure which can dominate in certain regimes [114], however, for this work the main contributions are from (1.70) & (1.71).

Collisions of bubble walls

The computation of the gravitational wave signal from the collision of bubbles during a first order phase transition is complex and requires numerical simulations to provide accurate results. However, we can make generic estimates of the signal based on the scales in the problem. The regime where bubble collisions are the dominant source for the signal is when $v_w \sim 1$, so we will assume this is the case during this section. There is a characteristic time scale in the problem, β^{-1}, which sets the frequency of gravitational waves at emission, $2\pi f_* = \beta$. Redshifting to today, this means the frequency of these gravitational waves is [101]

$$f_0 = f_* \left(\frac{a_0}{a_*}\right) \simeq 10^{-5} \left(\frac{\beta}{H_*}\right) \left(\frac{106.75}{g_*(T_*)}\right)^{1/6} \left(\frac{T_*}{100\text{GeV}}\right) \text{Hz} \tag{1.72}$$

To get a sense of the intensity of the gravitational radiation released in the transition we can use similar scaling arguments. For a bubble of size R the amount of energy released is given by $E_b \sim \kappa_b \Delta V R^3$, where κ_b is an efficiency factor which determines the

proportion of the vacuum energy which is converted into energy of the bubble wall. Then the energy converted into gravitational waves scales as

$$E_{\rm GW} \sim \frac{E_b^2}{M_P^2 R} \sim \frac{\kappa_b^2 (\Delta V)^2}{M_P^2 \beta^5}\,, \tag{1.73}$$

as the quadrople moment of the two bubble system is $Q \sim E_b/R$ and $R \sim \beta^{-1}$ [98]. Then if $\Delta V \sim T_{\rm n}^4$, the energy fraction of gravitational waves at production is roughly

$$\Omega_{\rm gw} \sim \kappa_b^2 \left(\frac{H_*}{\beta}\right)^2 \Omega_R\,. \tag{1.74}$$

A more quantitative estimate for gravitational wave signal for two bubble collisions can be calculated using the envelope approximation [98–101]. This approximation amounts to assuming all of the energy of the bubbles is stored in the bubble walls in a thin shell and is released the moment they collide. The two-bubble collision can then be generalised to the multi-bubble case through simulations [110, 115–118]. The final spectrum is well approximated by:

$$\Omega_{\rm GW} h^2 \simeq 1.7 \times 10^{-5} \left(\frac{H_*}{\beta}\right)^2 \left(\frac{\kappa_b \alpha}{\alpha+1}\right)^2 \left(\frac{100}{g_*}\right)^{1/3} \left(\frac{0.11 v_w^3}{0.42 + v_w^2}\right) S_{\rm env}(f)\,, \tag{1.75}$$

$$S_{\rm env}(f) = \frac{3.8 (f/f_0)^{2.8}}{1 + 2.8 (f/f_0)^{3.8}}\,, \tag{1.76}$$

where the peak amplitude agrees with the rough scaling (1.74). The peak frequency today is

$$f_0 \sim 16.5 \times 10^{-6}\,{\rm Hz} \left(\frac{0.62}{1.8 - 0.1 v_w + v_w^2}\right) \left(\frac{\beta}{H_*}\right) \left(\frac{T_*}{100\,{\rm GeV}}\right) \left(\frac{g_*}{100}\right)^{1/6}\,. \tag{1.77}$$

From equation (1.75) it can be seen that the gravitational wave signal is largest when the phase transition is slow, i.e. when $\beta \sim H_*$. Due to redshifting of the radiation energy density, the factor α is also expected to be larger for a slower phase transition. This means that the phase transitions which produce the largest gravitational wave signal are those that come close to saturating the bounds of section 1.5.1.

Sounds Waves in Plasma

For runaway bubble wall velocities (where $\gamma \to \infty$) bubble collisions are expected to be the dominant source of gravitational waves. However, for bubbles which reach a terminal velocity the signal is expected instead to be dominated by sound waves created in the

plasma due to the motion of the bubble wall. This is expected as, once the bubble reaches its terminal velocity the energy in the walls scales like R^2 for a bubble of radius R, while the energy being released scales like R^3 [10], the remainder of which goes into sound waves.

While the gravitational wave signal produced from collisions is suppressed by $(H_*/\beta)^2 < 1$, for the case of sound waves this suppression factor becomes

$$\left(\frac{H_*}{\beta}\right) H_* \tau_s \tag{1.78}$$

where τ_s is the length of time the sound waves in the plasma persist before damping. If the sound waves last a hubble time, $\tau_s \sim H_*^{-1}$ then the relative single is enhanced in comparison to the collision signal by the factor β/H_* which can be $\sim 10^2$ depending on the dynamics of the phase transition. There is also an efficiency factor for the conversion of vacuum energy into sound waves of the fluid which is related to the efficiency factor κ_b by

$$\kappa_{\rm sw} = \frac{\alpha(1-\kappa_b)^2}{0.73 + 0.083\sqrt{\alpha(1-\kappa_b)} + \alpha^2(1-\kappa_b)^2}\,. \tag{1.79}$$

For a runaway transition, $\kappa_b \to 1$, meaning negligible sound waves are produced.

In terms of these quantities the gravitational wave amplitude and peak frequency today ($f_{p,0}$) are given by [102, 119–121]

$$\begin{aligned} \frac{d\Omega_{\rm gw\,,0}}{d\ln(f)} &= 1.2\times 10^{-6}\left(\frac{v_w H_*}{\beta}\right)\left(\frac{\kappa_{\rm sw}\alpha}{1+\alpha}\right)^2\left(\frac{100}{g_*}\right)^{1/3} S(f/f_{p,0})\,, \\ f_{p,0} &\simeq 8.9\left(\frac{v_w H_*}{\beta}\right)\left(\frac{T_*}{100\,\text{GeV}}\right)\left(\frac{g_*}{100}\right)^{1/6}\mu\text{Hz}\,. \\ S(x) &= x^3\left(\frac{7}{4+3x^2}\right)^{7/2} \end{aligned} \tag{1.80}$$

The gravitational wave spectrum in (1.80) is accurate when the time for shock formation is larger than one Hubble time, namely if

$$H_*\tau_s \simeq 3.4\times\left(\frac{v_w H_*}{\beta}\right)\sqrt{\frac{1+\alpha}{\kappa_{\rm sw}\alpha}} > 1. \tag{1.81}$$

When this inequality is not satisfied, equation (1.80) needs to include an additional suppression factor given by $H_*\tau_s$ [122].

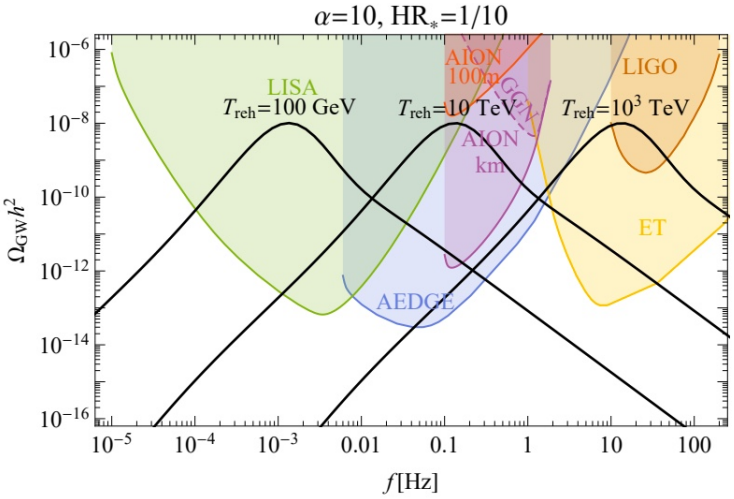

Figure 1.6: Plot showing examples of potential gravitational wave signals from phase transitions. The black curves show the spectrum of gravitational waves from an early universe phase transitions which occur at temperatures 100 GeV, 10 TeV and 10^3 TeV. The coloured regions are the forecasted exclusion limits from the LISA (green) [88], AEDGE (blue) [94], AION (red & purple) [97], LIGO (orange) [123] and ET (yellow) [86] experiments. Figure taken from [97].

1.5.3 Topological Defects

Depending on the pattern of symmetry breaking, a phase transition can lead to topological defects in the broken phase [124]. This requires there to be a family of degenerate vacua of the potential, which will be the case if the true vacuum spontaneously breaks a symmetry of the full theory. The symmetry group G acts on ϕ as

$$\phi \to R(g)\phi\,, \tag{1.82}$$

where R is a representation matrix of G. If G is broken to a subgroup H by the expectation value ϕ_0 then $R(h)\phi_0 = \phi_0$ for $h \in H$ while elements of G/H act on ϕ_0 non-trivially, taking ϕ_0 to another vacuum state. The manifold of degenerate vacua is therefore given by $\mathcal{M} = G/H$.

Defects are present in a theory when there are closed loops in physical space which have topologically distinct mappings to the vacuum manifold $\mathcal{M}$. Mathematically this condition is the requirement that a homotopy class of $\mathcal{M}$ is non-trivial. The homotopy class π_n of a manifold $\mathcal{M}$ is the set of topologically distinct continuous maps from an n-sphere S^n to $\mathcal{M}$. If we consider all maps $f : S^n \to \mathcal{M}$ and define an equivalence relation, $f \sim f'$ if f

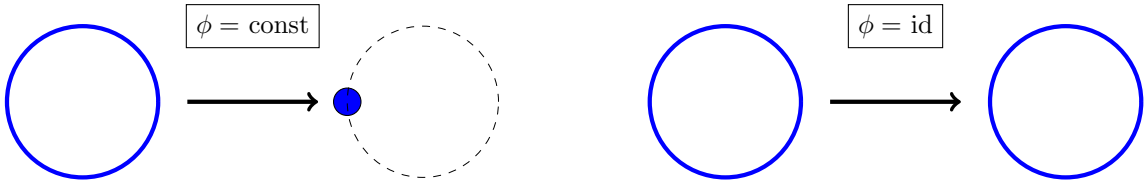

Figure 1.7: Examples of different elements of the homotopy group $\pi_1(U(1))$, the equivalence classes of maps from S^1 to itself. The left picture shows the trivial map where every point in S^1 maps to a single point in $U(1)$, while the second shows the identity map where each point in $U(1)$ is passed through once. In general any mapping can be classified by an integer n which measures how many times each point in the image is passed through, the two cases here are $n = 0$ and $n = 1$.

can be continuously deformed to f' then the set of distinct maps under this equivalence relation is $\pi_n(\mathcal{M})$, which forms a group under composition for $n \geq 1$.

The relevance of this comes from considering the scalar field(s) ϕ as a map from spacetime to $\mathcal{M}$. For a subregion of spacetime $S^n \subset \mathbb{R}^{1,3}$ the field ϕ on this region is a map from $S^n \to \mathcal{M}$, so can be classified as an element of $\pi_n(\mathcal{M})$. The case where ϕ is constant corresponds to the trivial element of π_n. In the preceding chapters this has been the focus, however, we can also consider topologically non-trivial maps. An example of the difference between the two cases is shown in figure 1.7.

As will be shown in the examples below, the consequence of ϕ having a non-trivial topology is that there must exist regions of space where ϕ takes values away from $\mathcal{M}$. This leads to localised regions of energy density which are known as topological defects, some examples of which are described below. The general form of the potential we consider for each example is

$$V = \frac{\lambda}{4}\left(\phi^2 - v^2\right) , \tag{1.83}$$

where ϕ is understood to transform in some representation of G.

Domain Walls

The simplest example of this kind is where a $\mathbb{Z}_2$ symmetry is spontaneously broken by the vev of a real scalar. $\mathcal{M}$ consists of two points, $\pm v$, for the potential (1.83). As $\mathcal{M}$ is disconnected, $\pi_0(\mathcal{M})$ is non-trivial as any point x can be mapped to either of the two vacuum states, and there is no way to smoothly deform $\phi(x) = v$ to $\phi(x) = -v$.

The topological defects this leads to are known as domain walls. If ϕ takes different values at two points then it must interpolate between the two vacua over some finite

region. For the potential (1.83), a domain wall centred at $z = 0$ and constant in the x, y directions has the field profile:

$$\phi(z) = v \tanh\left(\sqrt{\frac{\lambda}{2}} vz\right) . \tag{1.84}$$

In 4d the domain wall is a 2-dimensional surface with a constant energy density. Due to it's infinite extent, it takes an infinite amount of energy to vary the field so that it is everywhere in the $\phi = v$ or $\phi = -v$ vacuum state, so the domain wall is topologically stable.

Strings

The second example we consider is the breaking of a $U(1)$ symmetry by a complex scalar field. As $U(1)$ is topologically a circle, $\pi_1(U(1))$ is equal to $\mathbb{Z}$, where the element $n \in \mathbb{Z}$ corresponds to a map which winds around the target S^1 n times. The cases for $n = 0, 1$ are shown in figure 1.7. We can consider the ansatz for the scalar field

$$\phi(\rho, \theta, z) = vh(\rho)e^{in\theta} \tag{1.85}$$

where $h(\infty) = 1$. Then $\phi(\infty, \theta, z)$ for fixed z maps the spatial S^1 at $\rho \to \infty$ (for fixed z) to $U(1)$ with winding number n. In order for ϕ to be continuous at $\rho = 0$ it must be that $h(0) = 0$, meaning that there is a region around $\rho = 0$ where ϕ is away from the minimum of the potential. This region forms a line in the z direction, corresponding to a string.

Monopoles & Skyrmions

Monopoles (or skyrmions in the global symmetry case) are produced when the breaking yields a non-trivial $\pi_2(G/H)$. The canonical example of this is $SU(2)$ broken to $U(1)$ but the solution can be embedded in to a larger group which contains an $SU(2)$ subgroup [124, 125]. Again the potential has the form of equation (1.83), with ϕ in the triplet representation of $SU(2)$. Considering a spherical co-ordinate system with the centre of the monopole at $r = 0$, then

$$\phi^a_\infty(\theta, \varphi) = \lim_{r\to\infty} \phi^a(r, \theta, \varphi) \tag{1.86}$$

is an element of $\pi_2(SU(2)/U(1)) = \mathbb{Z}$ so can be labelled by a winding number. The $n = 1$ element corresponds to

$$\phi^a(r, \theta, \varphi) = v\hat{r}^a h(r) , \tag{1.87}$$

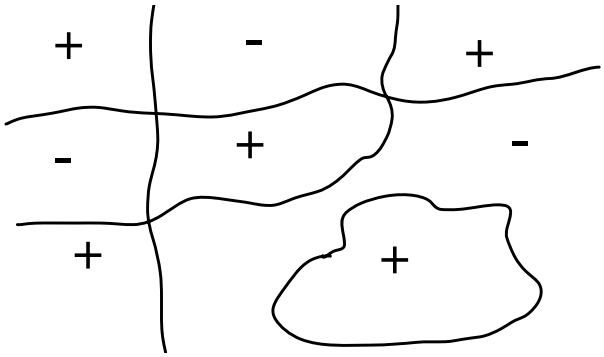

Figure 1.8: Kibble mechanism for production of domain walls. The + (−) labels represent the $\phi = v\,(-v)$ vacua in different regions of space, with the lines showing the domain walls separating the different regions.

where $h(r) \to 1$ as $r \to \infty$ and $h(0) = 0$ from continuity. The monopole is therefore a spatially localised field configuration which behaves like a particle.

If the $SU(2)$ is a gauge group then the gauge fields also have a non trivial profile around the monopole core, and the $n = 1$ configuration has a mass

$$M_m = \frac{8\pi v}{3e}\,. \tag{1.88}$$

The monopole also has a magnetic charge under the unbroken $U(1)$ gauge group given by

$$Q_M = \frac{2\pi}{e}\,. \tag{1.89}$$

Kibble Mechanism

While the above discussion shows under what circumstances topological defects exist, it is not clear when or how they will actually be produced. Closed domain walls and string loops will shrink to zero size, so the defects which are long-lived are of macroscopic size and require significant energy to produce. Monopoles have mass $M_m \gg v$, and as they are only present in the broken phase this might lead one to naively conclude that they too should be produced in negligible amounts. However, the dynamics of phase transitions will generically lead to their production via the Kibble mechanism if the full symmetry G was restored in the high temperature phase [126, 127].

The reason for this is that the present day universe contains many patches each of which were causally disconnected at the time of the phase transition. As $\mathcal{M}$ describes a set

of degenerate vacua, the phase transition is equally likely to end at any point on $\mathcal{M}$. This means that causally disconnected regions of space will generically end the phase transition at different points on $\mathcal{M}$, inevitably leading to some winding in the fields and the production of topological defects. This is shown in figure 1.8 for the case of a $\mathbb{Z}_2$ breaking transition which produces domain walls. The number of defects produced depends on the correlation length, ξ, of the transition. For monopoles the number density produced is $n_m \sim \xi^{-3}$, while the number of strings per unit area will scale as $n_s \sim \xi^{-2}$ and the number of domain walls per unit length will scale as ξ^{-1}. The correlation length depends on the type of phase transition, and can be estimated as $\xi \sim v_w \beta^{-1} \sim \mathcal{O}(H)$ for a first order transition, while for a continuous transition typically $\xi \ll H$. This means in any transition which leads to the production of defects we would expect at least one defect per hubble patch, although the number of defects produced could be much larger if the transition is second order.

Cosmological bounds

There are strong bounds on the cosmological abundances of domain walls and magnetic monopoles. Domain walls are described by a surface tension, σ, which for the potential (1.83) is given by $\sigma = v^3 \lambda^{1/2}$. After being produced, the domain wall network reaches a scaling regime where this $\mathcal{O}(1)$ domain wall per hubble patch. In this regime the energy density in domain walls scales like

$$\rho_{\rm DW} \simeq \frac{\sigma}{t}\,, \tag{1.90}$$

meaning that the energy density in domain walls falls more slowly than that of radiation (which goes as $\rho_{\rm rad} \propto t^{-2}$). Domain walls will come to dominate the expansion of the universe within a hubble time, after which the scale factor grows

$$a \propto t^2\,. \tag{1.91}$$

This leads to an accelerated expansion which is inconsistent with observations [128], meaning that domain walls must either have decayed or have energy scales $\sigma \lesssim 1$ MeV [129, 130]. If there is a bias in the potential from a $\mathbb{Z}_2$ breaking term which means the minima aren't exactly degenerate [131] then this can be avoided, as the difference in energies between the two vacua will cause the regions in the false vacuum to collapse.

Production of magnetic monopoles is also in conflict with cosmological observations. The number density of monopoles produced during a phase transition which occurs at temperature T_c is

$$n_m \gtrsim \frac{T_c^6}{M_P^3}\,, \tag{1.92}$$

leading to an overall energy density

$$\rho_m \gtrsim M_m \frac{T_c^6}{M_P^3}\,, \tag{1.93}$$

and a present-day abundance of

$$\Omega_m h^2 \simeq 10^{11} \left(\frac{T_c}{10^{14}\,\mathrm{GeV}}\right)^3 \left(\frac{M_m}{10^{16}\,\mathrm{GeV}}\right)\,. \tag{1.94}$$

Requiring this be less than the current matter density $\Omega_m h^2 \sim 0.12$ rules out heavy monopoles being produced via the Kibble mechanism [132].

There is also another astrophysical bound for monopole with magnetic charge under $U(1)_{\mathrm{em}}$, known as the Parker bound. Magnetic monopoles will be accelerated by galactic magnetic fields and ejected from the galaxy, draining energy from the galactic magnetic fields in the process. Requiring that the energy lost in this process is negligible leads to the Parker bound [133, 134]. For GUT scale monopoles, this bound turns out to be around an order of magnitude stronger than the bound on $\Omega_m h^2$, with the bound being much more severe for lighter monopoles.

Chapter 2

Avoided Deconfinement in Randall-Sundrum Models

This chapter is on the deconfining phase transition in the Randall-Sundrum (RS) model [7]. As discussed in section 1.4.1, the RS model can be understood via its dual description as the deconfined phase of a strongly-coupled large-N CFT. The confinement phase transition is exponentially suppressed by N^2, which means the RS model runs into supercooling bounds in the large-N limit. Large-N is crucial for the RS model to be valid as an effective field theory (EFT), as the the curvature scale is parametrically below the Planck scale in this limit.

Theories described by the RS model in an appropriate limit suffer from a severe cosmological constraint. At high temperature the preferred phase is the AdS-Schwarzschild (AdS-S) solution with a UV brane. Here the Schwarzschild horizon cuts off the geometry in the IR and there is no IR brane. The dual description of the AdS-S phase is the deconfined phase of the theory, while the confined phase is signalled by the presence of the IR brane. The confinement transition corresponds to the appearance of the IR brane from behind the AdS-S horizon [8, 58, 73], and proceeds at a rate suppressed by the factor $\exp\left(-N^2/\lambda\right)$, where λ denotes a possible weak coupling. The confinement scale in the gauge theory is dual to the vacuum expectation value of the radion field which sets the size of the extra dimension in the RS model.

For large-N, the suppressed phase transition is much slower than the expansion rate of the universe, leading to eternal inflation. Requiring the phase transition to complete

leads to an upper bound on N [135]:

$$N \lesssim \sqrt{4\lambda \log \frac{M_{\rm pl}}{\Lambda_c}} \sim 12\sqrt{\lambda}\,. \tag{2.1}$$

where $\Lambda_c \simeq 1$ TeV is the confinement scale for the gauge theory. This bound follows just from dimensional analysis and is independent of the details of the RS model. The ratio $N/4\pi$ sets the hierarchy between the curvature scale k and the 5d reduced Planck scale M_5, $N/4\pi \sim (M_5/k)^{3/2}$ [71]. A small value of this ratio, as implied by the bound (2.1), then means that corrections due to Planck scale physics become important, making the EFT control in the RS model delicate. Gravitational loop corrections can be estimated by the following loop counting parameter,

$$\frac{N_{\rm species} k^3}{16\pi^2 M_5^3} < 1 \Rightarrow N^2 \gtrsim N_{\rm species} \tag{2.2}$$

which is in tension with equation (2.1) even with just the SM degrees of freedom contributing to $N_{\rm species} \sim 100$.

In fact, the bound is much more stringent within the simplest version of the RS model. In this setup, the backreaction of the stabilisation mechanism and breaking of scale invariance are assumed to be small even close to the confinement scale. The gauge theory is an approximately conformal field theory (CFT), with spontaneously broken conformal invariance in the confined phase. The approximate conformality suppresses the phase transition further, making $\lambda \ll 1$, so that the bound on N in equation (2.1) is impossible to satisfy.

There is a large body of work devoted to relaxing this more stringent constraint on the RS model by changing the details of the stabilisation mechanism [136–151] in such a way that $\lambda \simeq 1$ and the phase transition occurs more rapidly. However, the N^2 dependence of the tunnelling rate is a generic feature of the confinement phase transition. While modifying the stabilisation mechanism can change the numerical value of the bound on N, in all these models the phase transition is exponentially suppressed at large-N and therefore subject to the bound in equation (2.1). As pointed out in [152], for Klebanov-Strassler type constructions, the effective value of N itself varies over the extra-dimensional coordinate – the relevant N in this case is the value near the confinement scale.

In this chapter a simple modification to the RS model is presented where N can be made parametrically large without running into this cosmological bound. A scenario is

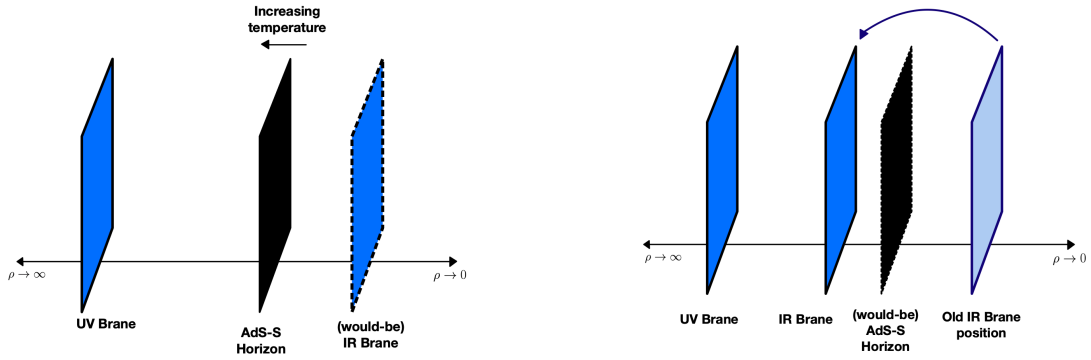

Figure 2.1: Left hand diagram shows the high temperature behaviour of the RS model, while the right hand diagram shows the high temperature behaviour in the AD model. Beyond a certain temperature in the RS model the IR brane is stabilised behind the location of the horizon in the AdS-S phase, indicating that the model is unstable against black hole formation. In the AD model, this instability is lifted by introducing a temperature dependence to the stabilisation mechanism in such a way that the IR brane is stabilised outside the would-be horizon at high temperatures.

constructed where the confinement scale grows with temperature, and hence the universe can remain in the confined phase at all times in early cosmology. For this reason, we call our mechanism avoided deconfinement. In order to achieve this we consider the RS I model with the IR brane stabilised by a Goldberger-Wise (GW) field Φ [72]. By introducing new scalars to the IR brane, we can generate a potential which stabilises the IR brane at high temperatures. The mechanism we use to achieve this is reminiscent of non-restoration of electroweak symmetry at high temperatures, as considered in refs [17, 153–156]. Similar mechanisms have also been proposed to avoid monopoles [157–159] or domain walls [160] in Grand Unified theories, as models of CP violation at high temperature [161, 162], and in the $O(N) \times O(N)$ models of [163, 164].

The modification made to the RS model can lead to dramatic departures from its standard cosmological history. Above a critical temperature T_c, the confinement scale varies almost linearly with temperature T leading to T-dependent mass scales on the IR brane,

$$M_{\rm ir}(T) \propto \mu(T) = \mu(0) \left(\frac{T}{cT_c} \right)^{1/(1+\epsilon)} \tag{2.3}$$

with $\epsilon \ll 1, c \sim \mathcal{O}(1)$. For a mass scale $M_{\rm ir} > T_c$, this can imply that the ratio $T/M_{\rm ir}(T)$ reaches 1 at very high temperatures, or potentially not at all (similar to low reheating temperature models). Taking the standard model (SM) to be localised on the IR brane, the T-dependence of the electroweak and QCD scales is as in equation (2.3). If $v_{\rm ew} > T_c$,

the electroweak phase transition occurs at temperatures far above the TeV scale or is completely avoided. Furthermore, at high temperature, fields localised in the UV of the RS model may have had significant overlap with fields localised towards the IR of the theory, a feature which may have applications to models of baryogenesis and dark matter production.

The initial condition for the mechanism to work is that the universe exits inflation in the RS phase with a stabilized IR brane. A relatively simple way to achieve this is to have inflation with Hubble rate below the confinement scale of the gauge group, or with an additional stabilization of the IR brane during inflation. After inflation the universe reheats and the AD mechanism prevents the brane from falling behind the would-be AdS-S horizon (see figure 2.1). Note that at high enough temperatures the AdS-S phase will still be the preferred thermodynamic phase of the theory, but in the avoided deconfinement model the RS phase is classically stable. The probability of tunnelling from the RS to the AdS-S phase is exponentially suppressed by N^2 factors, and can be made vanishingly small in the large-N limit.

The rest of this chapter is organised as follows. In section 2.1 we describe the early universe cosmology and summarise the details of the confinement phase transition in various generalisations of the RS model that have been considered in the literature. We go on to describe the avoided deconfinement (AD) model in section 2.2 and show how the model leads to a stabilised IR brane at high temperatures. In section 2.3 we present the low energy effective Lagrangian and discuss some of the experimental signatures of the model. In section 2.4 we then discuss the unique early universe cosmology of the model and how this relates to other non-standard cosmological histories in the literature.

In sections 2.5, 2.6 and 2.7 the production of dark matter in the AD model is studied in detail, based on ref. [165]. The non-standard cosmology of the AD model leads to a novel production mechanism, similar to the non-thermal production mechanisms considered in [166–174], where the interactions governing DM production are suppressed because the DM candidate is non-relativistic. This scenario allows for DM production at arbitrarily high masses with $\mathcal{O}(1)$ couplings to the SM, circumventing the usual unitarity bounds on the DM mass [175, 176] and leading to potentially observable signatures in direct and indirect dark matter searches.

2.1 The Supercooled Randall-Sundrum Model

In this section we review the standard cosmology of the RS type I model and Goldberger-Wise field, and its dual gauge theory description via the gauge-gravity duality. In the standard treatment of gauge-gravity duality at finite temperature, the gauge theory partition function is defined on a manifold $\mathcal{M} = S_1 \times R^3$ with the temporal direction compactified on a circle of radius $\beta = \pi/T$. The corresponding gravitational theory is defined on a 5-dimensional manifold with $\mathcal{M}$ as the boundary. In computing the gravitational partition function, all possible geometries Σ which satisfy the boundary condition $\partial\Sigma = \mathcal{M}$ must be integrated over [58]. The partition function will however be dominated by classical gravity solutions. Each semi-classical gravitational solution Σ_i which satisfies the boundary condition is interpreted as a different phase of the CFT. At a given temperature, the geometry which minimises the Euclidean action will give the dominant contribution to the partition function, and therefore correspond to the preferred phase of the CFT.

In the RS model, the UV brane cuts off the AdS space, and hence plays the role of the boundary $\partial\Sigma$. The dual gauge theory is interpreted as a field theory coupled to 4D gravity, defined on the manifold $\mathcal{M}$. One of the possible classical solutions is,

$$ds^2_{\rm RS} = k^2\rho^2 dt^2 - \frac{d\rho^2}{k^2\rho^2} - \rho^2 k^2 dx_i^2, \tag{2.4}$$

with the space in the ρ direction cut off at the position of the IR and UV branes so that $\rho_{\rm ir} < \rho < \rho_{\rm uv}$. Here and throughout this paper, we work in a frame where $\rho_{\rm uv}$ is fixed to the value $\rho_{\rm uv} = k^{-1}$, where k is the AdS curvature. A convenient definition of the temperature of the 5D theory is the local temperature at the UV brane. We will simply refer to this temperature as T. Thermal effects tend to push the IR brane towards the horizon, rendering the RS solution unstable [8] at arbitrarily small temperatures in the absence of stabilization. This instability can be lifted using the GW mechanism [72].

The quasi-conformal theory dual to the RS model is a strongly coupled gauge theory [69, 70] with $\mathcal{O}(N^2)$ degrees of freedom, where N can be determined by matching the entropy of the black hole with the entropy of the high temperature phase of the gauge theory [71],

$$\frac{N^2}{16\pi^2} \simeq 12\left(\frac{M_5}{k}\right)^3, \tag{2.5}$$

where M_5 is the bulk Planck scale. This relation can be modified by $\mathcal{O}(1)$ factors depending on strong coupling effects in different gauge theory models. We see that the large-N aspect of the 4D gauge theory is a crucial feature of these models, since it corresponds to the hierarchy between the curvature scale k and the 5D Planck scale M_5 in the 5D gravitational theory. The ρ direction can be thought of as the RG scale of the conformal theory, with small ρ corresponding to the IR of the theory. The UV and IR branes of the RS model correspond to UV and IR cut-offs in the gauge theory. The cutoff at the IR brane represents a spontaneous breaking of conformality in the IR due to confinement in the gauge theory, while the UV brane represents explicit breaking by the cutoff at the Planck scale [71]. The RS model with the IR brane therefore corresponds to the confined phase of the conformal theory. The GW mechanism corresponds to introducing a nearly marginal operator to the CFT which explicitly breaks the conformal symmetry of the theory. The coupling of this operator is dual to a scalar field in the RS model with a small bulk mass. Introducing the GW scalar generates an effective potential for the radion (identified with $\mu = k^2\rho_{\rm ir}$ in co-ordinates where the location of the UV brane is fixed [177]), with a minimum at small μ – the IR brane will then be stabilised at the minimum of this potential.

The RS solution with the IR brane becomes classically unstable at high temperatures. There is another classical solution that contributes to the finite temperature partition function given by the AdS-Schwarzschild (AdS-S) geometry,

$$ds^2_{\rm AdS-S} = f(\rho)dt^2 - \frac{d\rho^2}{f(\rho)} - \rho^2 k^2 dx_i^2, \quad f(\rho) = k^2\left(\rho^2 - \frac{\rho_h^4}{\rho^2}\right). \tag{2.6}$$

The position of the horizon ρ_h is set by the temperature $\rho_h = \pi T/k^2$. The solution is cut off at $\rho = \rho_{\rm uv}$ by the UV brane as before. The AdS-S solution is dual to the deconfined phase of the gauge theory, with the Hawking temperature and entropy of the AdS black hole equal to the corresponding quantities in the gauge theory. The AdS-S solution is classically stable for any non-zero temperature, and is the thermodynamically preferred phase of the theory at high temperatures.

As the universe cools below a critical temperature, the RS phase with the IR brane becomes preferred and there is a first order phase transition between the two phases which proceeds through a tunnelling process connecting the two solutions. This tunnelling process

is strongly suppressed, however, due to the large change in free-energy in the two phases. The requirement that this phase transition completes places bounds on N for the model to be cosmologically viable. These bounds typically require $N \sim \mathcal{O}(1)$, which is in tension with the assumption of working in the large-N limit.

2.1.1 (De)confinement Phase Transition in the RS Model

We consider the RS model with the GW stabilization mechanism. The bulk Lagrangian contains gravity and the GW field (Φ),

$$S_{\text{bulk,RS}}[G_{AB}, \Phi] = \int d^4x\, d\rho\, \sqrt{G} \left[-2M_5^3 R + 24 M_5^3 k^2 + \frac{1}{2} G^{AB} \partial_A \Phi \partial_B \Phi - \frac{1}{2} m_\Phi^2 \Phi^2 \right] . \tag{2.7}$$

We also include brane localized terms,

$$S_{\text{uv,RS}} = \int d^4x \sqrt{-g_{\text{uv}}} \left[-\lambda_{\text{uv}} (\Phi^2 - v_{\text{uv}}^2)^2 - 24 M_5^3 k + \delta\Lambda_{\text{uv}} \right] \tag{2.8}$$

$$S_{\text{ir,RS}} = \int d^4x \sqrt{-g_{\text{ir}}} \left[-\lambda_{\text{ir}} (\Phi^2 - v_{\text{ir}}^2)^2 + 24 M_5^3 k + \delta\Lambda_{\text{ir}} \right] . \tag{2.9}$$

where $g_{\text{uv,ir}}$ are the induced metrics on the UV and IR branes. In the presence of the GW stabilization mechanism, only one combination of the brane tension detuning parameters $\delta\Lambda_i$ needs to be tuned, corresponding to the tuning of the 4D cosmological constant. Depending on the sign of m_Φ^2, these parameters may be required to lie in a certain range for there to be a local minimum for the radion away from $\mu = 0$. For simplicity, here we set each of the detuning parameters to 0 and assume $m_\Phi^2 > 0$. We also assume that the stabilization occurs in the limit of small backreaction. These assumptions are not crucial and do not affect the qualitative results. With these assumptions, the metrics in equations (2.4) and (2.6) continue to be approximate classical solutions.

We can obtain the potential for the radion by integrating over the classical solution for the GW field. In the limit where the brane localized terms fix $\Phi(\rho_{\text{uv,ir}}) = v_{\text{uv,ir}}$, the 4D effective potential for the radion, $\mu \equiv k^2 \rho_{\text{ir}}$ is [8],

$$V(\mu) = \epsilon v_{\text{uv}}^2 k^4 + \left[(4 + 2\epsilon) \mu^4 (v_{\text{ir}} - v_{\text{uv}} (\mu/k)^\epsilon)^2 - \epsilon v_{\text{ir}}^2 \mu^4 \right] + \mathcal{O}(\mu^8/k^4) , \tag{2.10}$$

with $\epsilon = \sqrt{4 + m_\Phi^2/k^2} - 2$. The minimum is obtained for:

$$\mu_{\rm TeV} = f(\epsilon) k \left(\frac{v_{\rm ir}}{v_{\rm uv}}\right)^{1/\epsilon}, \tag{2.11}$$

$$f(\epsilon) = \left[\frac{4 + \epsilon + \sqrt{\epsilon(4+\epsilon)}}{4 + 2\epsilon}\right]^{1/\epsilon} \sim \mathcal{O}(1)\,. \tag{2.12}$$

A relatively modest hierarchy in $v_{\rm uv,ir}$ and $\epsilon \sim 1/10$ can generate an exponential hierarchy between k and $\mu_{\rm TeV}$. At energies $\lesssim \mu_{\rm TeV}$ the effective theory is a 4D theory with a tower of Kaluza-Klein (KK) states with masses $\sim \mu_{\rm TeV}$. In the 4D theory, dimensionful parameters involving fields localized on the IR brane, such as the Higgs mass parameter, scale with $\mu_{\rm TeV}$, thus explaining the electroweak hierarchy elegantly.

At low-temperatures, $T < \mu_{\rm TeV}$, both classical solutions – the stabilized RS solution with UV and IR branes, and the AdS-S solution with a UV brane and a black hole horizon – are (meta)stable. However, at high-temperatures $T \gg \mu_{\rm TeV}$, the minimum of the radion potential is behind the AdS-S horizon $\mu_{\rm TeV} < \rho_h k^2$, indicating that the AdS-S solution is the only classical solution. During the early universe the universe is in the AdS-S phase; to get to the RS phase the universe needs to undergo a first order phase transition.

The tunnelling rate per unit volume for the phase transition is,

$$\Gamma \simeq R_c^{-4} \exp(-S_b) \tag{2.13}$$

where S_b is the bounce action for the tunnelling transition, and R_c is the radius of the critical bubble [75, 78]. The field configuration for the transition from the AdS-S phase to the RS phase involves moving the black hole horizon to the far IR, $\rho_h \to 0$, and then nucleating the IR brane at $\rho = 0$ and bringing it to larger values of ρ. Therefore this field configuration probes the geometry in the region where the local temperature is super-Planckian and stringy corrections would be relevant. However, in the case where the transition temperature is low, and there is an approximate conformal symmetry in the IR, the dominant contribution to the bounce is dictated by the radion dynamics and can be estimated while ignoring the gravitational contribution to the bounce [151]. Even so, since the field configuration probes the geometry in the far IR, the bounce action for this configuration can depend sensitively on the details of the GW stabilisation, and

other physics in the IR. We summarize the results for the bounce action that have been considered in various limits in the literature next.

2.1.2 Bounce action from the radion

In a large class of models, the phase transition is captured by the dynamics of the radion [8, 147, 151]. The general radion effective field theory can be understood in terms of the dual 4D theory. The 4D theory is a near-conformal field theory coupled to gravity. The gravitational sector breaks the conformal symmetry explicitly, but below the gravitational cutoff an approximate conformal symmetry survives. For a stabilised RS geometry with a light radion, the 4D effective theory below the KK scale $\mu_{\rm TeV}$ is well-described by an effective theory of a spontaneously broken (approximate) conformal symmetry, with the light radion/dilaton as the pseudo-Nambu-Goldstone boson.

In this section we work in this 4d picture to study a few such generalisations that have been studied in the literature. As we will see, in each case the first order phase transition is highly suppressed. The effective Lagrangian for the dilaton [8, 178] can be written as,

$$\mathcal{L}_{\rm eff} = \frac{N^2}{16\pi^2}\left[(\partial\mu)^2 - \lambda(g(\mu))\mu^4\right] , \tag{2.14}$$

where the μ-dependence in $g(\mu)$ denotes the explicit breaking of conformal symmetry due to the GW deformation. We expect the dilaton to be the lightest bound state of the gauge theory [179, 180] as it is the pNGB of the broken dilation symmetry, so is the only relevant degree of freedom in the IR of the theory. The N^2 factor makes explicit the fact that the dilaton is interpreted as a glueball state in a 4D large-N gauge theory.

The free energy in the (de)confined phase is well approximated by,

$$\begin{aligned} F_{\rm confined} &= V(\mu_{\rm TeV}) = -\frac{N^2}{16\pi^2}\lambda_{\rm TeV}\mu_{\rm TeV}^4 + V_0 \\ F_{\rm deconfined} &= C - 2\pi^4(M_5/k)^3T^4 = C - \frac{\pi^2}{96}N^2T^4 \end{aligned} \tag{2.15}$$

where we have defined $\lambda_{\rm TeV} \equiv |\lambda(g(\mu_{\rm TeV}))|$, and added a constant V_0 to ensure that the vacuum energy at the minimum is zero. Notice that $\lambda(g(\mu_{\rm TeV})) < 0$ for $\mu_{\rm TeV}$ to be the minimum of the potential. C can be calculated by matching the free energy at

$\mu = T = 0$. The critical temperature can be calculated by equating the free energy in the two phases at the transition,

$$C - \frac{\pi^2}{96} N^2 T_c^4 \simeq -\frac{N^2}{16\pi^2} \lambda_{\rm TeV} \mu_{\rm TeV}^4 + V_0 \tag{2.16}$$

$$\Rightarrow T_c \simeq \left[\frac{6\lambda_{\rm TeV}}{\pi^4}\right]^{1/4} \mu_{\rm TeV} \,. \tag{2.17}$$

When $\lambda_{\rm TeV} \ll 1$, the transition temperature $T_c \ll \mu_{\rm TeV}$, and the approximation of radion domination is well justified.

If the phase transition is prompt, it completes for $T \sim T_c$. In this case the bubble has O(3) symmetry, and the action can be estimated in the thin-wall regime (see e.g. [135]),

$$\frac{S_3}{T} \sim \frac{N^2}{8} \left[\frac{1}{\lambda_{\rm TeV}}\right]^{3/4} \frac{T_c}{T} \left(1 - \left(\frac{T}{T_c}\right)^4\right)^{-2} \,. \tag{2.18}$$

This explicitly shows the general enhancement of the bounce action by N^2, and often also by the weak coupling $\lambda_{\rm TeV}$.

We can evaluate the bounce action for the GW model considered in section 2.1.1 above. The quartic $\lambda_{\rm TeV}$ in this case is,

$$\lambda_{\rm TeV} = \frac{16\pi^2}{N^2} \epsilon^{3/2} v_{\rm ir}^2 \tag{2.19}$$

which leads to the following parametric form for the bounce action [8],

$$\frac{S_3}{T} \sim \frac{N^{7/2}}{\epsilon^{9/8} v_{\rm ir}^{3/2}} \frac{T_c}{T} \left(1 - \left(\frac{T}{T_c}\right)^4\right)^{-2} \,. \tag{2.20}$$

The action is not only enhanced by the factor of N^2, but also by the small quartic coupling of the radion, which increases the dependence on N to $N^{7/2}$. There is an additional enhancement by $1/\epsilon$, related to the fact that the scale symmetry violation at $\mu_{\rm TeV}$ is parametrised by ϵ. The exact power of ϵ that appears can depend on the implementation of the GW mechanism [8, 137, 147, 151].

More generally, we can see that the action is enhanced for small scale symmetry violation encoded in $\beta_\lambda \ll 1$. The zero temperature minimum is determined by the running quartic, $\lambda(g(\mu))$,

$$\partial V(\mu)/\partial\mu = [4\lambda(g(\mu_{\rm TeV})) + \beta_\lambda(g(\mu_{\rm TeV}))]\mu^3 = 0 \,. \tag{2.21}$$

Thus for a nearly scale invariant theory at $\mu_{\rm TeV}$, $\lambda_{\rm TeV}$ will be generically small.

If the transition is not prompt, then it will then take place in the supercooled regime, $T \ll T_c$. In the case where there is a barrier in the radion potential between $\mu_{\rm TeV}$ and $\mu \sim 0$, the bounce configuration is essentially the same as the zero temperature tunnelling, and has an O(4) symmetric bounce action [8, 137]

$$S_4 \sim \frac{N^2}{16\pi^2 \lambda_{\rm TeV}}. \tag{2.22}$$

As before, the explicit factor N^2 appears. Again, we see that in the case of the simplest RS+GW model above, the parametric dependences are even stronger,

$$S_4 \sim \frac{N^4}{(4\pi)^4 \epsilon^{3/2} v_{\rm ir}^2}. \tag{2.23}$$

If there is no barrier between $\mu \sim 0$ and $\mu = \mu_{\rm TeV}$, then the "release point" for the radion field can be very small $\mu \sim T$ even for supercooled transition, so the smallest bounce action is still obtained by an O(3) symmetric bounce. For example, in the case where conformal symmetry is restored in the IR ($\epsilon > 0$ for the GW field) [147], the radion potential near the origin is $V \sim \lambda(0)\mu^4$. The bounce action is then the $T \ll T_c$ limit of equation (2.18),

$$\frac{S_3}{T} \sim \frac{N^2}{8[\lambda(0)]^{3/4}} \tag{2.24}$$

which is no longer suppressed by the small parameter ϵ. In the case where $\epsilon \lambda_{\rm TeV}$ is not parametrically small, radion dynamics no longer suffice to estimate the bounce. However, it may still be possible to estimate the bounce in the 5D effective theory [151] and is found to be $\mathcal{O}(N^2)$.

When $\epsilon < 0$, the GW field profile grows towards the IR. Consequently, the higher order terms in the GW potential might become important and the approximate conformality $\partial_{\log \mu} g(\mu) \sim \epsilon$ might be broken as we approach $\mu \lesssim \mu_{\rm TeV}$. In such cases the enhancement of the bounce action by $1/\epsilon$ will be absent, even though the EW/Planck hierarchy is set by small epsilon. This can be explicitly seen in explicit holographic constructions [152, 181], or in RS models with more general stabilisation mechanisms [137–148, 150, 151].

We see from the examples above that while the details of the bounce action depend on the actual theory, it takes the form $S_b \simeq N^2/\lambda$ in each case, with $\lambda \lesssim 1$. This has far-reaching consequences for early universe cosmology. Either the universe is required

to be reheated to temperatures lower than the confinement scale, or there is a strong constraint on the maximal N allowed.

If the rate of tunnelling is smaller than Hubble, the universe will get stuck in the false vacuum [79]. Since the true vacuum at zero temperature is assumed to have a (nearly) vanishing cosmological constant, the deconfined vacuum has a large positive cosmological constant $C \sim N^2 T_c^4$ at low temperatures and starts to inflate with $H \simeq N T_c^2 / M_{\rm pl}$. In a Hubble volume, the probability of completing the phase transition within a Hubble time is,

$$P = \Gamma / H^4 \tag{2.25}$$

If $P \ll 1$, then the universe eternally inflates. This gives us a bound on N,

$$N \lesssim 2\sqrt{\lambda \log \frac{M_{\rm pl}}{T_c}} \tag{2.26}$$

We have replaced the inverse critical radius by T_c; unless the bubble size is exponentially smaller, this is a reasonable approximation. In many models considered above, λ is parametrically small. For the RS+GW model above, S_b is enhanced both by N as well as $1/\epsilon$, making it impossible to satisfy the constraint above. Even without these enhancements, the calculations above assume dilaton dominance, which requires $\lambda_{\rm TeV} \ll 1$ [147]. Therefore, it is hard to get $S_b \lesssim N^2$ in a controlled approximation. This translates into a bound $N \lesssim 12$ for $T_c \sim 1\,\text{TeV}$. From equation 2.5, we see that the hierarchy between the 5D Planck scale and the AdS curvature is $(M_5/k) \lesssim 1$. This lack of hierarchy makes the 5D effective gravitational theory very delicate.

One avenue to evade this cosmological bound is to avoid reheating the universe above the TeV scale. This may require a more intricate inflationary mechanism, as well as solutions to baryogenesis at the electroweak scale or below [142, 143, 154]. In the next section we outline the avoided deconfinement mechanism, where the GW stabilisation of the radion is temperature dependent and the IR brane is stabilised at arbitrarily high temperatures. This allows for parametrically large hierarchies between M_5 and k, and an early cosmology without a stringent restriction on the reheat temperature.

2.2 5D Model for Avoided Deconfinement

In this section we modify the RS model with GW field (Φ) by including extra scalars localised to the IR brane[1]. Given a suitable set of parameters, the effect of this will be to realise a model where the new scalars provide a metastable minimum for the radion at high temperature, avoiding the formation of the AdS-S black hole.

We make a simple modification to the RS model described in equation (2.9) by adding scalar field(s) S to the IR brane. The action is:

$$S = S_{\text{bulk,RS}} + S_{\text{uv,RS}} + S_{\text{ir,RS}} + S_{\text{ir,AD}} \,. \tag{2.27}$$

where $S_{\text{bulk,RS}}$ and $S_{\text{uv/ir,RS}}$ are the RS model bulk and brane actions which are unchanged from their definition in equations (2.7), (2.8),and (2.9). We continue to choose the detuning parameter $\delta\Lambda_{\text{ir}} = 0$. As usual, this simplifying assumption can be relaxed. The modified IR brane action, $S_{\text{ir,AD}}$ includes N_s real scalars S localised to the brane. The additional terms in the IR brane action is

$$S_{\text{ir,AD}} = k^4 \int_{\rho=\rho_{\text{ir}}} d^4x \sqrt{-g_{\text{ir}}} \sum_{i=1}^{N_s} \left[\frac{1}{2k^2} g_{\text{ir}}^{\mu\nu} \partial_\mu S_i \, \partial_\nu S_i - \frac{\lambda_s}{4}(S_i^2 - v_s^2)^2 - \frac{\gamma}{6} S_i^3 \right], \tag{2.28}$$

where we have explicitly included factors of k so that the parameters λ_s, γ, v_s as well as the field S are dimensionless. We will suppress the index i on S for notational simplicity. In order for the potential to remain bounded from below, the coupling λ_s must be positive. The value of the masses and quartic couplings of each field S do not have to be equal, but for simplicity we will take them to be the same. For unequal couplings our results below can be reinterpreted using statistical averages over the S ensemble. Each S has an approximate Z_2 symmetry that is spontaneously broken at zero temperature. The coupling γ that weakly breaks the Z_2 symmetry for each S is introduced to avoid domain wall problems, and can be very small in a technically natural way.

Before presenting the consequences of adding these extra scalars, we summarize the choice of parameters for which our approximations are under theoretical control. The primary goal of the AD setup is to generate a classically stable minimum for the radion

[1]Localised fields on the IR brane may be required to arise from corresponding bulk modes with masses below the 5D cutoff [182]. These bulk modes will then have an associated tower of KK states, but this detail will not affect our discussion.

at high temperatures for arbitrary N, therefore avoiding a confinement phase transition entirely and putting the large-N approximation on a firmer footing. It is then worth highlighting the validity of the large-N expansion, especially in light of adding extra matter on the IR brane. Requiring the gravitational loop counting parameter to be small, $N_{\text{species}}/N^2 \lesssim 1$, restricts the number of scalars we can add. As we show below, the AD mechanism does require $N_s > 1$ to operate. However, in order to obtain a classically stabilized radion at high temperatures, N_s can be parametrically smaller than N^2. In this case, the black hole phase does have a lower free energy, but the tunnelling rate from the AD phase to the black hole phase is exponentially suppressed by a tunnelling exponent of order $\sim N^3$. Thus, the parameter N can be taken arbitrarily large while keeping other parameters in our model fixed, ensuring that the $1/N$ expansion is well under control.

In order to understand the other parametric scalings in the Lagrangian, it is useful to characterize the cosmological history of the AD model by the following three scales:

1. the temperature T_s at which the scalars S undergo a (crossover) phase transition;

2. the temperature T_c at which the AD construction begins to take effect and the position of the IR brane begins to vary with temperature; and

3. the zero-temperature radion vev, μ_{TeV}.

The AD model requires the hierarchy $T_s < T_c$, due to the fact that the addition of the new scalars S only generates the desired finite-temperature effects in the symmetric phase. At temperatures $T > T_c$ the position of the IR brane is moved from the GW minimum due to thermal effects. As mentioned above, in this temperature range the confined phase is metastable, in contrast to the usual RS model where the confined phase becomes classically unstable at high temperature. Another condition on the parameter space comes from the requirement that the IR brane is stabilized at a radius where the local temperature is small enough such that the backreaction on the bulk geometry is small. At the confinement scale, this condition implies

$$T_c < \frac{\mu_{\text{TeV}}}{\pi}, \tag{2.29}$$

This condition becomes stronger logarithmically in temperature, and can fail at very high temperatures, which sets a maximum temperature $T_{\max}$ for the AD mechanism to operate. As we explain in further detail in section 2.2.2, this leads to the following condition on the parameters of the model:

$$1 > \frac{\pi T_c}{\mu_{\rm TeV}} > \sqrt{\frac{6}{N_s}}\frac{m_\varphi}{m_s} > v_s \tag{2.30}$$

where m_φ, m_s are the masses of the radion and scalar (s) fluctuations at zero temperature. Since the mass of the radion m_φ cannot be too small phenomenologically, this leads us to require a moderately large number of scalar fields N_s for the AD model to work.

2.2.1 Finite temperature effective potential for the radion

We work in a regime where the local 5D temperature remains below $(M_5^3 k^2)^{1/5}$ everywhere in the 5th dimension, so that the finite temperature effects have a negligible backreaction effect on the bulk geometry. At any temperature T and the position of the IR brane $\rho_{\rm ir}(T)$, we can solve the equations of motion for the GW field on the background RS metric with the same boundary conditions, $\Phi(\rho_{\rm ir/uv}(T)) = k^{3/2} v_{\rm ir/uv}$. The bulk solution is,

$$\Phi(\rho) = A\rho^{-4-\epsilon} + B\rho^{\epsilon} \tag{2.31}$$

where A, B are fixed by the boundary conditions. As above, $\epsilon \approx m_\Phi^2/(4k^2)$, which we take to be positive. We expand in fluctuations around this classical solution with the size of the extra dimension equal to $\rho_{\rm ir}(T)$. We decompose the bulk fluctuations into Kaluza-Klein modes and integrate over the 4D modes to derive the finite temperature effective potential.

The temperature-dependent effective potential can be broken up into the tree-level potential and the one-loop potential [34, 35]:

$$V_{\rm eff}(T) = V_{\rm tree} + \Delta V_1^{\rm CW} + \Delta V_1^T(T) \tag{2.32}$$

where we have separated the 1-loop contribution into a piece that goes to 0 at zero temperature $\Delta V_1^T(0) = 0$. The zero temperature Coleman-Weinberg potential, $\Delta V_1^{\rm CW}$ includes the usual UV-divergences one would encounter in these calculations. The tree-level 4D action is obtained as above by integrating the classical solution over the extra

dimension. The potential is given by,

$$V_{\rm tree}(\mu, S_i) = \mu^4 \left[(4+2\epsilon)(v_{\rm ir} - v_{\rm uv}(\mu/k)^\epsilon)^2 - \epsilon v_{\rm ir}^2 + \sum_{i=1}^{N_s} \left(\frac{\lambda_s}{4}(S_i^2 - v_s^2)^2 + \frac{\gamma}{6} S_i^3 \right) \right] \quad (2.33)$$

where we have used $\mu = k^2 \rho_{\rm ir}(T)$. We have also suppressed the T-dependence in the notation.

The one-loop contribution is obtained by integrating over the fluctuations. The finite temperature contribution to the potential depends on the effective mass of the fluctuations around the classical solution. The relevant particles in our case are the radion, the new scalars and the SM fields. Including the kinetic term for the radion [178, 183] and the scalars, we find the following action for the fluctuations:

$$S = \int d^4x \left[\mathcal{L}_{\rm SM} + \frac{1}{2}(\partial\varphi)^2 + \frac{1}{2}(\partial s_i)^2 - V_{\rm tree}\left(\mu \left(1 + \frac{\varphi}{F_\varphi} \right), S_i + \frac{s_i}{\mu} \right) \right] \quad (2.34)$$

We have introduced the canonically normalized fluctuations for the radion φ and the scalars s. The radion decay constant

$$F_\varphi = \frac{N}{2\sqrt{2}\pi}\mu. \quad (2.35)$$

The indices in the kinetic term are now contracted with the 4d Minkowski metric.

The field-dependent masses of these particles are defined as the second derivative of the potential w.r.t. the corresponding field. The SM particle masses and the radion and s masses all scale with μ. For a large number of scalars $N_s \gg 1$, the thermal potential is dominated by loops of ${s_i}^2$. The field-dependent masses of s_i are,

$$m_{s,i}^2 = \mu^2 \left[-\lambda_s v_s^2 + 3\lambda_s S_i^2 + \gamma S_i \right] \quad (2.36)$$

The other modes in the spectrum are the KK modes of the graviton, the GW field and other fields in the bulk. The mass of the nth KK mode is approximated by [184]:

$$m_n \simeq \left(n + \frac{2+\epsilon}{2} - \frac{3}{4} \right) \pi\mu. \quad (2.37)$$

The ρ-coordinate of the would-be AdS-S horizon is $\rho_h = \pi T/k^2$. Therefore, the condition that the IR brane is stabilised outside the AdS-S horizon, $\rho_{\rm ir}(T) > \rho_h$ implies that the higher KK modes are not excited at any T, and can be safely neglected in the thermal potential.

[2] Note that since the SM contribution to the μ potential is proportional the mass of the SM field, only the contributions from t, W, Z, h are sizeable.

The Coleman-Weinberg potential is given by,

$$V_1^{\rm CW}(\mu, S_i) = \sum_{i=1}^{N_s} \frac{1}{64\pi^2} m_{s,i}^4 \left(\log \left[\frac{m_{s,i}^2}{\mu_R^2} \right] - \frac{3}{2} \right) \tag{2.38}$$

where μ_R is a renormalisation scale. A convenient choice of the renormalisation scale for the dynamics on the IR brane is μ itself [185]. With this choice, we do not generate large hierarchies of scale on the IR brane and the one-loop corrections at zero-temperature stay small. We have included all terms allowed by the scale symmetry of the radion and the Z_2 symmetries in the s-sector, as well as leading terms violating these symmetries parameterized by the small parameters ϵ, γ. Thus, the higher order terms can be safely neglected and we will simply absorb the UV divergent pieces into a redefinition of couplings and masses as renormalized quantities.

The finite-temperature one-loop contributions from s_i are

$$\Delta V_1^T(\mu(T), S_i(T), T) = \sum_{i=1}^{N_s} \frac{T^4}{2\pi^2} \int dk\, k^2 \log \left[1 - \exp \left(-\sqrt{k^2 + \frac{m_{s,i}^2(\mu, S_i)}{T^2}} \right) \right] \tag{2.39}$$

$$\equiv \sum_{i=1}^{N_s} \frac{T^4}{2\pi^2} J_b \left(\frac{m_{s,i}^2(\mu, S)}{T^2} \right) \tag{2.40}$$

We approximate the thermal function J_b by assuming that $m_s(T) \ll T$. At high temperature the thermal function can be approximated as,

$$J_b(y^2) \approx -\frac{\pi^4}{45} + \frac{\pi^2}{12} y^2 - \frac{\pi}{6} y^3 - \frac{1}{32} y^4 \left(\log \frac{y^2}{\pi^2} + 2\gamma_E - \frac{3}{2} \right) . \tag{2.41}$$

where γ_E is the Euler-Mascheroni constant. The field-dependent log pieces cancel between the Coleman-Weinberg terms and the thermal corrections. The renormalisation scale $\mu_R \simeq \mu$ scales with the temperature (as we show below), and hence we do not get any enhanced large-log pieces, and we can safely ignore the terms of $\mathcal{O}(y^4)$. Then,

$$\begin{aligned} \Delta V_1^T(\mu, S, T) \simeq & \frac{N_s}{24} T^2 \mu^2 \left(-\lambda_s v_s^2 + 3\lambda_s S^2 + \gamma S \right) \\ & - \frac{N_s}{12\pi} T \mu^3 \left(-\lambda_s v_s^2 + 3\lambda_s S^2 + \gamma S + \lambda_s \frac{T^2}{4\mu^2} \right)^{3/2} \end{aligned} \tag{2.42}$$

where we have used the fact that each of the scalar vevs $S_i = S$ when $\{\lambda_s, v_s, \gamma\}$ are taken to be the same for each s_i. The extra term involving T^2 in the second term above is a result of performing the leading daisy resummation, where we replace the

field-dependent mass $m_{s,i}^2$ by $m_{s,i}^2 + \Pi_i$ in equation (2.40), with Π_i the leading temperature contribution to the one-loop thermal mass.

Thus, we see that at high temperatures $T > T_s \simeq \frac{1}{2} v_s \mu_{\rm TeV}$, thermal effects drive to restore the (approximate) Z_2 symmetry in S, so that $\langle S \rangle \ll 1$. This generates a tachyonic direction for μ, providing a finite temperature stabilization. As the universe cools, the S symmetry gets broken, and the radion settles down close to its zero temperature minimum dictated by the GW part of the potential. The thermal potential can be minimized numerically, and for a range of parameters the radion remains stabilized outside the would-be AdS-S horizon at high temperatures.

2.2.2 High temperature radion stabilization

The minimum of the radion potential can be simply approximated in two distinct regimes:

$$\mu(T) = \begin{cases} \mu_{\rm TeV} & T < T_c \\ \mu_{\rm TeV} \left(\frac{T}{cT_c}\right)^{\frac{1}{1+\epsilon}} & T \gg T_c \end{cases} \tag{2.43}$$

where the constant c is given by:

$$c^2 = \frac{4 v_{\rm uv}^2}{\epsilon^{3/2} v_{\rm ir}^2} \left(\frac{\mu_{\rm TeV}}{k}\right)^{2\epsilon} \tag{2.44}$$

The zero temperature value of the radion minimum $\mu_{\rm TeV}$ is well approximated by equation 2.11, up to an $\mathcal{O}(\gamma v_s^3)$ correction to the μ^4 co-efficient which is a result of the potential for S not vanishing at the zero-temperature minimum. The transition temperature T_c is is the temperature at which the radion starts to move and is given by,

$$T_c^2 \simeq \frac{6}{N_s} \frac{m_\varphi^2}{m_s^2} \mu_{\rm TeV}^2 = \frac{24 \mu_{\rm TeV}^2}{N_s (\lambda_s v_s^2)} \epsilon^{3/2} v_{\rm ir}^2 \tag{2.45}$$

where m_φ, m_s here are the zero-temperature masses for φ, s. Since $\mu(T)/T$ is slowly growing, there is a maximum temperature $T_{\rm max}$ beyond which the IR brane would fall behind the horizon,

$$T_{\rm max} \sim \mu(T_{\rm max})/\pi \Rightarrow T_{\rm max} = \frac{\mu_{\rm TeV}}{\pi} \left(\frac{\mu_{\rm TeV}}{\pi c T_c}\right)^{1/\epsilon} \tag{2.46}$$

This sets a (mild) bound on the reheat temperature of the universe. This is at an exponentially high scale for $\delta \equiv \pi T_c / \mu_{\rm TeV} \ll 1/c$. The AD transition temperature should

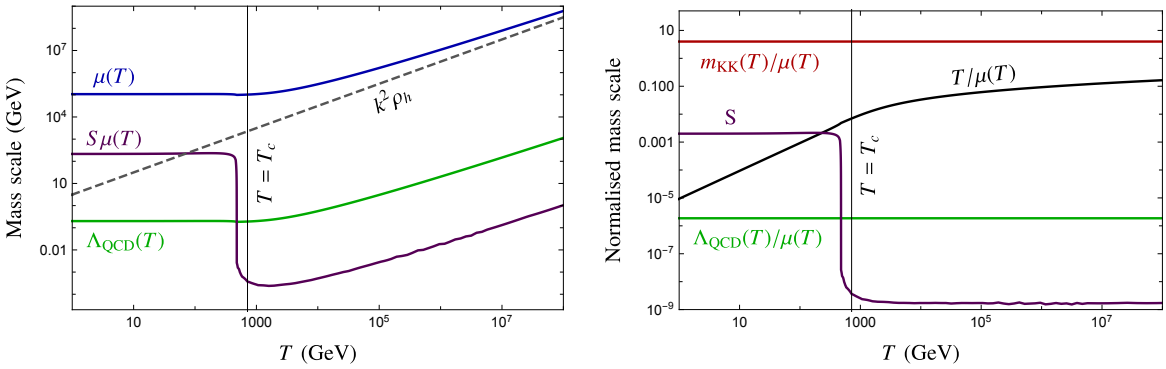

Figure 2.2: Plots showing the dependence of mass scales in the theory with temperature, for parameters in equation (2.48). The left plot shows the radion expectation value (μ), the scalar expectation value ($S\mu$) and the QCD scale, while the second plot shows the same quantities and the KK scale with the dependence on the radion factored out. The vertical line shows the critical temperature $T_c \sim 700$ GeV. The dashed black line in the first plot shows the horizon location $k^2\rho_h$ as a function of temperature.

also be higher than the Z_2 symmetry restoration temperature, $T_c > T_s$. These two requirements give us the following inequalities on our parameter space,

$$\delta > \sqrt{\frac{6}{N_s}}\frac{m_\varphi}{m_s} > v_s \tag{2.47}$$

For illustration, we choose the following benchmark values[3]

$$\begin{aligned}\big\{k = 6\times 10^{16}\text{GeV}, \epsilon = 4.13\times 10^{-2}, v_{\rm uv} = 10^{-3}, v_{\rm ir} = 3\times 10^{-4},\\ N_s = 100, \lambda_s = 1, v_s = 2\times 10^{-3}, \gamma = -10^{-8}\big\}\,,\end{aligned} \tag{2.48}$$

and find the following parameters

$$\mu_{\rm TeV} \simeq 1.8\times 10^{-12} k \simeq 100 \text{ TeV} \tag{2.49}$$

$$T_c \simeq 700 \text{ GeV}\,. \tag{2.50}$$

The maximum temperature $T_{\rm max}$ for this case is around 5×10^{11}GeV. The temperature evolution of various scales in this benchmark is illustrated in figure 2.2.

Comparing the AD model to the usual RS model, the high temperature behaviour is vastly different. In the RS model, as we move to high temperature, thermal effects drive the IR brane towards the AdS boundary, where it eventually collapses to form an AdS-S black hole [186]. The model then remains in the black hole phase until tunnelling to the RS phase

[3]The value of ϵ was chosen such that $\mu_{\rm TeV} \simeq 100$ TeV. A more generic choice works equally well.

through a first order phase transition which is highly suppressed in calculable models, as was shown in section 2.1. In contrast, the model presented here describes a situation where the IR brane is stabilised closer to the UV end of the warped direction at high temperatures, then falls approximately linearly with temperature into the IR before stabilising at a constant value deep in the IR as in the RS case. It should be noted that at very high temperatures, the black hole phase can still have a lower free energy than the AD phase, but the IR brane remains meta-stabilised. The only way the system can transition to the black hole phase is through a first order phase transition which is exponentially suppressed.

The AD model also introduces a novel temperature dependence of the mass scales on the IR brane, which scale linearly with the radion. Assuming that the SM is confined to the IR brane, the left panel of figure 2.2 shows the dependence of the QCD scale with temperature in the AD model. The other dimensional parameters of the SM, such as the electroweak vacuum value, exhibit a similar scaling above the critical temperature, T_c, of the theory. Above T_c the temperature only increases marginally relative to the other scales of the theory. This leads to the KK modes being frozen out to arbitrarily high temperature, as shown in the right panel of figure 2.2. A similar behaviour would occur for any other scales of the theory which are above T_c – they are frozen out to much higher temperatures than in the usual RS model. In section 2.4 we discuss this behaviour and its potential implications for BSM phenomenology in more detail.

2.3 Low Temperature Phenomenology

In this section we show we study the constraints on the avoided deconfinement model from collider results and ALP searches. For simplicity we have assumed that the SM is confined to the IR brane. More realistic models typically have some or all SM fields propagating in the bulk, which can offer an explanation of the hierarchical Yukawa couplings in the SM [184,187,188] but also lead to new constraints from flavour-violating processes [189,190]. The constraints on the RS model have been well-studied. Here we will focus on the new features that are required for the AD mechanism to work.

The qualitative features that the mechanism requires can be estimated using the inequality in equation 2.30. For $\delta \ll 1$, we need,

$$\begin{aligned} \frac{m_s}{\mu_{\rm TeV}} &\simeq v_s < \delta \\ \frac{m_\varphi}{\mu_{\rm TeV}} &< \delta^2 \sqrt{N_s}\,. \end{aligned} \tag{2.51}$$

Experimental constraints on a very light radion will lead us to require a large number of scalars, $N_s \gg 1$, with masses below the confinement scale.

In section 2.3.1 we write down the effective Lagrangian – the relevant degrees of freedom being the SM fields, the radion φ, and the AD scalar(s) s. We ignore higher dimensional operators which arise from integrating out KK modes and $1/N$ suppressed stringy corrections, taking these to be negligible. In section 2.3.2 we then describe the dominant experimental constraints in different regions of parameter space.

2.3.1 Effective Lagrangian at zero temperature

The tree-level interactions of the radion φ with the SM fields can be written compactly by the replacing the mass terms in the SM by a φ dependent mass,

$$\mathcal{L}^{(\rm tree)}[m_i] \to \mathcal{L}^{(\rm tree)}_{\rm int}\left[m_i\left(1+\frac{\varphi}{F_\varphi}\right)\right] \tag{2.52}$$

where we the decay constant F_φ was defined in equation 2.35. This produces Yukawa-like interactions of φ with the fermions, as well as trilinear and quartic couplings with the Higgs and the gauge bosons. This form of the radion potential is dictated by the AdS isometries (and hence is valid in the limit of $\epsilon \ll 1$). The self-interaction terms for the radion are generated by the GW mechanism,

$$\mathcal{L}_{\rm radion} = \frac{1}{2} m_\varphi^2 \varphi^2 \left(1 + \frac{5}{3}\frac{\varphi}{F_\varphi} + \frac{11}{12}\frac{\varphi^2}{F_\varphi^2}\right) \tag{2.53}$$

where we have only kept terms to leading order in ϵ. Finally, the scalars s interact with the SM through the radion portal.

$$\mathcal{L}^{(\rm tree)}_{\rm s} = \lambda_s v_s^2 \mu_{\rm TeV}^2 s^2 \left(1+\frac{\varphi}{F_\varphi}\right)^2 + \lambda_s v_s \mu_{\rm TeV} s^3 \left(1+\frac{\varphi}{F_\varphi}\right) + \frac{1}{4}\lambda_s s^4 + \mathcal{O}(\gamma) \tag{2.54}$$

The terms suppressed by the explicit Z_2 violating coupling γ are assumed to be very small, and do not contribute significantly to the zero-temperature phenomenology. Notice that

we do not generate terms of the form of φ-s mixing, or $s\varphi^3$. The classical solution sets the linear term in s to zero, and the φ field coupling as $(1+\varphi)$ then does not have a linear coupling to s around the vacuum. A small Higgs portal coupling of the form $\kappa s H^\dagger H$ can be added in order for s to be able to decay safely before BBN.

At loop level, there are also induced couplings between the EM and QCD field strengths proportional to their β-functions:

$$\mathcal{L}_{\rm int}^{(1-{\rm loop})} \supset \frac{\alpha_{\rm EM}}{8\pi F_\varphi} b_{\rm EM} \varphi \, F_{\alpha\beta} F^{\alpha\beta} + \frac{\alpha_s}{8\pi F_\varphi} b_{\rm G} \varphi \, G^a_{\alpha\beta} G^{a\,\alpha\beta} \,, \tag{2.55}$$

with the dominant contributions to these terms coming from quark and W-boson loops. In the case where the SM is confined to the IR brane, $b_{\rm EM} = 11/3$, $b_{\rm G} = -\frac{11}{3} N_c + 2n/3$, where n is the number of quarks lighter than the radion [191].

2.3.2 Experimental constraints

The low energy phenomenology of the model is largely determined by the physical masses of the radion and s fields, as well as the KK scale. These are related to the fundamental parameters of the model by:

$$m_{\rm KK} \simeq \frac{5\pi}{4} \mu_{\rm TeV} \,, \tag{2.56}$$

$$m_\varphi = 2\sqrt{2} v \epsilon^{3/4} \mu_{\rm TeV} \,, \tag{2.57}$$

$$m_s = \sqrt{2\lambda_s} v_s \mu_{\rm TeV} \,. \tag{2.58}$$

Collider searches limit the KK scale in RS models to be above $m_{\rm KK} \gtrsim 4.25$ TeV [192, 193], requiring the KK resonances to be out of the kinematic reach of current colliders. Due to the approximate shift symmetry of the GW field (broken only by the small parameter ϵ), the radion is parametrically lighter than the KK scale. The AD scalar masses are similarly suppressed, with m_s proportional to the combination $(\lambda_s v_s^2)^{1/2}$, which is chosen to be small for the s phase transition to happen well before the deconfinement transition. Therefore, the radion and the AD scalars can be kinematically accessible at colliders [194], however their couplings to the SM are suppressed by $\mu_{\rm TeV}$. Collider constraints translate into a bound $\mu_{\rm TeV} \gtrsim 2\,{\rm TeV}$ [191], which is weaker than direct bounds on the KK scale.

If the radion mass is below the GeV scale, bounds on the $\varphi\gamma\gamma$ coupling from supernova cooling[4], cosmology and beam dump experiments can give the strongest bounds on the model. These limits have been derived for axion-like particles [196–198], which translate into a bound

$$F_\varphi \gtrsim 4.25 \times 10^7 \,\mathrm{TeV}\,. \tag{2.59}$$

For a heavier radion $m_\varphi > 1\mathrm{GeV}$, these constraints are no longer applicable. The radion mass will be above a GeV for parameters,

$$v\epsilon^{3/4} > 7 \times 10^{-5} \ \left(\frac{\mu_{\mathrm{TeV}}}{5\ \mathrm{TeV}}\right)^{-1}\,. \tag{2.60}$$

The AD scalars can couple to the SM fields through the radion portal. For light AD scalars, the couplings to photons/gluons generated at higher loop order might still provide significant constraints. If the AD scalars are above the 1 GeV scale, these constraints are also absent.

2.4 Cosmology

The mechanism of avoided deconfinement has dramatic implications for early universe cosmology. The main departure from a standard cosmology is due to the scaling of the radion expectation value with temperature. This leads to the interesting consequence that while the universe may be reheated to a very high temperature (exciting heavy fields on the UV brane, for instance), from the IR brane point-of-view, the cosmology resembles a low-reheat cosmology. We aim to highlight some of the applications of the AD model to cosmology, but leave a detailed study of these implications for future work.

Figure 2.2 shows the characteristic dependence on temperature of dimensionful parameters on the IR brane. In particular, $m_{KK} > T$ to arbitrarily high temperature, as required by the condition that the IR brane be stabilised outside the horizon at a given temperature. Therefore, KK modes play no role in early universe cosmology from the point of view of the IR brane. In the high temperature regime $T > T_c$, the radion expectation value scales with temperature as:

$$\mu(T) \propto T^{\frac{1}{1+\epsilon}}\,. \tag{2.61}$$

[4]Whether supernova bounds on the radion coupling apply depends on the radion coupling to nucleons [195]. In the case where the SM quarks and gluons are on the IR brane, this coupling is too large for the radion to contribute significantly to supernova cooling.

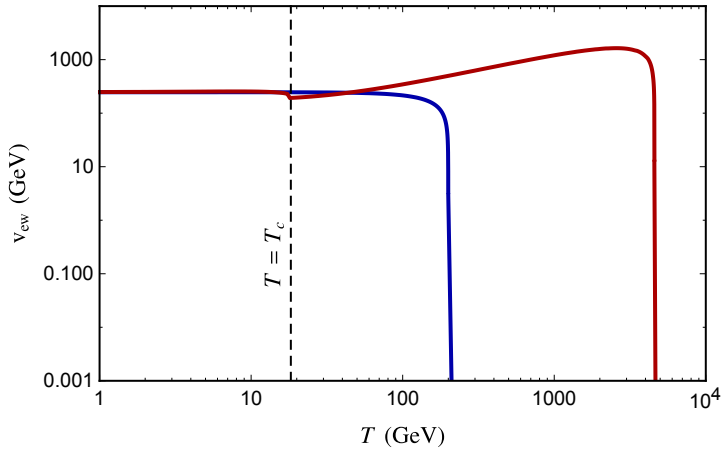

Figure 2.3: Higgs expectation value, $v_{\rm ew}$, as a function of temperature for the parameters of equation (2.48) (blue) and equation (2.63) (red). The dashed line is the critical temperature, $T_c = 18$GeV for the choice of parameters in equation (2.63).

This introduces a scaling of the other dimensionful quantities of the theory with T. The KK scale, the Higgs mass parameter and the QCD scale and are all proportional to $\mu(T)$[5], which means that the ratio of the temperature to these mass scales (denoted Λ) varies with T as:

$$\frac{T}{\Lambda} \propto T^{\frac{\epsilon}{1+\epsilon}} \,. \tag{2.62}$$

The consequence of this scaling is that the ratio T/Λ may reach unity at significantly higher temperatures than is the case in standard RS cosmology. For example, as we show below, if the critical temperature T_c is below the electroweak symmetry breaking scale, then the electroweak symmetry restoration phase transition may occur at much higher temperatures than in the usual case, or never occur at all.

2.4.1 Electroweak Phase Transition

In this section we show that the electroweak phase transition can occur in the avoided deconfinement phase at temperatures much higher than the weak scale. To illustrate some of these effects, we use a new set of parameters, with:

$$v_{\rm ir} = 1.5 \times 10^{-4},\ v_{\rm uv} = 7.5 \times 10^{-4},\ \epsilon = 0.05 \tag{2.63}$$

and all other parameters as in equation (2.48), which leads to a radion stabilised at $\mu_{\rm TeV} = 4.73$ TeV at zero temperature. We note that with these parameters, the model

[5]More generally, $\Lambda_{\rm QCD} \propto (\mu(T))^n$, where $n = 1$ is true for the case where the SM is confined to the IR brane, $n < 1$ if some of the SM quark fields are bulk fields.

in its simplest form does not satisfy the bound on the radion mass (2.60). We expect that a more complete model with additional breaking of scaling invariance can lead to an unsuppressed radion mass and a less severe bound than equation (2.60). This could happen, for example, through additional terms in the GW action [183], allowing more fields to propagate in the bulk, or by considering a more general geometry for the fifth dimension [152]. We will leave the detailed model building for future work.

The Higgs potential at finite temperature gets thermal corrections from the top Yukawa, gauge couplings and its quartic coupling. In addition, the Higgs mass parameter scales with $\mu(T)$. The Higgs thermal mass in the low- and high-temperature limits is given by:

$$\mu_h^2(T > T_c) = T^2 \left(-\lambda \frac{v_{\rm ew}^2}{c^2 T_c^2} \left(\frac{cT_c}{T} \right)^{2\epsilon} + \frac{\lambda_t^2}{4} + \frac{3g^2}{16} + \frac{g'^2}{16} + \frac{\lambda}{2} \right), \tag{2.64}$$

$$\mu_h^2(T < T_c) = -\lambda v_{\rm ew}^2 + T^2 \left(\frac{\lambda_t^2}{4} + \frac{3g^2}{16} + \frac{g'^2}{16} + \frac{\lambda}{2} \right). \tag{2.65}$$

where $v_{\rm ew} \simeq 246$GeV. The electroweak phase transition (EWPT) happens at the temperature where the Higgs mass parameter become positive. This happens for $T < T_c$ if T_c is above the electroweak scale, in which case there is no modification to the phase transition in comparison to the SM. However, if T_c is below the electroweak scale, the EWPT will occur at a temperature:

$$T_* = cT_c \left(\frac{T_{\rm ew}}{cT_c} \right)^{\frac{1}{\epsilon}} \tag{2.66}$$

where $T_{\rm ew}$ is the temperature of the EWPT in the SM. For small ϵ, even a modest ratio $T_{\rm ew}/T_c$ can lead to the EWPT occurring at a temperature which is orders of magnitude above the scale predicted by the SM. Figure 2.3 shows $-\mu_h^2$ as a function of temperature the two sets of parameters defined in equations (2.48) & (2.63). For the second set of parameters the EWPT doesn't occur until the universe reaches a temperature of order $\sim 5 \times 10^3$ GeV.

A high temperature EWPT has been considered in refs [153–156] in the context of electroweak baryogenesis. A primary motivation for these models is to avoid the bounds which result from introducing new sources of CP violation around the weak scale by having the EWPT occur at a temperature $T \gg v_{\rm ew}$. This typically requires the introduction of a large number of fields coupled to the Higgs sector in order to significantly increase the temperature of the phase transition while satisfying collider bounds. In contrast, the

AD model provides a mechanism in which the electroweak phase transition can occur at arbitrarily high temperatures due solely to the Higgs-radion interaction. However, the Higgs potential must still be modified to make the EWPT first order and introduce new sources of CP violation introduced in order to include a mechanism for electroweak baryogenesis in the AD framework. Further, even though the electroweak phase transition happens at much higher temperatures, the scales governing local physics on the IR brane also scale with T. Thus, if the CP violating operators are localized on the IR brane, their effect at $T = T_*$ will be the same as that at $T = T_c \lesssim v_{\rm ew}$. Therefore, they will be subject to the very constraints the models of [153–156] were constructed to avoid. On the other hand, if the CP violating operators are on the UV brane/bulk, their effect does become much more important at higher temperatures.

2.4.2 High Scale Baryogenesis

As discussed in section 2.1, in the usual RS model the high temperature phase is described by an AdS black hole, before a phase transition to the RS phase at a temperature around the TeV scale or below. The period of supercooling accompanying the phase transition significantly dilutes any pre-existing baryon asymmetry [146]. This has motivated consideration of baryogenesis mechanisms that combine the electroweak and RS phase transitions [139, 142, 143]. Baryogenesis mechanisms which operate at temperatures significantly above the TeV scale are difficult to realise in the RS model. This is not the case, however, for the AD model, as the universe is never in the BH phase after inflation and does not undergo a period of supercooling.

At high temperature the radion is stabilised closer to the UV brane. This means that fields localised toward the IR brane may have significant overlap with UV- localised fields at early times, with the UV and IR sectors then decoupling at low temperature. This allows for the possibility of having baryogenesis occur due to interactions between the IR and UV fields, which have $\mathcal{O}(1)$ couplings in the early universe but whose interactions are negligibly small after the radion has settled to its zero-temperature expectation value.

2.4.3 QCD Phase Transition and the QCD Axion

The QCD phase transition in the AD model may also be modified from the usual picture if T_c is below the QCD scale. In order to achieve this in our model while satisfying the bounds on the radion and s masses requires a large number of AD scalars. However, as was the case for the electroweak phase transition, even for T_c slightly below the QCD scale the QCD phase transition may occur at temperatures far above the TeV scale. This may be able to reproduce some of the non-standard QCD dynamics discussed in refs [199–201].

A cosmology where QCD confinement occurs at high temperatures, when $\Lambda_{\rm QCD}(T) \gg \Lambda_{\rm QCD}(0)$, can also have dramatic consequences for the abundance of the QCD axion. The axion field can have various 5D origins; one simple possibility is that it is the fifth component of $U(1)$ gauge field in 5D. Irrespective of its origin, the large decay constant of the axion suggests that its wavefunction is localised near the UV brane. Therefore, we can safely assume that f_a is largely temperature independent. In the confined phase of QCD, but with a temperature-dependent confinement scale, the axion mass is given by,

$$m_a(T) = \frac{f_\pi(T) m_\pi(T)}{f_a} \tag{2.67}$$

The axion starts oscillating around the epoch of QCD confinement at a temperature $T_{\rm osc}$ which is defined by $m_a(T_{\rm osc}) \simeq H(T_{\rm osc})$. The axion abundance at the onset of oscillation is

$$\rho_a(T_{\rm osc}) \sim m_a^2(T_{\rm osc}) f_a^2 \theta_i^2 \tag{2.68}$$

where θ_i is the initial misalignment angle. The mass of the axion continues to decrease due to the temperature dependence of $\Lambda_{\rm QCD}(T) \sim \mu(T)$. In the adiabatic approximation $\dot{m} \ll m^2$, the number density of the axion scales as a^{-3}, and the mass redshifts as $\sim a^{-2}$, so the axion energy density redshifts approximately as a^{-5} in this epoch, whereas the background energy density is redshifting as a^{-4}. This can reduce the axion abundance dramatically.

2.4.4 Gravitational Waves

The absence of a first order confinement phase transition is a necessary feature of this mechanism that distinguishes it from the standard RS model. The RS phase transition results in a gravitational wave signal which will be absent in the avoided deconfinement

model [136, 144]. The RS phase transition also leads to a drop in g_* of order N^2 as a result of degrees of freedom confining and freezing out. If there is an observable background of gravitational waves, such as from a cosmic string network [202, 203] or inflation [204–206], this change in g_* is observable as a relative decrease in the power in modes which were below the horizon scale prior to the phase transition. The absence of these gravitational wave signals could be used to distinguish the AD model from RS models which do undergo a phase transition. Furthermore, the addition of the AD scalars, which are necessarily light degrees of freedom due to the bound (2.51), also leads to a potentially observable change in g_* in the early universe for N_s as low as $N_s \sim 10$ and masses around the GeV scale.

In addition to modifying the RS phase transition, in our set up there are additional phase transitions associated with the s fields, which can be first order and can each happen at slightly different temperatures. This can give us interesting forest of GW signals with a spectrum that is different from the one expected from a single phase transition. As noted above, the electroweak and/or the QCD phase transition may also be made first order and can happen at very high temperatures, predicting a gravitational wave signature from these phase transitions as well.

2.5 Non-thermal Dark Matter production

The AD mechanism can also lead to a novel production mechanism for dark matter (DM). If dark matter is a field χ localised to the IR brane, then $m_\chi \propto \mu(T)$, and the scaling of the DM mass with temperature can lead to the DM being non-relativistic up to very high temperatures. The production of χ from the thermal bath is then suppressed by a Boltzmann factor, significantly altering the usual calculation for χ production. In particular, this can lead to DM produced via a freeze-in process [207] while still having $\mathcal{O}(1)$ couplings to the SM.

The usual freeze-in mechanism [207] applies to particles χ which have a negligible initial abundance and a highly suppressed coupling λ to thermalised species [207–212]. The suppressed interactions mean that the χ abundance is always out of equilibrium value and freezes-in at a temperature such that $x = m_\chi/T \sim 2 - 5$. Below this temperature the production and annihilation rates for χ particles are exponentially suppressed and the co-moving number density remains constant.

The DM abundance produced by freeze-in increases with λ and typically values of $\lambda \sim 10^{-10}$ are required to produce the observed DM abundance. A coupling of this order also means that these models are often difficult to detect. However, if the DM candidate χ has a mass (m_χ) larger than the reheat temperature (T_r) then the freeze-in mechanism can produce the correct relic abundance for $\mathcal{O}(1)$ couplings between χ and the thermal plasma. This works as the χ production process is suppressed by the Boltzmann factor $e^{-m_\chi/T}$, so the effective coupling which governs the freeze-in process is not λ but λe^{-x_r}, where $x_r = m_\chi/T_r \gtrsim 1$. The requirement for the correct relic abundance then becomes $\lambda e^{-x_r} \sim 10^{-10}$, which can be easily achieved for $\lambda \sim 1$ and $x_r \sim 25$.

2.5.1 Boltzmann Equations

In this section we review the production of non-relativistic DM assuming a standard cosmology, before discussing how the AD model modifies the picture in the following sections. The mechanism considered is similar to non-thermal DM production [166, 167], which has some similarity to the freeze-in mechanism as the DM never reaches thermal equilibrium, but can be achieved with $\mathcal{O}(1)$ couplings.

To illustrate this we consider a model where the dominant process contributing to the χ abundance is

$$\chi\chi \leftrightarrow \phi\phi\,, \tag{2.69}$$

for a thermalised species ϕ which is taken to be massless. We will parametrise the matrix element for this process as $\mathcal{M} = \lambda$ for some effective coupling λ. If the process (2.69) is governed by a renormalisable operator, then λ is simply the coupling in the Lagrangian. If either χ, ϕ or both are fermions the process comes from a higher-dimensional operator, as in models with a heavy mediator [213, 214]. In that case, the effective coupling is related to the tree-level coupling by;

$$\lambda = \lambda_{\text{tree}} \left(\frac{m_\chi}{M_{\text{uv}}}\right)^{d-4}\,, \tag{2.70}$$

where d is the dimension of the operator and $M_{\text{uv}} > m_\chi$ a UV scale which is integrated out.

The number density of χ particles in the early universe is governed by the Boltzmann equation:

$$\dot{n}_\chi + 3Hn_\chi = \langle\sigma v\rangle \left(n_{\rm eq}^2 - n_\chi^2\right) , \tag{2.71}$$

where $n_{\rm eq}$ is the equilibrium number density. The thermally-averaged cross-section is given by the integral [215, 216]

$$n_{\rm eq}^2 \langle\sigma v\rangle = \frac{g_\chi^2 T}{512\pi^5} \int_{4m_\chi^2}^\infty ds\, |\mathcal{M}|^2\, K_1\left(\frac{\sqrt{s}}{T}\right) \sqrt{s - 4m_\chi^2} \tag{2.72}$$

where K_1 is a modified Bessel function and g_χ is the number of degrees of freedom of the field χ. Extracting the parametric dependence for large x, we find

$$n_{\rm eq}^2 \langle\sigma v\rangle \simeq \frac{g_\chi^2 T^4}{256\pi^4} \lambda^2 x e^{-2x} . \tag{2.73}$$

Using this result and re-writing equation (2.71) in terms of the yield $Y_\chi = n_\chi/s$ we find

$$\frac{dY_\chi}{dx} = \frac{45 M_P \lambda^2 x e^{-2x} g_\chi^2}{1.66 \times 512\pi^6 g_{*S}\sqrt{g_*} m_\chi} \left(1 - \frac{Y_\chi^2}{Y_{\rm eq}^2}\right) , \tag{2.74}$$

We can then integrate from $x = x_r$ to $x \to \infty$ to get:

$$Y_\chi(T \to 0) = \frac{45\lambda^2 g_\chi^2 M_P}{1.66 \times 2048\pi^6 g_{*S}\sqrt{g_*} m_\chi} \left(1 + 2x_r\right) e^{-2x_r} , \tag{2.75}$$

leading to a present-day abundance of:

$$\Omega_\chi h^2 = 0.103 \times g_\chi^2 \left(\frac{\lambda e^{-x_r}}{10^{-10}}\right)^2 \left(1 + 2x_r\right) . \tag{2.76}$$

Here we note that this depends on the mass only through the parameter $x_r = m_\chi/T_r$. This mechanism therefore offers a mechanism for DM production over a wide mass range, although requires a specific ratio of the mass to reheat temperature. For DM in the meso-tuned range with $\mathcal{O}(1)$ couplings this points to a reheat temperature in the range 40 GeV to 4 TeV. A reheat temperature in this range makes a baryogenesis mechanism difficult to accommodate, although production of a baryon asymmetry in models with a low reheat temperature are possible [217].

Here we also note the possibility of a period of matter domination just after inflation, as may be the case in models with a reheat temperature at the TeV scale or below [167, 169].

In this case the decay of a scalar field reheats the universe after inflation. If the decay is rapid, then the reheat temperature is given in terms of the inflationary hubble scale H_I as

$$T_r = \sqrt{M_P H_I}\,. \tag{2.77}$$

In this case the above analysis holds although this requires a very low hubble scale during inflation.

If instead the scalar field decays slowly then H_I can be larger than the hubble rate at T_r. The temperature in this case increases to a maximum of $T_{\rm max}$ before cooling with the scale factor a as $T \propto a^{-3/8}$ until reaching T_r at the start of the radiation dominated era. For large $x_{\rm max} = m_\chi/T_{\rm max}$ the DM abundance in this case is given by replacing [171, 174]:

$$e^{-2x_r} \to \left(\frac{T_r}{T_{\rm max}}\right)^8 e^{-2x_{\rm max}}\,, \tag{2.78}$$

in equation (2.76), up to an $\mathcal{O}(1)$ prefactor. This leads to a suppressed present day density compared to the case considered in this work. There is also the possibility that the χ abundance is produced through the decay of the inflaton [166–170, 172] or moduli [173]. In both cases an additional dependence on the details of inflation is introduced through the parameter $T_{\rm max}$, and as such we do not consider these cases here, instead assuming instantaneous reheating after inflation.

As discussed in the following section, the AD model provides a scenario where DM is produced in the same way without having to assume a low reheat temperature, a scenario where the approximation of instantaneous decay is more consistent with models of inflation.

2.6 Dark matter and Avoided Deconfinement

The temperature dependence of the radion vev leads to all dimensionful parameters on the IR brane scaling with temperature in a similar way. In particular, the mass of an IR degree of freedom will have a temperature dependence of:

$$m_{\rm ir}(T) = m_{\rm ir}(0)\frac{\mu(T)}{\mu(0)} = m_{\rm ir}(0)\left(\frac{T}{T_c}\right)^{\frac{1}{1+\epsilon}}\,. \tag{2.79}$$

This implies that the ratio $x(T) = m_{\rm ir}(T)/T$ changes by a factor:

$$\frac{x(T_r)}{x(T_c)} = \left(\frac{T_c}{T_r}\right)^{\frac{\epsilon}{1+\epsilon}}\,, \tag{2.80}$$

during the period of avoided deconfinement. Taking the benchmark parameters of [218], $T_r \sim 10^{11}\,\text{GeV}$, $T_c = 16.6\,\text{TeV}$, $\epsilon = 4.13 \times 10^{-2}$ gives:

$$\frac{x(T_r)}{x(T_c)} = .53\,. \tag{2.81}$$

This allows for the non-thermal production of dark matter with a mass around the TeV scale while requiring only mild assumptions about the reheat temperature[6]. Any particle with mass set by the radion vev which satisfies $m \gtrsim 2T_c$ will remain non-relativistic throughout the entire thermal history due to the temperature dependence of the radion.

In comparison to typical non-thermal dark matter production, the yield in the AD model is enhanced due to the longer time the ratio x remains constant. This is captured by the relation:

$$\frac{dx}{dT} = -\frac{\epsilon x}{T}\,, \tag{2.82}$$

as opposed to $dx/dT = -x/T$ in the usual case. This leads to a $1/\epsilon$ enhancement of the final abundance:

$$\Omega_\chi h^2 = 0.1 \times \left(\frac{4.13 \times 10^{-2}}{\epsilon}\right)\left(\frac{\lambda e^{-x_r}}{10^{-11}}\right)^2 (1 + 2x_r) \tag{2.83}$$

giving the correct present-day abundance for slightly larger values of x_r given fixed coupling λ.

2.6.1 Radion portal dark matter

Any DM candidate in the AD model necessarily couples through the radion portal, so a minimal model is presented here where the radion couplings set the DM abundance [191, 219, 220]. Below the electroweak scale and in unitary gauge, the interaction Lagrangian governing the radion interactions with the SM is:

$$\begin{aligned}\mathcal{L}_{\varphi,\text{int}} =& \frac{\varphi}{2F_\varphi}(\partial h)^2 - \sum_\psi \left(\frac{\varphi}{F_\varphi}\right) m_\psi \bar{\psi}\psi - \frac{5m_\varphi^2}{3F_\varphi}\varphi^3 - \frac{11}{24}\frac{m_\varphi^2}{F_\varphi^2}\varphi^4 \\ &+ \left(\frac{2\varphi}{F_\varphi} + \frac{\varphi^2}{F_\varphi^2}\right)\left(m_W^2 W_\mu^+ W^{-\,\mu} + \frac{m_Z^2}{2} Z_\mu Z^\mu - \frac{m_h^2}{2} h^2\right)\,.\end{aligned} \tag{2.84}$$

[6]The maximum allowed reheat temperature in the AD model is bounded by the requirement that the RS phase remains metastable, for the benchmark points presented here this requires $T_R \lesssim 5 \times 10^{11}\,\text{GeV}$.

For the case of scalar χ, the couplings to the radion are described by the Lagrangian

$$\mathcal{L}_{\varphi,\chi} = -\frac{m_\chi^2}{2}\left(1+\frac{\varphi}{F_\varphi}\right)^2\chi^2\,. \tag{2.85}$$

In the limit where χ is heavier than the SM fields and the radion, the dominant processes which contribute to freeze-out are the χ annihilations to the higgs, radion and longitudinal modes of the electroweak gauge bosons. In this limit the squared matrix elements for these processes are all equal and given by:

$$|\mathcal{M}|^2 = 4\left(\frac{m_\chi}{F_\varphi}\right)^4\,, \tag{2.86}$$

The DM abundance is therefore governed by the cross-section

$$\sigma v = \frac{\lambda_{\text{eff}}^2}{32\pi m_\chi^2} \tag{2.87}$$

where we have defined the effective coupling:

$$\lambda_{\text{eff}} = 2\sqrt{5}\left(\frac{m_\chi}{F_\varphi}\right)^2\,, \tag{2.88}$$

which can be substituted for λ in equation (2.83) to determine the relic abundance.

The avoided deconfinement model solves two issues with the non-thermal production process for DM in the meso-tuned range. The RS model solves the hierarchy problem as the radion sets the scale of physics on the IR brane to be of order $10-100$ TeV, predicting the existence of new particles with masses $m \sim c\mu(0)$ for $c \sim \mathcal{O}(1)$. Given $T_c < \mu(0)$, any new particle with $c \gtrsim 2$ will remain non-relativistic for the thermal history of the universe, and stable particles can have a relic abundance set by a similar process to the one described here without having to assume a relationship between T_r and m_χ. Furthermore, the assumption of instantaneous reheating is more natural in the AD model as the reheat temperature can be large without χ becoming relativistic, meaning no assumptions about the hubble scale of inflation are necessary.

2.7 Experimental Signatures

In this section, the possible experimental signatures of meso-tuned WIMPs are discussed. The experiments sensitive to the model depend on the final state of χ annihilations

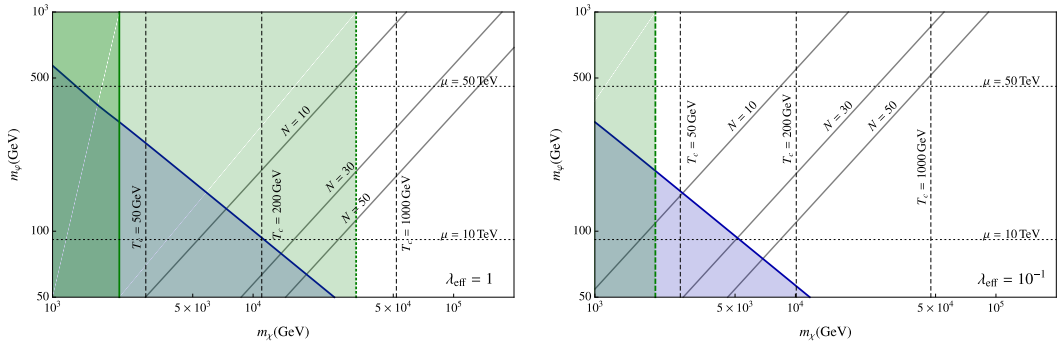

Figure 2.4: Bounds on the parameter space for fixed $\lambda_{\rm eff} = 1$ (left) and $\lambda_{\rm eff} = .1$ (right). Blue shaded regions are excluded by direct detection null results. The light green regions show the bounds from CTA assuming the maximum possible Sommerfeld enhancement, $S \sim 200$, while the dark green region shows the CTA bounds when Sommerfeld enhancement is negligible. The ratio x_r required to generate the correct relic abundance is $x_r = 27$ for $\lambda_{\rm eff} = 1$ and $x_r = 25$ for $\lambda_{\rm eff} = .1$.

which set the relic abundance. If χ couples to nuclei the strongest bounds come from direct detection, while if the production process comes from χ annihilations to τ or W final states then CTA and H.E.S.S. are sensitive to the gamma ray signal form χ annihilations in the galactic centre.

Experiments sensitive to the γ ray emission from the galactic centre are most sensitive to χ annihilations to τ or W final states. In the mass range $m_\chi \sim 10 - 100\,\text{TeV}$, the projected bounds from CTA are of order [221–224]

$$\sigma v \lesssim 10^{-26} - 10^{-25}\ \text{cm}^3\text{s}^{-1}\,. \tag{2.89}$$

H.E.S.S. has a similar sensitivity in the range $m_\chi \sim 1 - 10\,\text{TeV}$ but the sensitivity falls off more rapidly at higher masses [225]. HAWC is also sensitive to gamma-ray emission but the bounds are above the cross-sections predicted by the model considered in this work [226, 227]. Indirect detection experiments are also sensitive to χ decays to a $b\bar{b}$ final state, but in this case direct detection offers the strongest constraints on the model. Compared to the $\chi\chi \to b\bar{b}$ cross-section, the cross-section for χ scattering with nuclei is further suppressed by a form factor of $f_b^2 \sim 10^{-4}$, however PandaX2 [228, 229] and Xenon1T [230, 231] place strong bounds on the cross-section to nuclei:

$$\sigma_{\chi N} \lesssim 3 \times 10^{-36}\ \text{cm}^3\text{s}^{-1} \left(\frac{m_\chi}{\text{TeV}}\right)\,, \tag{2.90}$$

offering stronger constraints than indirect detection experiments.

2.7.1 Constraints on radion portal DM

For the case of the scalar model which couples via the radion portal presented in section 2.6.1 the dominant bounds come from CTA and direct detection experiments. The relevant cross-sections are the annihilation to W-bosons

$$\sigma v\left(\chi\chi \to WW\right) = \frac{\lambda_{\text{eff}}^2}{80\pi m_\chi^2} \tag{2.91}$$

and scattering off nuclei [191]:

$$\begin{gathered}\sigma\left(\chi N \to \chi N\right) \simeq \frac{F_N^2 \lambda_{\text{eff}}^2}{20\pi} \frac{m_N^2}{m_\chi^2 m_\varphi^4}\,, \\ F_N \sim 0.6\text{GeV}\,.\end{gathered} \tag{2.92}$$

Which is derived from the interaction terms coupling the radion to quarks:

$$\mathcal{L} \supset -\sum_q \frac{m_q}{F_\varphi}\,\varphi\bar{q}q\,. \tag{2.93}$$

The bounds on the model are shown in figure 2.4 for fixed effective couplings $\lambda_{\text{eff}} = 1$ and $\lambda_{\text{eff}} = .1$ respectively. Direct detection constraints (blue shaded region) rule out the region of parameter space where both the radion and χ are light. At larger masses direct detection experiments lose sensitivity due to the $m_\chi^{-2} m_\varphi^{-4}$ dependence of the cross section. Lines of constant N are shown in gray, defined implicitly as a function of m_χ from the requirement of constant λ_{eff}. Similarly, the dotted horizontal lines show the values of the radion vev μ given the radion mass, and the vertical dashed lines show the critical temperature T_c of the AD model required to generate the correct relic abundance. In both figures the reheat temperature T_r is fixed to be 10^{10} GeV and ϵ set to 4.13×10^{-2}. For small ϵ the model is largely insensitive to T_r – increasing T_r to the Planck scale results only in a shift of the value of T_c required to produce the observed DM abundance by a factor of 2.

For $\lambda_{\text{eff}} \sim \mathcal{O}(1)$ CTA is sensitive to χ masses up to the multi-TeV range (green shaded regions), assuming the maximum sensitivity $(\sigma v)_{\chi W} < 10^{-26}$ cm^{3}s^{-1} across the mass range. The dark green region in figure 2.4 shows the CTA reach without considering possible Sommerfeld enhancement of the cross-section [232], while the light green regions in figure 2.4 show the CTA sensitivity assuming the maximum possible Sommerfeld enhancement[7].

[7] By maximum possible enhancement we mean the largest enhancement factor for the given coupling in the mass range displayed on the figures.

For $\lambda_{\text{eff}} \lesssim 10^{-1}$ CTA begins to lose sensitivity to the model even in the presence of a significant enhancement of the cross-section.

The enhancement factor is derived by resumming ladder diagrams involving dilaton exchange between χ legs, and can be approximated as [233–235]

$$S \simeq \frac{\pi}{\epsilon_v} \frac{\sinh\left(\frac{12\epsilon_v}{\pi\epsilon_\phi}\right)}{\cosh\left(\frac{12\epsilon_v}{\pi\epsilon_\phi}\right) - \cos\left(2\pi\sqrt{\frac{6}{\pi^2\epsilon_\phi} - \left(\frac{12\epsilon_v}{\pi\epsilon_\phi}\right)^2}\right)}, \tag{2.94}$$

where $\epsilon_v = \frac{2\pi v F_\varphi^2}{m_\chi^2}$, $\epsilon_\phi = \frac{2\pi m_\varphi F_\varphi^2}{m_\chi^3}$ and $v \sim 10^{-3}$ is the DM velocity. This factor is only significant at resonances in tuned regions of parameter space, but for $\lambda_{\text{eff}} = 1$ can be as high as $S \sim 200$ for the masses plotted in figure 2.4. In these resonance regions the lower bound on m_χ can be increased by over an order of magnitude, as shown by the dotted green line in figure 2.4 which shows the bound assuming the strongest possible Sommerfeld enhancement. The effect is reduced for smaller λ_{eff}, but for $\lambda_{\text{eff}} = .1$ the maximum enhancement is still $S \sim 86$. In regions where this enhancement is realised indirect detection experiments are still sensitive to the model even at couplings $\lambda_{\text{eff}} \lesssim 0.1$.

Chapter 3

Vacuum Decay Catalysed by Magnetic Monopoles

First order phase transitions which occur in nature are often strongly catalysed by boundary effects or defects which exponentially enhance the rate of transition. Some examples of this are the boiling phase transition of water and bubble formation in cloud chambers. It is therefore natural to ask whether cosmological phase transitions may be catalysed by defects in the same way. In this chapter it is shown that magnetic monopoles may act as impurities which seed phase transitions in the early universe. We study models of vacuum decay catalysed by the 't Hooft–Polyakov monopole [124, 125], with a scalar field potential such that the symmetry breaking vacuum is metastable and the symmetry preserving vacuum is a global minimum. In this case the monopole is metastable for a range of parameters and can tunnel to an expanding true vacuum bubble. Classically unstable monopoles were studied in [236, 237] and metastable monopoles were studied in the thin-wall approximation in [238, 239].

This idea can be generalised to other topological defects such as global monopoles, strings [240–242] and domain walls. The defect need not be topologically stable [243, 244] and there exist studies of Q-balls [245–247] and black holes as nucleation sites [248–254] which can affect the electroweak lifetime [255–259]. The gravitational effect of compact objects was considered in [260] and finite density effects in [261]. In each of these studies the catalysed decay is analysed using a thin-wall approximation or in the limit of classically unstable defects, although this is far from the most general scenario.

The usual homogeneous false vacuum decay proceeds through bubble nucleation. The rate of transitions is calculated through semiclassical field configurations which are solutions to euclidean field equations, as was described in section 1.4.2 [74–76], also known as bounce solutions. The bounce action is usually calculated in the limit of zero or infinite temperature, where the field profiles have an $O(3)$ or $O(4)$ symmetric dependence on the coordinates. The saddle point describing monopole decay does not have $O(3)$ or $O(4)$ symmetry in euclidean space, and is difficult to find away from the thin-wall limit studied in [238, 239]. In section 3.2 a new method to determine the solutions to catalysed tunnelling problems is presented, using the mountain pass theorem (MPT) to numerically find the saddle point. This provides the first steps towards reliable calculations of the lifetime of metastable vacua when defects are present.

There are many applications of this calculation, which depend on the mechanism by which monopoles are populated. They could arise from a Kibble-Zurek mechanism from an earlier phase transition (see section 1.5.3), be produced in high energy collisions or black hole evaporation. The production can leave an imprint on the gravitational wave background both through the rate of the phase transition, which determines the amplitude and peak frequency of the signal, and through the spatial distribution of magnetic monopoles which can lead to an observable angular anisotropy in the signal.

False vacuum decay and the physics of metastable monopoles in the thin-wall limit is reviewed in section 3.1. The method to evaluate the bounce action is presented in section 3.2, and some applications of our results are shown in section 3.3.

3.1 Monopoles & Vacuum Decay

In this section we review the formalism for calculating the lifetime of a homogeneous false vacuum state and compare this to vacuum decay seeded by magnetic monopoles in the thin wall limit. The magnetic charge of the monopole may correspond to the SM $U(1)_{\rm em}$ or to a hidden sector. For concreteness we consider a model with an $SU(2)$ gauge symmetry, and a scalar field ϕ which is charged in the triplet representation. It is possible that the monopoles come from the breaking of a larger gauge group, in which case $SU(2)$ represents

a subgroup of the full gauge symmetry. The scalar potential we consider is

$$V_\phi(\phi^\dagger\phi) = \lambda v^4 \left(\frac{1}{2}\frac{(\phi^\dagger\phi)}{v^2} - \left(1 - \frac{3\epsilon}{\lambda}\right)\frac{(\phi^\dagger\phi)^2}{v^4} + \frac{1}{2}\left(1 - \frac{4\epsilon}{\lambda}\right)\frac{(\phi^\dagger\phi)^3}{v^6} \right), \tag{3.1}$$

where λ, ϵ are dimensionless parameters. The shape of the potential is shown in figure 3.1. This form of the potential is chosen so that for $0 < \epsilon < \lambda/6$, $\phi = 0$ is the true minimum of the potential, and there is a second set of (metastable) minima at $|\phi| = v$ separated from the true vacuum by a potential barrier. ϵ parametrises the difference in potential energy between the vacua:

$$V_\phi(v) - V_\phi(0) = \epsilon v^4, \tag{3.2}$$

and λ sets the overall size of the potential.

The gauge sector is not relevant for the homogeneous false vacuum tunnelling process, and we choose this specific set up anticipating the discussion of magnetic monopoles catalysing the phase transition in section 3.1.2. Since ϕ is charged under $SU(2)$, terms in the potential must be powers of the gauge invariant combination $\phi^\dagger\phi$, so in order to satisfy both these conditions the potential must be stabilised by an operator with dimension > 4. We are assuming that the $(\phi^\dagger\phi)^3$ stabilises the potential at large ϕ and we can ignore operators with dimension > 6, although adding higher order terms with positive coefficients does not alter our results significantly.

The tunnelling process involve bubble profiles that are spatially spherically symmetric. It will be convenient to parametrise the $SU(2)$ triplet ϕ by a dimensionless profile h defined by

$$\phi^\dagger\phi = v^2 h^2. \tag{3.3}$$

For the homogeneous false vacuum decay the orientation of the scalar ϕ is arbitrary and constant, whereas for the monopole solution it is given by the hedgehog configuration (equation 3.13).

The tunnelling solutions will be dictated by the scalar field profile h. We will use a subscript 'fv' to refer to the false vacuum bounce solution, subscript 'm' to the static monopole profile and 'mb' to the monopole tunnelling solution. We will often make use of the rescaled potential V written in terms of h with the parameter λ factored out:

$$\lambda v^4 V(h) = V_\phi(v^2 h^2). \tag{3.4}$$

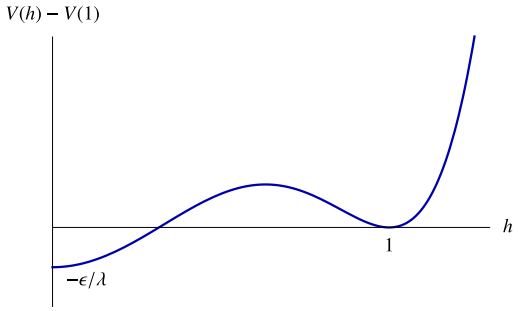

Figure 3.1: The scalar potential for the metastable monopole model, given a representative set of values.

In both cases we work in the zero temperature limit and assume that the effects of gravity are negligible.

3.1.1 False vacuum decay

The rate for the false vacuum tunnelling process, defined as the rate of bubble nucleation per unit volume is given by [75, 76]

$$\Gamma_{\rm fv} = A^4 e^{-B_{\rm fv}}. \tag{3.5}$$

The dominant suppression of the decay rate comes from the exponential dependence on the bounce action $B_{\rm fv}$, and the calculation of this quantity is the focus of this chapter. In equation (3.5) A is related to the determinant of fluctuations around the bounce solution [76], and only corrects the decay rate by logarithmic correction to $B_{\rm fv}$. Throughout this paper we will simply approximate $A \sim v$. $B_{\rm fv}$ is given by the Euclidean action S_E evaluated on the bounce solution $|\phi| = v h_{\rm fv}$

$$B_{\rm fv} = S_E[v h_{\rm fv}] - S_E[v], \tag{3.6}$$

where for our case of a single scalar field the action is given by

$$S_E[\phi] = \int dt_E d^3x \left[\frac{1}{2}|\partial\phi|^2 + V(\phi)\right]. \tag{3.7}$$

The bounce profile $h_{\rm fv}(t_E, \vec{x})$ is a solution to the Euclidean field equations and describes a field configuration where $h_{\rm fv}$ begins in the false vacuum state ($h_{\rm fv} = 1$) at $t_E \to -\infty$, evolves to a bubble of true vacuum before turning around and evolving along a time-reversed path to the false vacuum state [75]. The translational symmetry of the field equations

allows us to set the turning point of the solution to $t_E = 0$. It can be shown that in the zero temperature limit the solution obeys an $O(4)$ symmetry and depends only on the combination $\rho = \sqrt{t_E^2 + r^2}$ [77]. The field equations then become

$$h''_{\rm fv} + \frac{3}{\rho} h'_{\rm fv} = \lambda v^2 \frac{\partial V(h_{\rm fv})}{\partial h}, \tag{3.8}$$

with boundary conditions

$$h_{\rm fv}(\rho \to \infty) = 1, \qquad\qquad h'_{\rm fv}(0) = 0, \tag{3.9}$$

where $'$ denotes the derivate $\partial/\partial\rho$.

In general the solution $h_{\rm fv}$ can only be found by numerically integrating equation (3.8), however in the case where the two vacua are nearly degenerate a simplifying approximation can be made. In this case the solution remains near the true vacuum at $h = 0$ until ρ is large enough so that the friction term ($\propto h'_{\rm fv}$) is negligible before rapidly evolving to the false vacuum value $h_{\rm fv} = 1$. In this case the profile is given by the thin-wall approximation:

$$h_{\rm fv} = \begin{cases} 0, & \rho < R - \delta, \\ \bar{h}_{\rm fv}(\rho), & |\rho - R| < \delta, \\ 1, & \rho > R + \delta, \end{cases} \tag{3.10}$$

where $\bar{h}_{\rm fv}(\rho)$ interpolates between 0 and 1 in a small interval with length $2\delta \ll R$ around R.

The energy of a static bubble of radius R, relative to that of the false vacuum is given by

$$E_{\rm fv}(R) = -\frac{4\pi\epsilon v^4}{3} R^3 + 4\pi\sigma R^2, \tag{3.11}$$

where σ is the surface tension

$$\sigma = \sqrt{2\lambda} v^3 \int_0^1 dh \sqrt{V(h) - V(0)}. \tag{3.12}$$

$E_{\rm fv}$ has a maximum at $R_c = 2\sigma/(\epsilon v^4)$ and any bubble of true vacuum larger than this is unstable against expanding, as shown in figure 3.2. As $R = 0$ corresponds to the homogeneous false vacuum ($\phi = v$ everywhere) and energy must be conserved, the nucleated bubble will have radius $R_{\rm fv} = 3\sigma/(\epsilon v^4)$. A bubble nucleated at this radius will spontaneously expand with the latent heat released from converting a region of false vacuum to true vacuum driving the expansion of the bubble wall. This picture also highlights that the bounce solution is a saddle point of S_E, with a single negative mode corresponding to the expansion of the bubble.

The thin-wall limit, while instructive, is not generally applicable and applies only in the regime where the transition rate is most suppressed (nearly degenerate vacua separated by a large potential barrier). In general solutions to equation (3.8) have to be found numerically. A simple method to do this is using a shooting algorithm. The algorithm works by making a guess h_0 for the value of $h_{\rm fv}$ at $\rho = 0$, then solving equation (3.8) as an initial value problem with boundary conditions $h_{\rm fv}(0) = h_0$, $h'_{\rm fv}(0) = 0$. If the guess h_0 is too close to the true vacuum at $h = 0$ the solution found will "overshoot", evolving past the false vacuum $h = 1$ and diverging toward $+\infty$ at large ρ, while if the guess is too far from the true vacuum the solution will "undershoot" and reach a maximum value less than 1 before turning around and oscillating around the field value that maximises $V(\phi)$. The bounce solution separates the profiles that overshoot from those that undershoot.

3.1.2 Metastable monopole background

We now turn to the case where false vacuum decay can be seeded by magnetic monopoles, which act as impurity sites and catalyse the phase transition from the false to true vacuum. This effect is relevant when:

1. the scalar field ϕ is charged under a gauge group G and the false vacuum state breaks the gauge group G to a subgroup H,

2. the true vacuum state is the symmetry restored phase, $\phi = 0$,[1] and

3. the symmetry breaking pattern $G \to H$ leads to topological monopole solutions.

The symmetry breaking pattern (G spontaneously broken to a subgroup H) permits topological monopole solutions if the homotopy group $\pi_2(G/H)$ is non-trivial. Our setup, described above equation (3.1) is the simplest example where these conditions are satisfied. In this case the field profiles describing the monopole solution take the form

$$\begin{aligned} \phi^a &= v\hat{r}^a h_{\rm m}(r), \\ A_i^a &= \epsilon^{aij}\hat{r}^j \left(\frac{1 - u_{\rm m}(r)}{gr}\right), \\ A_0^a &= 0, \end{aligned} \tag{3.13}$$

[1] This assumption can be replaced by the less restrictive requirement that $\phi = 0$ is in the basin of attraction of the true vacuum, but we consider the case where $\phi = 0$ is precisely at the true vacuum both for simplicity and as this assumption maximises the effect under consideration.

where g is the gauge coupling, a indexes the adjoint representation of $SU(2)$ and i, j are spatial indices. At large values of r the scalar field must approach a point on the symmetry breaking minimum of the potential, $\phi^\dagger\phi = v^2$, which implies $h_\mathrm{m} \to 1$ as $r \to \infty$; while the gauge field profile u_m approaches 0 at large r, giving the coulomb field for a monopole with magnetic charge $Q_\mathrm{m} = 4\pi/g$. As each point on the spatial unit sphere is mapped to a distinct orientation in field space (as $\phi^a \propto \hat{r}^a$) the only way for this solution to be continuous as $r \to 0$ is if $h_\mathrm{m}(0) = 0$. The topology of the gauge field profile similarly requires that $u_\mathrm{m}(0) = 1$. By construction $h = 0$ is the true minimum of the potential V, so in some neighbourhood around the centre of the monopole the scalar field is in the true vacuum region of the potential. In this way, the monopole profile resembles the profile of a bubble nucleated in false vacuum decay.

When these assumptions hold there are now two separate processes that contribute to the decay of the false vacuum. The formalism described in section 3.1.1 is still valid when considering bubbles nucleated far from the core of a monopole, but around the core of a monopole the rate of bubble nucleation can be exponentially enhanced, as the interior of the monopole contains a region of true vacuum. If this interior region of the monopole is of a critical size, then the monopole can become classically unstable and will spontaneously expand – even if the false vacuum decay process is exponentially suppressed. If the monopole is smaller than the critical size, it can still decay via a tunnelling process where the monopole tunnels to a larger monopole before spontaneously expanding.

Similar to the false vacuum tunnelling process, the rate for this process will be dictated by bounce solutions to the Euclidean field equations. The exponent suppressing the monopole decay, B_mb, is the Euclidean action evaluated on these solutions. The decay rate of a single monopole is

$$\Gamma_{\mathrm{single-monopole}} = A' e^{-B_\mathrm{mb}}. \tag{3.14}$$

The contribution of the monopole channel to the false vacuum decay rate (per unit volume) in this case will then be given by

$$\Gamma_\mathrm{mb} = n_\mathrm{m} A' e^{-B_\mathrm{mb}}, \tag{3.15}$$

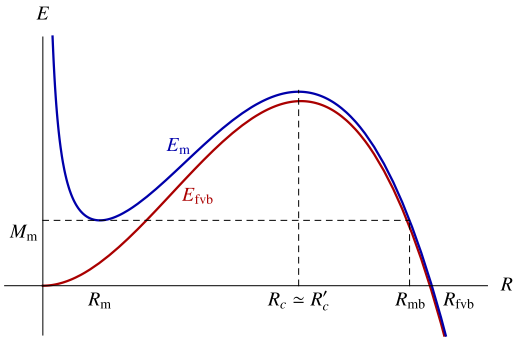

Figure 3.2: Energy of the metastable monopole (blue) and false vacuum bubble (red) as a function of radius in the thin-wall limit. We neglect differences in the tension of the two bubbles and set $\sigma = \sigma'$. The plot is illustrative of the shape of profiles in the thin-wall limit.

where $n_{\rm m}$ is the monopole number density. In general the pre-factors A in equation (3.5) and A' may be different, but we make the approximation that $A \sim A' \sim v$, which only affects the bounce action logarithmically. Due to the exponential dependence on $B_{\rm fv}, B_{\rm mb}$ in equations (3.5) and (3.15) if $B_{\rm mb} < B_{\rm fv}$ the monopole-catalysed decay can still dominate the false vacuum process even if $n_{\rm m}$ is very small.

3.1.3 Metastable monopoles in the thin wall limit

In this section we discuss the behaviour of metastable monopoles in the thin wall limit [239] and compare this to the false vacuum tunnelling process. This amounts to making a similar approximation to the one in equation (3.10), where the scalar field interpolates between the two vacua in a small region around the radius R. The detailed form of the profile $u_{\rm m}$ is not important at leading order, and it is assumed that $u_{\rm m}$ varies with the same characteristic radius as the scalar field [239]. In this limit the energy of the monopole can be written solely as a function of the radius R as

$$E_{\rm m}(R) = -\frac{4\pi\epsilon v^4}{3}R^3 + 4\pi\sigma' R^2 + \frac{2\pi}{g^2 R}, \tag{3.16}$$

where σ' is the surface tension of the monopole. σ' is in general different from the surface tension σ defined in equation (3.11) due to contributions from the gauge field profile, but these become less important at larger R values. For small ϵ the energy has a minimum at $R_{\rm m} \simeq \left(4g^2\sigma'\right)^{-1/3}$ and a maximum at $R_c \simeq 2\sigma'/(\epsilon v^4)$. Comparing this with the energy (3.10) of a bubble nucleated in a false vacuum tunnelling process we see there is a minimum generated at a small radius in the monopole case due to the

additional term $2\pi/(g^2 R)$, as shown in figure 3.2. The monopole can thus be thought of as as a sub-critical bubble of true vacuum which is stabilised by the magnetic self-energy in the thin-wall limit.[2] Therefore, monopoles do not collapse to zero size, whereas sub-critical false vacuum bubbles do.

Choosing parameters such that $R_{\rm m} = R_c$ (i.e. if g is sufficiently small) leads to a monopole which is classically unstable and will spontaneously expand as was the case discussed in ref.'s [236–238]. Even if $R_{\rm m} < R_c$ the monopole can tunnel to a monopole solution of (super)-critical size ($R \geq R_c$) at which point it will spontaneously expand. In contrast, the false vacuum case can be thought of as tunnelling from the $R = 0$ homogeneous false vacuum to a bubble of size $R \geq R'_c$. It is therefore a natural expectation that the bounce action for monopole decay should be smaller than the false-vacuum bounce.

The monopole bounce action in the thin-wall approximation was studied in ref. [239], their result was:

$$\frac{B_{\rm mb}}{B_{\rm fv}} = \frac{32\sqrt{2}}{105\pi}\left(1 - \frac{R_m}{R_{\rm mb}}\right)^{5/2} I\left(\frac{R_m}{R_{\rm mb}}\right), \tag{3.17}$$

where I is an $\mathcal{O}(1)$ function. Here $R_{\rm mb}$ is the radius of the bubble after tunnelling, given by $E_{\rm m}(R_{\rm mb}) = E_{\rm m}(R_{\rm m})$ as required by energy conservation. This expression makes explicit the classical instability as $R_{\rm m} \to R_{\rm mb}$ and the barrier in $E_{\rm m}(R)$ disappears.

3.1.4 Thin wall limitations

The thin wall limit only gives a good approximation to the true monopole solution in a limited set of circumstances. In general, the field profiles $h_{\rm m}, u_{\rm m}$ have a thick-walled profile which is determined by the field equations

$$\begin{aligned} h''_{\rm m} + \frac{2}{s}h'_{\rm m} &= \frac{2h_{\rm m}u_{\rm m}^2}{s^2} + \frac{\lambda}{g^2}\frac{\partial V(h_{\rm m})}{\partial h}, \\ u''_{\rm m} &= \frac{u_{\rm m}(u_{\rm m}^2 - 1))}{s^2} + h_{\rm m}^2 u_{\rm m}, \end{aligned} \tag{3.18}$$

where $s = gvr$ is a rescaled radial coordinate.

The usual justification for the thin-wall approximation is that an equation of motion of the form of equation (3.8) can be thought of as describing a particle (with position φ, 'time'

[2]Note that global monopoles are also stable against collapse – in this case the outward pressure is provided by the gradient energy of the scalar field profile, which is fixed to vanish at the origin due to topology. However, there is no thin-wall limit for global monopoles.

coordinate ρ) moving on an inverted potential $-V(\varphi)$ with a ρ-dependent friction term. If the minima of V are nearly degenerate (i.e. if $\epsilon \ll 1$) the particle must remain at the true vacuum point of the potential until the friction term becomes negligible before moving rapidly to the false vacuum minimum of the potential. Comparing equation (3.18) to (3.8), it is clear that this logic does not apply straightforwardly for the monopole equation of motion due to presence of the interaction term $2hu^2/s^2$. In particular, if we take the limit that the interaction dominates the term from the scalar potential, $\lambda/g^2 \ll 1$ (known as the BPS limit [262]), then the exact solution is known to be:

$$h_{\rm bps}(s) = \coth(s) - \frac{1}{s}, \quad u_{\rm bps}(s) = \frac{s}{\sinh(s)}, \tag{3.19}$$

and does not describe a thin-wall profile, regardless of the value of ϵ. We therefore expect that a thin wall approximation for the scalar field profile is only valid for both $\lambda \gg g^2$ and $\epsilon \ll 1$, while more general monopoles will have a thick-walled profile.

At distances $s \lesssim g\lambda^{-1/2}$ from the centre of the monopole the potential term is always negligible in comparison to the interaction term. Expanding equation (3.18) for small s the leading term for h is linear in s, and this coefficient is only non-zero due to the interaction term in the equation. This is in conflict with the assumption that the scalar field stays exponentially close to the true vacuum value inside the thin wall bubble, which is crucial to deriving the first term of equation (3.16). Even for small deviations of h from zero, $V(h)$ can become positive since the thin wall limit requires $|V(0)| = \epsilon \ll 1$. As the EOM for $u_{\rm m}$ contains no additional parameters, we similarly expect that $u_{\rm m}$ evolves smoothly between 1 and 0 as s varies by an $\mathcal{O}(1)$ amount, although this does not significantly affect the validity of the thin wall approximation of the bounce action.

While the thin wall approximation for the monopole profile is only expected to hold for a specific set of parameters we expect that the intuitive picture derived from this approximation should apply more generally. A thick-walled monopole must have a region at its core which is in the true vacuum region of the potential and therefore we expect that a bubble nucleated around a monopole should have a smaller bounce action than a bubble nucleated from the homogenous false vacuum. This motivates looking at more general monopole profiles to determine the bounce action which describes their decay,

although this is complicated by the fact that they can no longer be described solely by their radius. The calculation of this process in generality is the main result of this work, which we present in the next section.

3.2 General Monopole Tunnelling

In this section we describe a numerical method for calculating the bounce action for the tunnelling process initiated by a monopole. The bounce action for this process is given by:

$$B_{\rm mb} = S_E[h_{\rm mb}, u_{\rm mb}] - S_E[h_{\rm m}, u_{\rm m}], \tag{3.20}$$

where S_E is the Euclidean action for the gauge field and triplet scalar, and $h_{\rm m}, u_{\rm m}$ are the monopole field profiles obtained from solving equation (3.18).

The functions $h_{\rm mb}, u_{\rm mb}$ describe the tunnelling process from the monopole solution to a critical bubble of true vacuum and will depend on the variable s and the (rescaled) Euclidean time $\tau = gvt_E$, assuming the monopole bounce solutions retain the $O(3)$ symmetric dependence on the spatial coordinates. They solve the equations of motion

$$\begin{aligned} \ddot{h}_{\rm mb} + h''_{\rm mb} + \frac{2}{s}h'_{\rm mb} &= \frac{2h_{\rm mb}u^2_{\rm mb}}{s^2} + \frac{\lambda}{g^2}\frac{\partial V(h_{\rm mb})}{\partial h}, \\ \ddot{u}_{\rm mb} + u''_{\rm mb} &= \frac{u_{\rm mb}(u^2_{\rm mb}-1)}{s^2} + h^2_{\rm mb}u_{\rm mb}, \end{aligned} \tag{3.21}$$

where a $\dot{}$ denotes $\partial/\partial\tau$ and $'$ denotes $\partial/\partial s$. There are two boundary conditions enforced by the topology of the profiles, $h_{\rm mb}(\tau, 0) = 0$ and $u_{\rm mb}(\tau, 0) = 1$, and in order to have a finite tunnelling action we require that $h_{\rm mb}, u_{\rm mb}$ approach the monopole solutions $h_{\rm m}(s), u_{\rm m}(s)$ as $|\tau| \to \infty$. Combined with the symmetry of the equations under $\tau \to -\tau$ this implies that for some τ the derivatives $\dot{h}_{\rm mb}, \dot{u}_{\rm mb}$ vanish. As the equations are invariant under shifts in τ we can choose this point to be $\tau = 0$, giving us the final boundary condition $\dot{h}_{\rm mb}(0, s) = \dot{u}_{\rm mb}(0, s) = 0$.

3.2.1 Mountain pass theorem

The system of equations (3.21) does not allow us to make the simplifications usually made when calculating the analogous expressions for tunnelling from the homogeneous false vacuum. Due to the explicit dependence on s on the right hand side of equation (3.21), and the s-dependence of the boundary profiles $h_{\rm m}(s), u_{\rm m}(s)$ the solutions will no longer

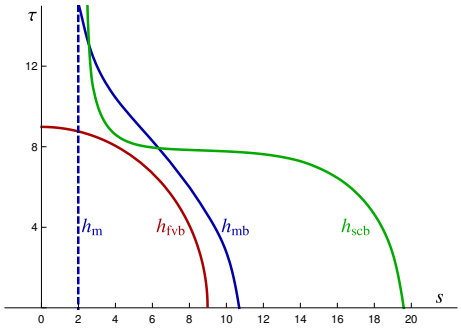

Figure 3.3: Lines in τ, s space which seperate the true vacuum and false vacuum regions for the $O(4)$ bounce solution (red), the monopole tunnelling solution (blue), the static monopole solution (blue dashed) and the supercritical profile (green). Parameters for each are $\lambda = 1/2$, $\epsilon = 5 \times 10^{-2}$, $g = 1$. To the left of each of the lines the relevant function is in the true vacuum region of the potential, while to the right they are on the false vacuum side of the potential.

obey an $O(4)$ symmetry and will instead depend independently on τ and s. In figure 3.3 we show contours of the profiles $h_{\rm m}$, the $O(4)$ symmetric false vacuum bounce $h_{\rm fv}$ and the monopole bounce $h_{\rm mb}$ that separate the false vacuum region from the true vacuum region in each case. Comparing the monopole and false vacuum bounce profiles it is clear that $O(4)$ symmetry is not a good approximation for the monopole bounce. The monopole bounce $h_{\rm mb}$ and the supercritical bounce $h_{\rm scb}$ are discussed in detail below.

This makes the system of equations (3.21) much more difficult to solve (at least in the absence of an approximation scheme such as the thin wall approximation). If we were to try to implement a shooting-type algorithm similar to the one described at the end of section 3.1.1 we would now need to guess the complete field profiles $h_{\rm mb}(0, s)$ and $u_{\rm mb}(0, s)$ for which the solutions asymptote to $h_{\rm m}(s)$ and $u_{\rm m}(s)$ as $\tau \to \infty$ after solving the equations of motion. This is impractical, both as it requires guessing the two complete field profiles and there is no way we know of to systematically improve the guess depending on the form of the asymptotic solutions found given an initial guess.

Instead, we use the fact that the solution we are looking for is a saddle point of S_E. If an initial guess which is close to the tunnelling solution is known in advance, it is possible to find the solution by varying the profiles so that they better satisfy the equations of motion [263]. However, this approach is limited by the need for a good initial guess, as there are other solutions to the field equations which the algorithm can relax to. Instead, we use a more generic algorithm which does not rely on the initial guess for convergence. It makes use of a theorem known as the mountain pass theorem (MPT) [264] to turn the

problem of solving equations (3.21) into a minimisation problem, which can then be solved using a gradient descent algorithm. The use of the MPT allows us to find the bounce solutions without the requirement of a good initial guess for the profiles. The MPT is well-known, but its application to tunnelling in quantum field theory is novel.

The MPT applies to a functional $I[f]$ which maps a Hilbert space H to the reals and satisfies the following conditions:

- I is differentiable and the derivative I' is Lipschitz continuous on bounded subsets of H;
- I satisfies the Palais Smale compactness condition, which guarantees the existence of a saddle point;
- $\exists f_0 \in H$ such that $I[f_0] = 0$ and f_0 is a local minimum of I;
- $\exists f_1 \in H$ such that $I[f_1] < 0$.

Considering the set of continuous paths that interpolate between f_0 and the function f_1

$$P = \{\gamma : [0,1] \to H \,|\, \gamma(0) = f_0, \gamma(1) = f_1\}, \tag{3.22}$$

then the statement of the MPT is that the point

$$x = \min_{\gamma \in P} \max_{\alpha \in [0,1]} I[\gamma(\alpha)] \tag{3.23}$$

is a critical point of I. The intuition behind the theorem is that if we consider all paths which start at a minimum of I where $I = 0$ and end at a point where $I < 0$, each path must reach a point where I is maximum along the path (and I is necessarily positive) and turn around. The path whose maximum point is smallest crosses through a saddle point of I at this point. A simple example of such a set of paths is shown in figure 3.4. For each choice of path the maximisation picks out a point on the ridge, ensuring that the action is not lowered by exciting the negative mode. Therefore $\max_{\alpha \in [0,1]} I[\gamma(\alpha)]$ as a function of paths is robust against unstable modes and can be minimised using gradient descent methods.

The utility of the MPT for our purposes comes from realising that

$$I[h, u] = S_E[h, u] - S_E[h_{\mathrm{m}}, u_{\mathrm{m}}] \tag{3.24}$$

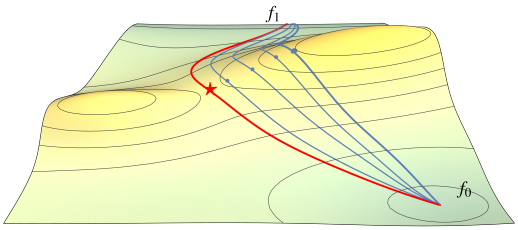

Figure 3.4: Mountain pass theorem in a two-dimensional example. Five paths interpolating between the minimum at f_0 and the negative point at f_1 are shown, where the red path passes through the saddle point (indicated by the red star). The blue dots show the maximum point along each of the other paths.

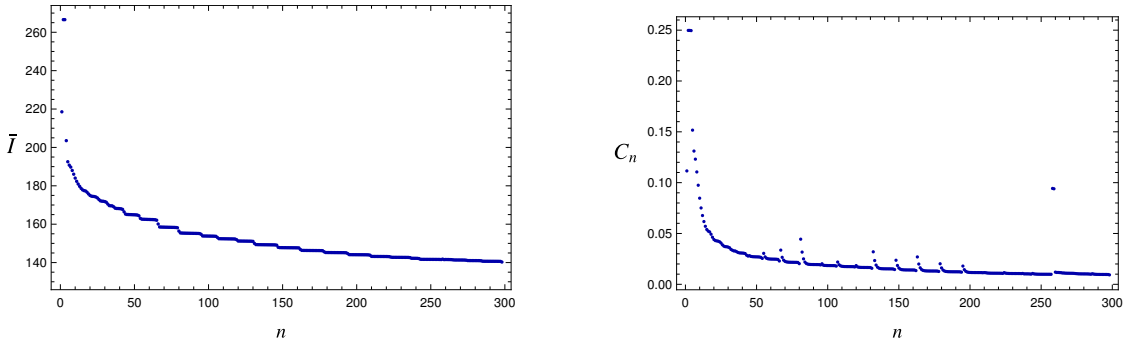

Figure 3.5: Value of the action $\bar{I}$ (left panel) and the cost function C_n (right panel) for the field profiles $h_{\bar{\alpha}}, u_{\bar{\alpha}}$ as a function of the number iterations performed. Jumps in the values of C_n are due to changes in the value of $\bar{\alpha}$ as the algorithm proceeds.

satisfies the conditions for the theorem to apply, and the solution $(h_{\rm mb}, u_{\rm mb})$ we are looking for is a saddle point of I. The monopole solution $(h_{\rm m}, u_{\rm m})$ for a metastable monopole is a local minimum of I with $I[h_{\rm m}, u_{\rm m}] = 0$, and we can consider a field configuration describing a supercritical bubble $(h_{\rm scb}, u_{\rm m})$ which contains a large true vacuum region. A sufficiently large region of true vacuum will lead to $I[h_{\rm scb}, u_{\rm m}] < 0$, so the point $(h_{\rm scb}, u_{\rm m})$ in field space is the point f_1. If we consider paths which interpolate between $(h_{\rm m}, u_{\rm m})$ and $(h_{\rm scb}, u_{\rm m})$ then minimise the maximum value of I along this set of paths we will approach the saddle point solution $(h_{\rm mb}, u_{\rm mb})$.

3.2.2 Mountain pass algorithm

Given the parametrisation of the scalar potential in equation (3.1) the solution for the monopole bounce $B_{\rm mb}$ depends on three parameters: λ, g, ϵ. For a given set of these parameters we first find the monopole solutions $h_{\rm m}(s), u_{\rm m}(s)$ by solving equation (3.18) using a modified shooting algorithm.We then construct the solution $h_{\rm scb}$ by using a

convenient interpolation between the monopole profile and a supercritical bubble:

$$\begin{aligned} h_{\mathrm{scb}}(\tau, s) &= \left(1 - e^{-(\tau/T)^2}\right) h_{\mathrm{m}}(s) + e^{-(\tau/T)^2} h_{\mathrm{sc}}(s, S, \delta), \\ h_{\mathrm{sc}}(s, S, \delta) &= \frac{1}{2}\left[1 + \tanh\left(\frac{s - S}{\delta}\right)\right]. \end{aligned} \tag{3.25}$$

The parameters T, S, and δ are chosen such that $I[h_{\mathrm{scb}}, u_{\mathrm{m}}] < 0$. An example of one such field profile is shown in figure 3.3. T sets the time scale over which the scalar field varies between the bubble profile h_{sc} and the monopole solution $h_{\mathrm{m}}(s)$, S sets the radius of the bubble profile and δ the thickness of the bubble. For $\delta \ll S$ this ansatz satisfies the boundary conditions for the equation of motion.

Having found the start and end points of the paths we want to consider, the next step is to choose a continuous interpolation between the monopole and supercritical solutions $h_\alpha(\tau, s), u_\alpha(\tau, s)$ for $0 \leq \alpha \leq 1$ such that $(h_0, u_0) = (h_{\mathrm{m}}, u_{\mathrm{m}})$ and $(h_1, u_1) = (h_{\mathrm{scb}}, u_{\mathrm{m}})$. This interpolation represents one choice of path between the endpoints, the task now is to find the path which passes through the saddle point of I. We present the algorithm here assuming h_α, u_α are continuous in τ, s and α, and give details on the discretised version in appendix A. Having constructed the initial guess, the algorithm then proceeds as follows:

1. At a given step n in the iteration calculate the functional

$$I[h_\alpha^n, u_\alpha^n] = S_E[h_\alpha^n, u_\alpha^n] - S_E[h_{\mathrm{m}}, u_{\mathrm{m}}], \tag{3.26}$$

   for $0 \leq \alpha \leq 1$. Let $\bar{\alpha}$ be the value for which $h_{\bar{\alpha}}^n, u_{\bar{\alpha}}^n$ maximise I and let $\bar{I} = I[h_{\bar{\alpha}}^n, u_{\bar{\alpha}}^n]$ be this maximum value.

2. The functions $h_{\bar{\alpha}}^n, u_{\bar{\alpha}}^n$ are then updated to decrease the action $I[h_{\bar{\alpha}}^n, u_{\bar{\alpha}}^n]$ using a gradient descent algorithm

$$\begin{aligned} h_{\bar{\alpha}}^{n+1} &= h_{\bar{\alpha}}^n - \beta_n \frac{\delta \bar{I}}{\delta h_{\bar{\alpha}}^n}, \\ u_{\bar{\alpha}}^{n+1} &= u_{\bar{\alpha}}^n - \beta_n \frac{\delta \bar{I}}{\delta u_{\bar{\alpha}}^n}, \end{aligned} \tag{3.27}$$

   where β_n is a step size, which we discuss in further detail in section A.

   Performing this step only on the functions $h_{\bar{\alpha}}^n, u_{\bar{\alpha}}^n$, however, will lead to $h_\alpha^{n+1}, u_\alpha^{n+1}$ becoming discontinuous in α, violating a necessary condition on the choice of paths for the MPT to apply. To vary the functions while preserving continuity in α and

keeping the endpoints at $\alpha = 0, 1$ fixed, we vary $h_\alpha^{n+1}, u_\alpha^{n+1}$ in the same direction as the change in $h_{\bar{\alpha}}^n, u_{\bar{\alpha}}^n$ but with a step size defined by a continuous function $F(\alpha, \bar{\alpha})$ such that $F(\bar{\alpha}, \bar{\alpha}) = 1, F(0, \bar{\alpha}) = F(1, \bar{\alpha}) = 0$, leading to

$$\begin{aligned} h_\alpha^{n+1} &= h_\alpha^n - \beta_n F(\alpha, \bar{\alpha}) \frac{\delta \bar{I}}{\delta h_{\bar{\alpha}}^n}, \\ u_\alpha^{n+1} &= u_\alpha^n - \beta_n F(\alpha, \bar{\alpha}) \frac{\delta \bar{I}}{\delta u_{\bar{\alpha}}^n}. \end{aligned} \tag{3.28}$$

We find that the specific choice of F has little effect on the convergence of the algorithm provided the choice retains the required continuity in α.

The variations of the field profiles at each step are simply the equations of motion evaluated on the field profiles $h_{\bar{\alpha}}^n, u_{\bar{\alpha}}^n$, albeit with a non-standard normalisation. Removing the indices $n, \bar{\alpha}$ for clarity, they are given by

$$\begin{aligned} \frac{\delta I}{\delta h} &= -\frac{8\pi s^2}{g^2} \left(\ddot{h} + h'' + \frac{2}{s} h' - \frac{2hu^2}{s^2} - \lambda \frac{\partial V(h)}{\partial h} \right), \\ \frac{\delta I}{\delta u} &= -\frac{16\pi}{g^2} \left(\ddot{u} + u'' - \frac{u(u^2 - 1)}{s^2} - h^2 u \right). \end{aligned} \tag{3.29}$$

3. The magnitude of the change in field profiles is dependent on how well the equation of motion is satisfied at each point, and the algorithm will terminate when the equations of motion are satisfied.

   In practice, we define a lattice of points (τ_j, s_i) and a cost function C_n which gives a measure of how well the equation of motion is satisfied by the field profiles[3]

$$C_n = \frac{1}{N_s N_\tau} \left[\sum_{ij} \left(\left(\frac{\delta \bar{I}}{\delta h_{\bar{\alpha}}^n} \right)_{ij}^2 + \left(\frac{\delta \bar{I}}{\delta u_{\bar{\alpha}}^n} \right)_{ij}^2 \right) \right]^{1/2}, \tag{3.30}$$

   where N_s, N_τ are the number of points in s, τ that we sample and

$$(h_{\bar{\alpha}}^n)_{ij} = h_{\bar{\alpha}}^n(\tau_j, s_i), \ (u_{\bar{\alpha}}^n)_{ij} = u_{\bar{\alpha}}^n(\tau_j, s_i). \tag{3.31}$$

   The cost function can be thought of as a measure of how well the field profiles $h_{\bar{\alpha}}^n, u_{\bar{\alpha}}^n$ satisfy the equations of motion.

   The condition we use to terminate the algorithm is that $C_n < 10^{-2}$. As a final step the PDE is solved numerically for a perturbation around the solution found by the

[3] For full details of the discretised algorithm we refer the reader to section A.

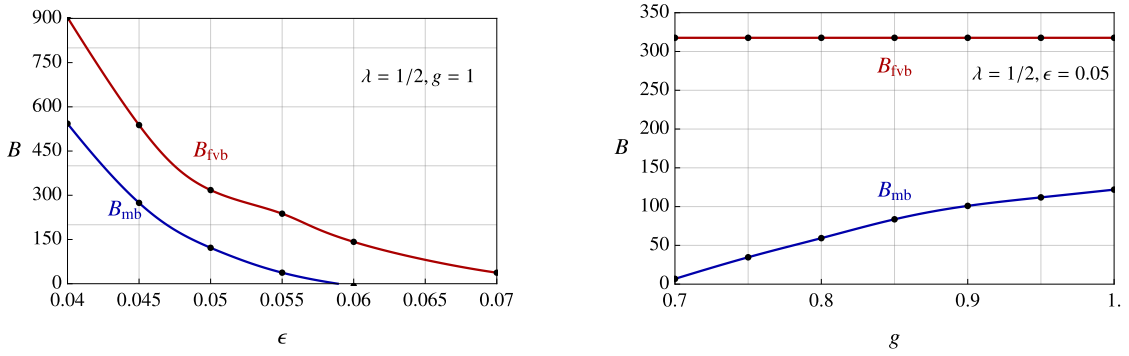

Figure 3.6: Plots showing the bounce action for bubble nucleation around a monopole ($B_{\rm mb}$) compared to the usual false vacuum bounce ($B_{\rm fv}$). The left panel shows the two bounce actions as a function of ϵ for $\lambda = 1/2, g = 1$, the right panel shows the bounce actions as a function of g for $\lambda = 1/2, \epsilon = 0.05$. The false vacuum bounce is independent of the gauge coupling so is constant in the right hand plot, showing that the monopole may be classically unstable (for $g < 0.7$ in our results) while the false vacuum decay is still exponentially suppressed.

algorithm described above, but find that the perturbation found in this way amounts to a sub-percent level correction to the field profiles at each point. The choice of the termination condition is validated by requiring that the perturbations found by the PDE solver are small.

In figure 3.5 we show the action $\bar{I}$ and the cost C_n as a function of the number of iterations n. In a gradient descent algorithm, the value of the action $\bar{I}$ is expected to decrease monotonically. This is not true for our implementation in general, as each iteration decreases $I[h_\alpha, u_\alpha]$ at a fixed value of α. This might cause the value of α for which the updated profiles (h_α, u_α) maximise I to change, and possibly also cause $\bar{I}$ to increase. In such a case, the algorithm switches to updating the set of profiles at the new value of $\bar{\alpha}$ and proceeding with the gradient descent method. As can be seen from the right panel of figure 3.5, this behaviour does not prevent the algorithm from converging.

3.2.3 Numerical results

In this section, we present results comparing the monopole-catalysed and false vacuum decays in the simplified model described in section 3.1. We choose generic, $\mathcal{O}(1)$ values of the couplings λ, g and take $\epsilon \lesssim \lambda/6$ as required for the potential to retain a metastable vacuum.

In the left panel of figure 3.6 we show the bounce action $B_{\rm mb}$ for tunnelling induced by a monopole in comparison to the false vacuum bounce $B_{\rm fv}$ for different parameter values.

The left panel of figure 3.6 shows the two bounce actions for $\lambda = 1/2, g = 1$ and varying ϵ. The monopole bounce $B_{\rm mb}$ is always smaller than the false vacuum bounce and approaches a classical instability ($B_{\rm mb} \to 0$) at $\epsilon \sim 5.8 \times 10^{-2}$, where for the same choice of parameters $B_{\rm fv} \sim 140$ so the false vacuum tunnelling rate is suppressed by a factor $\Gamma_{\rm fv} \propto e^{-140}$.

The right panel of figure 3.6 shows the results for fixed $\lambda = 1/2$ and $\epsilon = 5 \times 10^{-2}$ and varying the coupling g. The false vacuum bounce is independent of the gauge coupling and is constant at $B_{\rm fv} \sim 317$ while the monopole bounce decreases for smaller g, with the monopoles becoming classically unstable for $g \lesssim 0.7$. As the monopole size scales like g^{-1}, decreasing g implies that the monopole contains a larger region of true vacuum at its core which for sufficiently large size to become classically unstable.

From equations (3.5) & (3.15) the monopole induced rate will dominate that of tunnelling from the homogenous false vacuum for a monopole abundance which satisfies

$$n_m \gtrsim v^3 e^{B_{\rm mb} - B_{\rm fv}}. \tag{3.32}$$

This can be written in terms of the ratio of the monopole number density per Hubble volume as

$$\frac{n_m}{H^3} > e^{B_{\rm mb} - B_{\rm fv}} \left(\frac{\pi^2 g_*}{30}\right)^{-3/2} \left(\frac{v M_P}{T^2}\right)^3, \tag{3.33}$$

assuming a radiation dominated universe with g_* degrees of freedom. The difference in the bounce actions for each of the points shown in figures 3.6 falls in the range

$$\begin{aligned} B_{\rm mb} - B_{\rm fv} &\in [-360, -150]\,, \\ \implies e^{B_{\rm mb} - B_{\rm fv}} &\in \left[4 \times 10^{-157}, 8 \times 10^{-66}\right]. \end{aligned} \tag{3.34}$$

If we take the monopoles to be produced via the Kibble-Zurek mechanism (discussed further in section 3.3.1) when the universe has a temperature $T_* \sim v$ then we would expect of order 1 monopole per Hubble volume at this temperature [126, 127]. As the universe cools the monopole abundance scales as:

$$n_{m,\rm kibble} = H_*^3 \left(\frac{T}{T_*}\right)^3 \simeq H^3 \left(\frac{v}{T}\right)^3, \tag{3.35}$$

for constant g_*. In this case we find that the monopole-catalysed process will dominate the false vacuum phase transition rate for:

$$\frac{T}{M_P} \gtrsim 1.7 \times 10^{-23} \left(\frac{e^{B_{\rm mb} - B_{\rm fv}}}{10^{-66}}\right)^{1/3}. \tag{3.36}$$

For any viable BSM phase transition monopoles produced through the Kibble-Zurek mechanism will give the dominant contribution to the phase transition rate, within all of our parameter space.

We can also consider the stability of the present-day vacuum in the presence of a monopole population which makes up a fraction Ω_m of the total energy density of the universe. The condition that the monopole induced rate dominates the false vacuum rate is that:

$$\Omega_m > 1.3 \times 10^{-23} g^3 \left(\frac{M_m}{\text{GeV}}\right)^4 \left(\frac{e^{B_{\text{mb}} - B_{\text{fv}}}}{10^{-66}}\right), \tag{3.37}$$

where g is the gauge coupling and we have used the approximate relation $M_m = 4\pi v/g$. For example, a single monopole in our Hubble patch $\Omega_m \sim M_m H/M_P^2$ dominates the decay if $B_{\text{mb}} - B_{\text{fv}} \lesssim -300$ for monopole masses of order $M_m \sim$ TeV and $B_{\text{mb}} - B_{\text{fv}} \lesssim -386$ for monopole masses of order $M_m \sim M_{\text{GUT}} \sim 10^{16}$ GeV.

For monopoles with magnetic charge under $U(1)_{\text{em}}$, there is a bound on the monopole abundance [133, 134]

$$\Omega_m < 1.3 \times 10^{-16} \left(\frac{M_m}{\text{GeV}}\right) \left(\frac{\beta_m}{10^{-3}}\right)^{-1}, \tag{3.38}$$

assuming a constant monopole density throughout the universe, where β_m is the velocity of monopoles in the galaxy. The critical value of the bounce action required for electromagnetic monopoles to play a significant role in catalysing vacuum decay today depends on their mass. For monopoles with mass $M_m \sim$ TeV conditions (3.37) & (3.38) can be satisfied for $B_{\text{mb}} - B_{\text{fv}} \lesssim -163$, while if $M_m \sim M_{\text{GUT}}$ then both requirements are satisfied for $B_{\text{mb}} - B_{\text{fv}} \lesssim -258$.

3.3 Phenomenological Implications

The results of section 3.2 highlight the significant enhancement in the false vacuum decay rate due to the presence of magnetic monopoles in a simple model. In this section we present some examples illustrating how our calculation of monopole-induced tunnelling could apply in more general models of BSM physics.

3.3.1 Metastable monopole production

A common method by which monopoles are produced in the early universe is via the Kibble-Zurek mechanism [126, 127]. This occurs when the universe undergoes a phase transition to the symmetry-broken phase, where the symmetry breaking pattern allows monopole solutions. Points separated by distances larger than the correlation length exit the phase transition at different points on the vacuum manifold, resulting in twisted field configurations which relax to magnetic monopole solutions.

This can be a viable production for metastable monopoles in theories with two-step phase transitions where the $SU(2)$ gauge group is unbroken at high temperatures, is then broken in the first phase transition where monopoles are produced via the Kibble-Zurek mechanism. In the second phase transition an $SU(2)$ preserving vacuum state becomes the lowest energy state making the monopole metastable. An example of this was considered in ref.'s [236, 237] in the context of an $SU(5)$ GUT breaking to $SU(4) \times U(1)$ before breaking to the SM. Another related possibility is that during the cosmological evolution after the first phase transition, the symmetry-breaking vacuum (which is initially the preferred vacuum) becomes metastable due to thermal corrections to the potential. The monopole abundance in either case is $\mathcal{O}\left(\xi^{-3}\right)$, where ξ is the correlation length of the phase transition, which is Hubble scale for a first order transition but can be significantly smaller than Hubble for second-order transitions [265].

The Kibble-Zurek mechanism requires the early phase of the universe to be one in which the $SU(2)$ symmetry is restored, however we can consider alternate production mechanisms when this is not the case. Examples of this are monopoles produced by Hawking evaporation of primordial black holes [266], Schwinger pair-production in magnetic fields [267] or in high-energy particle collisions [268]. As the monopoles can be classically unstable when the false vacuum tunnelling process is exponentially suppressed, even if magnetic monopoles are very rarely produced through particle collisions or black hole evaporation, these processes may still trigger false vacuum decay. Another interesting production mode that has recently been considered is through the Kibble-Zurek mechanism operating in the thermal plasma surrounding an evaporating black hole [269].

3.3.2 GUT phase transitions

Although we considered the simplest possible case of a scalar potential with true vacuum at $\phi = 0$, monopole decay may also be relevant for theories where the field values at the monopole core may not be at the precise true vacuum, but simply in the basin of attraction of the true vacuum. This can have implications for the lifetime of the current vacuum state of the universe. If the UV completion of the SM is described by a GUT, then it is possible that the universe is in a metastable phase described by

$$\langle \Phi_{\rm GUT} \rangle = M_{\rm GUT}, \tag{3.39}$$

where $\Phi_{\rm GUT}$ is a scalar field which spontaneously breaks the GUT symmetry. At the core of a GUT monopole, $\langle \Phi_{\rm GUT} \rangle = 0$ and if this field value is in the basin of attraction of a new, lower minimum in the scalar potential then GUT monopoles are metastable. One way that this could occur is through interplay with the Higgs potential. As is well known, current experimental measurements of the top Yukawa indicate that the Higgs quartic turns negative at a large field value $h > 10^{10}$ GeV [270]. This contribution can help ensure that a second minimum with a lower vacuum energy exists, however, the details are model dependent. Given that this decay has evidently not occurred at any point in our past lightcone, this can be used to put bounds on the abundance of GUT monopoles, although we leave a detailed analysis of this possibility for future work.

3.3.3 Gravitational waves

The gravitational wave signal from a first order phase transition can also be significantly altered if it is catalysed by a population of magnetic monopoles. The fraction of the total energy emitted as gravitational waves scales and the peak frequency of the resulting spectrum scale as [98–101, 115, 116]

$$\begin{aligned} \frac{E_{\rm GW}}{E_{\rm vac}} &\propto \left(\frac{H}{\beta}\right)^2, \\ \omega_{\rm max} &\propto \beta, \end{aligned} \tag{3.40}$$

where β^{-1} is the time the nucleated bubbles evolve before colliding and H is the Hubble rate at the time of the phase transition. As the bubbles rapidly accelerate until

they are moving at the speed of light, β^{-1} is given by the average separation of bubbles when they are nucleated.[4]

For the false vacuum process β^{-1} is determined solely by the bounce action and how it varies with time, as bubbles are equally likely to be nucleated at any point in space. If the magnetic monopoles are homogeneously distributed with number density larger than one per Hubble volume the monopole catalysed process behaves in the same way as the false vacuum transition, although the rate may differ. If the phase transition completes more rapidly due to the presence of monopoles the amplitude of the gravitational wave signal will be decreased and shifted to higher frequencies. However, if the population of monopoles is not uniformly distributed on Hubble scales then β^{-1} will instead be set by the average separation of the monopoles. In this case there is also the possibility that there may be multiple scales on which bubbles of different sizes collide, leading to a spectrum with multiple peaks of differing intensity. Furthermore, the topology of the bubble walls may introduce additional interactions between the walls or between the walls and the thermal plasma which may modify the dynamics of the wall.

A further interesting possibility is that the distribution of monopoles could lead to an observable anisotropy in the gravitational wave spectrum. In ref. [271] it was shown that upcoming gravitational wave experiments are potentially sensitive to spatial anisotropies in the gravitational wave signal from a first order phase transition. It was also shown that for a generic first order phase transition that this spectrum should be proportional to the temperature anisotropy,

$$\frac{\delta\rho_{GW}(\theta,\phi)}{\rho_{GW}} \propto \frac{\delta T(\theta,\phi)}{T}, \tag{3.41}$$

and therefore gives a second copy of the CMB (without the effects of Silk damping and baryon acoustic oscillations). If the phase transition was instead catalysed by a population of magnetic monopoles whose abundance has a spatial dependence that is not correlated with temperature this could lead to a spatial variation in the gravitational wave signal that is not aligned with the CMB. One example of how this may occur is if primordial magnetic fields bias the Kibble-Zurek mechanism to produce more monopoles in some

[4]Here we are ignoring interactions of the bubble walls with the thermal plasma.

regions of space than others. The gravitational wave anisotropy would then additionally track the anisotropy in the monopole number density

$$\frac{\delta\rho_{GW}(\theta,\phi)}{\rho_{GW}} \sim \frac{\delta n_m(\theta,\phi)}{n_m}, \tag{3.42}$$

which in turn depends on the magnetic field strength at different points in space.

Chapter 4

Domain Walls Catalysing the Electroweak Phase Transition

A first order electroweak phase transition (EWPT) represents a target for upcoming gravitational wave experiments. The transition is second order within the SM alone [31, 36–40], however, extensions to the SM introducing new physics at the electroweak scale lead to a first order EWPT (see, e.g. [49–53]). This can lead to an observable gravitational wave signal [98–101] and could also explain the observed baryon asymmetry of the universe [6, 29]. In particular, LISA has sensitivity in the correct frequency range to observe gravitational waves emitted during a first order EWPT [9].

One possible extension to the SM which can lead to a first order EWPT is the addition of a real scalar singlet S with a $\mathbb{Z}_2$ symmetry, S [272–288]. In this model the transition has two steps, where in the first step the $\mathbb{Z}_2$ symmetry is spontaneously broken via the vev of S while the Higgs vev remains zero. Below the electroweak scale, the Higgs acquires its electroweak vev, $v_{\rm ew}$ and $S = 0$, restoring the $\mathbb{Z}_2$ symmetry. In the typical setup, the first step is a second order transition while the second step can be first order, depending on the choice of the portal coupling between S and the Higgs.

The breaking of the $\mathbb{Z}_2$ symmetry in the first step of the phase transition leads to the formation of domain walls through the Kibble-Zurek mechanism [126–128]. In ref. [289], it was shown that these domain walls act to catalyse the EWPT in this model, in an analogous manner to the monopoles considered in chapter 3. In this chapter the results of [289] are extended by using the using the MPT algorithm developed in chapter 3.2.2. The use of this algorithm allows us to determine the effect of domain wall catalysis beyond the

high temperature expansion used in [289] and determine the thermodynamic parameters which are relevant for the gravitational wave signal.

For parameter choices in the singlet-extended SM (xSM) which predict a first order EWPT, the model is often difficult to probe at the LHC. The $\mathbb{Z}_2$ symmetry prevents higgs-singlet mixing and for a singlet mass m_S which satisfies $m_S > m_h/2$ there is no corrections to higgs decays [282]. Bounds from phase transition dynamics are the only ways to probe the model in large regions of parameter space [284, 286], although the model generically predicts modified couplings which could be seen at future colliders [290]. Given the importance of this model for studies of electroweak baryogenesis [275, 280, 285] and dark matter [272, 273], an accurate determination of the phase transition dynamics in this model is important in order to reliably test these models. Most of the studies to date have focused on the homogeneous phase transition, however, if domain walls are present the transition rate will be greatly enhanced due to their catalysing effects.

The rest of this chapter is devoted to studying the effects of domain wall catalysis of the electroweak phase transition. In section 4.1 the details of the model are presented. In section 4.2 we present results for a representative choice of benchmark points and highlight how the dynamics of the transition is altered by the presence of domain walls. In section 4.3 we compare the gravitational wave signal in the catalysed transition to the homogeneous case.

4.1 Setup

In this section we review the singlet-extended SM (xSM) and discuss the general features of domain wall catalysed phase transitions in the model. In section 4.1.3 we also discuss the mountain pass algorithm and how we apply it to solving the tunnelling problem. The tree–level scalar potential is

$$V(h, S) = -\mu^2|\mathcal{H}|^2 + \lambda|\mathcal{H}|^4 - \frac{m^2}{2}S^2 + \frac{\eta}{4}S^4 + \kappa|\mathcal{H}|^2S^2, \tag{4.1}$$

where the Higgs doublet is such that $\langle\mathcal{H}\rangle = (0, h)/\sqrt{2}$, and in the regime of interest all parameters $(\eta, \lambda, \kappa, \mu^2, m^2)$ are positive. We introduce the following counterterms in the potential,

$$V_{\rm ct} = \mu^2_{\rm ct}|\mathcal{H}|^2 + \lambda_{\rm ct}|\mathcal{H}|^4 + m^2_{\rm ct}S^2 + \eta_{\rm ct}S^4, \tag{4.2}$$

which are fixed by the requirement that at $T = 0$ the Higgs mass, the Higgs vev and the singlet mass are unchanged from their tree–level values in the global minimum $(h, S) = (v, 0)$, and that the vev of S in the false vacuum $(h, S) = (0, v_s)$ is the same as at tree level. The renormalization scale used in the one–loop Coleman–Weinberg potential [33],

$$V_{\rm CW}(h,S) = \sum_{i=h,S} \frac{m_i^4(h,S)}{64\pi^2}\left(\log\left(\frac{m_i^2(h,S)}{\mu_0^2}\right) - \frac{3}{2}\right) \tag{4.3}$$

is taken to be $\mu_0 = 246\,\text{GeV}$.

In this chapter we include thermal corrections within the truncated full dressing scheme (see [35] for other possible schemes and related uncertainties). This amounts to substitute thermal masses obtained at leading order in the high temperature expansion in the one–loop effective potential,

$$m_i^2 \to m_i^2 + \Pi_i(T^2). \tag{4.4}$$

where

$$\begin{aligned} \Pi_h(T^2) &= c_h T^2 \qquad & c_h &= \frac{2m_W^2 + m_Z^2 + m_h^2 + 2m_t^2}{4v^2} + \frac{\kappa}{12} \\ \Pi_S(T^2) &= c_s T^2 \qquad & c_s &= \frac{4\kappa + 3\eta}{12} \end{aligned} \tag{4.5}$$

Adopting this scheme, the 1-loop thermal corrections to the potential are given by:

$$V_T(h,S;T) = \sum_{i=h,S} \frac{T^4}{2\pi^2} J_B\left(\frac{m_i^2(h,S) + \Pi_i(T^2)}{T^2}\right), \tag{4.6}$$

$$J_B(y^2) = \int_0^\infty dx\, x^2 \log\left[1 - \exp\left(-\sqrt{x^2 - y^2}\right)\right]. \tag{4.7}$$

The full thermal potential we use in our calculations is therefore:

$$V_{\rm eff}(h,S;T) = V(h,S) + V_{\rm CW}(h,S) + V_T(h,S;T) \tag{4.8}$$

after subtracting counterterms and making the substitution (4.4) in the thermal integral.

In the high-temperature limit the leading order corrections to the effective potential are

$$V_{\text{high-T}}(h,S;T) = \frac{c_h T^2 - \mu^2}{2} h^2 + \frac{\lambda}{4} h^4 + \frac{c_s T^2 - m^2}{2} S^2 + \frac{\eta}{4} S^4 + \frac{\kappa}{2} h^2 S^2 . \tag{4.9}$$

Keeping only the leading temperature corrections is not in general a valid approximation, but simplifies the discussion and allows some of the calculations to be done analytically, simplifying the discussion below.

4.1.1 Thermal History of the xSM

With the effective thermal potential $V_{\rm eff}(h, S; T)$ at hand we can study the thermal history of the xSM. The regime we are interested in is where the electroweak phase transition is two step:

$$(h, S) = (0, 0) \to (0, v_s) \to (v, 0)\,, \tag{4.10}$$

which occurs for parameters such that

$$\frac{m^2}{c_s} \gtrsim \frac{\mu^2}{c_h}\,. \tag{4.11}$$

Due to the spontaneous $\mathbb{Z}_2$ symmetry breaking in the first step, domain walls will be formed through the Kibble mechanism. In the high temperature limit, the domain wall solution can be obtained exactly:

$$S_{\rm DW}(z) = \frac{m(T)}{\sqrt{\eta}} \tanh\left(\frac{m(T) z}{\sqrt{2}}\right), \qquad m(T) = \sqrt{m^2 - c_s T^2}\,. \tag{4.12}$$

However, away from this limit we need to determine the domain wall shape numerically by finding a solution to

$$S''(z) = \frac{\partial}{\partial S} V_{\rm eff}(0, S; T), \quad S(\pm\infty) = \pm v_s(T), \tag{4.13}$$

where we have indicated by $v_s(T)$ the temperature dependent singlet vev, and we have taken $h \equiv 0$ according to the false vacuum configuration $(0, v_s)$.

The solution to (4.13) can be efficiently obtained by using the following first integral of the motion,

$$I = -\frac{1}{2} S'(z)^2 + V_{\rm eff}(0, S; T) = V_{\rm eff}(0, v_s; T) \tag{4.14}$$

which fixes the value of $S'(0) = \sqrt{2(V_{\rm eff}(0, 0; T) - V_{\rm eff}(0, v_s; T))}$, where we have used the fact that $S(0) = 0$ as the domain wall is odd for $z \to -z$. The soliton solution can then be simply obtained with the help of `Mathematica` by solving (4.13) with the above initial conditions for $S(0)$ and $S'(0)$, avoiding the need for a shooting/relaxation algorithm.

If the $\mathbb{Z}_2$ symmetry is exact the domain walls are exactly stable T_c and so will be present at the second phase transition. However, if there are explicit $\mathbb{Z}_2$ breaking terms in the

potential then the $S = \pm v_s$ vacua will no longer be degenerate. This introduces a pressure on the domain walls that causes them to expand and collide, leaving the true minimum state behind [131, 291]. As was shown in ref. [289] if the $\mathbb{Z}_2$ breaking comes from a Planck-suppressed dimension-5 operator cS^5/M_P, the domain walls will annihilate at a temperature

$$T_{\rm ann} \sim \frac{v_s}{2} \frac{c^{1/2}}{\xi^{1/2}\eta^{1/4}}\,, \tag{4.15}$$

where ξ is the mean separation between domain walls (in hubble units). We therefore see that for $\mathbb{Z}_2$ breaking due to gravity the symmetry can generically be of sufficient quality for domain walls to be long-lived enough to remain present at the electroweak phase transition.

4.1.2 False vacuum decay channels

When the temperature drops below the critical temperature T_c, the $(v, 0)$ vacuum becomes the global minimum and tunnelling can take place from the false vacuum $(0, v_s)$. Far from the domain walls, the nucleation rate can be found according to (euclidean) time independent and spherically symmetric solutions to the equations of motion [75, 76, 78],

$$\phi''(r) + \frac{2}{r}\phi'(r) = \frac{\partial}{\partial\phi} V_{\rm eff}(h, S; T), \tag{4.16}$$

with $\phi = h, S$, and boundary conditions $S(\infty) = |v_s(T)|$ (either sign of v_s would yield the same result), $h(\infty) = 0$, together with $S'(0) = 0$, $h'(0) = 0$. Here r indicates the radial coordinate of the spherical bubble. The equations (4.16) can be readily solved with the numerical methods implemented in `FindBounce` and `CosmoTransitions` [292]. After determining the tunnelling fields profiles, the nucleation rate per unit volume in the homogeneous false vacuum is given by

$$\Gamma_{\rm hom} \simeq T^4 e^{-B_{\rm hom}(T)}\,, \tag{4.17}$$

where $B_{\rm hom}(T)$ is the euclidean action evaluated on the field profiles satisfying the equations of motion (4.16)

$$B_{\rm hom}(T) = \frac{4\pi}{T} \int r^2 dr \left[\mathcal{L}_E[h, S] - \mathcal{L}_E[0, v_s(T)]\right]\,. \tag{4.18}$$

The presence of domain walls introduces an additional channel for vacuum decay. Bubbles of true vacuum can form centred on the domain wall with a significantly reduced

action compared to tunnelling from the homogeneous false vacuum [289]. This process is governed by field profiles $h(\rho, z)$ and $S(\rho, z)$ which satisfy

$$\frac{\partial^2\phi}{\partial\rho^2} + \frac{1}{\rho}\frac{\partial\phi}{\partial\rho} + \frac{\partial^2\phi}{\partial z^2} = \frac{\partial}{\partial\phi}V_{\text{eff}}(h, S; T), \tag{4.19}$$

with $\phi = h, S$ and boundary conditions

$$h(\infty, z) = h(\rho, \pm\infty) = 0, \quad S(\infty, z) = S_{\text{DW}}(z),\ S(\rho, \pm\infty) = \pm v_s, \tag{4.20}$$

where $S_{\text{DW}}(z)$ is the domain wall configuration obtained by solving (4.13). Here $\rho = \sqrt{x^2 + y^2}$ is the radial coordinate on the domain wall plane, and z indicates the orthogonal direction. In this case the bounce action is similarly given by the euclidean action evaluated on the solutions to equations (4.19) & (4.20)

$$B_{\text{DW}}(T) = \frac{2\pi}{T}\int \rho d\rho dz \left[\mathcal{L}_E[h, S] - \mathcal{L}_E[0, S_{\text{DW}}(z)]\right] . \tag{4.21}$$

The nucleation rate per unit surface for bubbles nucleated on domain walls is estimated as

$$\Gamma_{\text{DW}} \simeq \sigma_{\text{DW}} e^{-B_{\text{DW}}(T)} \tag{4.22}$$

where $\sigma_{\text{DW}} \sim v_s^3$ is the domain wall tension.

Solving the system in (4.19) directly is challenging as the spherical symmetry in equation (4.16) is broken by the presence of the domain wall. In Ref. [289], this issue was circumvented by employing a Kaluza–Klein decomposition along the z direction and reducing the 4d (euclidean) action to a 3d EFT written in terms of the KK modes. This reduces the problem to that of homogeneous tunnelling within the lower dimensional theory on the domain wall, which can be solved with standard techniques similar to the spherical case of (4.16) with the help of `CosmoTransitions`. However, this method becomes technically more difficult to apply beyond the high temperature approximation as there is no exact form for the domain wall profile or the KK modes. In addition, the effective theory on the domain wall may not be under control in the whole temperature range relevant for the tunneling.

4.1.3 Numerical Procedure

In order to determine the phase transition dynamics beyond the high-temperature expansion we will here look for solutions of (4.19) by following the strategy of Ref. [293]. The algorithm presented in [293] is based on the mountain pass theorem [264], which turns the issue of solving the PDE's into a minimization problem which can be more easily tackled numerically. The algorithm is initialized by constructing a path in field space that connects the false vacuum configuration to a supercritical configuration with a smaller euclidean action. In this case, the false vacuum is

$$S_{\rm fv}(\rho, z) = S_{\rm DW}(z), \quad h_{\rm fv}(\rho, z) \equiv 0\,. \tag{4.23}$$

and we use the following ansatz for the supercritical bubble:

$$S_{\rm scb}(\rho, z) = \frac{1}{2}\left[S_{\rm DW}(z + f(\rho/R_0)Z_0) + S_{\rm DW}(z - f(\rho/R_0)Z_0)\right] \tag{4.24}$$

$$h_{\rm scb}(\rho, z) = \frac{v_h}{2}\left[1 - \tanh\left(\frac{(\rho/R_0)^2 + (z/Z_0)^2 - 1}{\delta}\right)\right] \tag{4.25}$$

where R_0 sets the bubble radius in the r direction, Z_0 sets the radius in the z direction and δ sets the thickness of the higgs profile. The function $\rho(x)$ we take to be equal to

$$f(x) = 1 - \tanh\left(x^4\right) \tag{4.26}$$

for parameters in the thin wall regime (tunnelling close to the critical temperature), or $f(x) = e^{-x^2}$ at temperatures significantly below the critical temperature. In each case we vary the parameters R_0, Z_0, δ to find a profile which gives $S_{\rm scb} < S_{\rm fv}$.

We describe here the basic features of the mountain pass algorithm, but refer the reader to ref. [293] for more details. After determining the false vacuum and supercritical profiles we define a path in field space between the points $(h_{\rm fv}, S_{\rm fv})$ and $(h_{\rm scb}, S_{\rm scb})$. We find the profile along the path which maximises the action then update the profiles using a gradient descent algorithm to minimise a cost function. The cost function we choose is a measure of how well the equations of motion are satisfied:

$$C = \sum_{ij}\left(E[h(\rho_i, z_j)]^2 + E[S(\rho_i, z_j)]^2\right)\,, \tag{4.27}$$

$$E[\phi(\rho, z)] = \frac{\partial^2\phi}{\partial\rho^2} + \frac{1}{\rho}\frac{\partial\phi}{\partial\rho} + \frac{\partial^2\phi}{\partial z^2} - \frac{\partial}{\partial\phi}V_{\rm eff}(h, S; T)\,, \tag{4.28}$$

where the sum is over a grid of points (ρ_i, z_j). We note that this differs from the implementation of the algorithm in [293] where the cost function used was the action itself. C is evidently minimised for a solution to the equations of motion, but there are many solutions: the domain wall profile, the constant solutions $(h, S) = (v_h, 0)$ and $(h, S) = (0, v_s)$, the homogeneous tunnelling solution and the domain wall bounce solution we are interested in. The use of the mountain pass algorithm ensures that we find the domain wall bounce solution.

4.2 Homogeneous vs. Seeded - phase transition parameters

In this section we highlight the effect of catalysis by domain walls on a first order phase transition. We begin by discussing the bounce action as a function of temperature for both cases in the xSM for two choices of parameters. We then discuss the effect of domain wall catalysis on the thermodynamic quantities which describe the phase transition.

4.2.1 Benchmark Points and bounce action

The two benchmark cases we consider are for different values of the quartic coupling, η, with fixed portal coupling, κ, and singlet mass, m_S. Benchmark 1 is the following choice of parameters:

$$(\kappa, \eta, m_S) = (1.5,\, 3.3,\, 250\,\text{GeV})\,, \tag{4.29}$$

and benchmark 2 is the choice:

$$(\kappa, \eta, m_S) = (1.5,\, 2.3,\, 250\,\text{GeV})\,. \tag{4.30}$$

To calculate the catalysed bounce action we use the MPT algorithm discussed in Sec. 4.1, with a numerical solution for the full 1-loop potential V_{eff} of equation (4.8). Our results for the bounce action as a function of temperature are shown in figure 4.1 and also compare to a thin wall approximation for the catalysed transition. For benchmark 2 the homogeneous bounce action is not shown because the values are $B_{\text{hom}} \sim 800$, far above the value required for the phase transition to complete.

Also shown in figure 4.1 are the nucleation conditions for the seeded and homogeneous transitions during radiation domination. In both cases, this condition identifies the

temperature at which there is on average one bubble of true vacuum per Hubble patch. For a homogeneous phase transition, the nucleation temperature $T_{\rm n}$ is defined as

$$\mathcal{N}(T_{\rm n}) = \int_{T_{\rm n}}^{T_c} dT \, \frac{\Gamma_{\rm hom}(T)}{T H^4(T)} = 1, \tag{4.31}$$

with $\Gamma_{\rm hom}$ given in Eq. (4.17). For the present case of a phase transition at the electroweak scale, one finds $B_{\rm hom} \simeq 140$ as the nucleation condition.

For a seeded phase transition the nucleation probability depends on the nucleation rate $\Gamma_{\rm DW}$ in Eq. (4.22) and the average number of domain walls inside the Hubble patch, ξ. Typically $\xi \sim \mathcal{O}(1)$ if the domain wall network reaches the scaling regime, but can be much larger in the immediate aftermath of a second order phase transition. The condition in general reads

$$\mathcal{N}(T_{\rm n}) = \int_{T_{\rm n}}^{T_c} dT \, \frac{\xi \Gamma_{\rm DW}(T)}{T H^3(T)} = 1, \tag{4.32}$$

where $\xi H^{-2}(T)$ is the average domain wall surface in one Hubble patch. This results in $B_{\rm DW} \simeq 105$ at the electroweak scale for $\xi = 1$ (with a weak logarithmic dependence on ξ).

For both benchmark points, the catalysed bounce action is much smaller than the homogeneous bounce, $B_{\rm DW} < B_{\rm hom}$. Given the exponential dependence of the decay rate on the bounce action, at a given temperature the catalysed process will dominate the homogeneous decay

$$\Gamma_{\rm hom}(T) \ll \xi H(T) \Gamma_{\rm DW}(T) \, . \tag{4.33}$$

As the catalysed rate depends only linearly on the number of domain walls per hubble patch, ξ, this is the case even for a sparse domain wall network ($\xi \sim 1$).

The two benchmark points represent examples of the two types of effect domain wall catalysis can have on the phase transition. Benchmark 1 is a point where the homogenous transition only just completes ($\Gamma_{\rm hom}(T) = H^4(T)$ at the minimum of $B(T)$) but the catalysed transition is much faster. The presence of domain walls means $T_{\rm n}$ is much closer to the critical temperature than in the homogeneous case. Benchmark 2 is an example case where the homogeneous transition is too slow to complete (equation (4.31) is not satisfied) but the catalysed process does finish. This point in parameter space would be naively ruled out by the strongly suppressed phase transition, but is viable if domain walls are present.

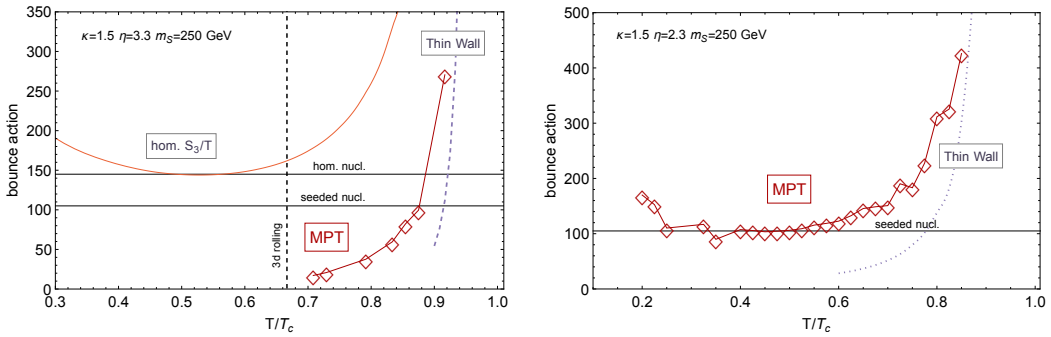

Figure 4.1: Homogenous vs. seeded bounce actions as a function of temperature for the benchmark points.

4.2.2 Phase transition parameters

In the case where the homogeneous phase transition does complete, we can define a characteristic timescale, β^{-1}, given by:

$$\beta = -\left.\frac{dB_{\rm hom}}{dt}\right|_{T_{\rm n}} = H_{\rm n} T_{\rm n} \left.\frac{dB_{\rm hom}}{dT}\right|_{T_{\rm n}}, \tag{4.34}$$

where $H_{\rm n} = H(T_{\rm n})$. In the homogeneous transition it is β^{-1} which sets the average time for two bubbles to collide after they are nucleated. For a catalysed transition, a similar timescale can be calculated with $B_{\rm DW}$ in place of $B_{\rm hom}$. However, for sparse domain wall networks ($\xi \sim 1$) the time taken for two bubbles to collide will instead be set by $(v_w \xi H_{\rm n})^{-1}$ where v_w is the bubble wall velocity. The effective inverse time scale for the catalysed phase transition will then be

$$\beta_{\rm DW} = \min\left(\left.\frac{dB_{\rm DW}}{dt}\right|_{T_{\rm n}}, v_w \xi H_{\rm n} \right). \tag{4.35}$$

Together with the time scale defined above, it is useful to define a percolation temperature, $T_{\rm p}$, that captures the moment at which a significant fraction of space is filled with the true vacuum and the transition is about to complete. For a 3D space, this fraction is approximately given by $p_c = 0.34$. Assuming a homogeneous nucleation probability per unit volume $\Gamma(t)$, the true vs false vacuum volume fraction at a given time t is given by [79]

$$I_{\rm 3D}(t) \equiv \frac{4\pi}{3} \int_{t_c}^{t} {\rm d}t' \Gamma(t') a(t')^3 r(t,t')^3, \tag{4.36}$$

so that T_p can be defined as $I_\mathrm{3D}(T_\mathrm{p}) = p_c$. In the expression above the (comoving) size at the time t of a bubble nucleated at t' is given by

$$r(t,t') = \int_{t'}^{t} \mathrm{d}\tilde{t} \frac{v_w}{a(\tilde{t})}. \tag{4.37}$$

For a homogeneous phase transition the percolation temperature can be evaluated straightforwardly according to (4.36) by taking $\Gamma(t) = \Gamma_\mathrm{hom}(t)$ in (4.17).

For a catalysed phase transition the percolation temperature depends on which of the two possibly time scales in Eq. (4.35) controls the transition. For a very dense network with $\xi \gg 1$, or a scenario in which the bounce action is flat around the nucleation temperature, we expect the time scale of the transition to be set by the slope of the (seeded) bounce action. This makes the percolation condition for this scenario equivalent to a homogeneous phase transition. The percolation temperature may then be computed according to (4.36) with the following identification:

$$\Gamma(t) = \xi H(t) \Gamma_\mathrm{DW}(t), \tag{4.38}$$

where $\Gamma_\mathrm{DW}(t)$ is given in (4.22). We shall indicate by T_p^3D the percolation temperature obtained in this way.

On the other hand, whenever the distance among domain walls sets the relevant time scale (namely for sparse networks with $\xi = \mathcal{O}(1)$ or for very fast nucleation rate) the percolation temperature can be derived from a purely geometrical argument, similarly to what has been done for a distribution of monopoles [81]. In this case bubbles of true vacuum can be thought of growing instantaneously out of the domain walls at $T \simeq T_\mathrm{n}$. From that moment on, the true vs false vacuum volume ratio is given by

$$I(t) \equiv \xi H(T_\mathrm{n}) \cdot 2 \int_{t_\mathrm{n}}^{t} v_w \frac{a(t_\mathrm{n})}{a(\tilde{t})} \, \mathrm{d}\tilde{t}, \tag{4.39}$$

and percolation occurs at $I(T_\mathrm{p}^\xi) = p_c$. In particular, assuming radiation domination, one finds

$$T_\mathrm{p}^\xi = \frac{1}{1 + \frac{p_c}{2\xi v_w}} T_\mathrm{n} \tag{4.40}$$

which for relativistic wall velocities and $\xi \sim 1$ gives $T_{\rm p}^{\xi=1} \sim 0.85\, T_{\rm n}$. According to the present discussion we shall therefore define the catalysed percolation temperature as

$$T_{\rm p} = \min(T_{\rm p}^{\rm 3D}, T_{\rm p}^{\xi}). \tag{4.41}$$

The timescale of the phase transition also sets the average size of bubbles at percolation, R_*. For homogeneous transition we shall refer to the standard relation

$$R_* = -v_w (8\pi)^{1/3} \left(\left. \frac{dB_{\rm hom}}{dt} \right|_{T_{\rm p}} \right)^{-1}. \tag{4.42}$$

According to our discussion around (4.38), the properties of a seeded phase transition whose time scale is set by the slope of the bounce action are indistinguishable from a homogeneous phase transition. The average bubble size is then still given by (4.42) with $B_{\rm hom}$ replaced by $B_{\rm DW}$:

$$R_* = -v_w (8\pi)^{1/3} \left(\left. \frac{dB_{\rm DW}}{dt} \right|_{T_{\rm p}} \right)^{-1}. \tag{4.43}$$

For sparse networks, however, the bubble size is related to the average distance among the walls as

$$R_* = a(t_{\rm n}) r(t_{\rm p}, t_{\rm n}) = \frac{p_c}{2\xi H(T_{\rm n})}, \tag{4.44}$$

where in the last step we have used the percolation condition $I(T_{\rm p}^{\xi}) = p_c$. This connection between the correlation length of the domain wall network, here given by $\xi_{\rm DW} = (\xi H)^{-1}$, and the effective size of the bubbles was also observed in the numerical simulation of Ref. [294]. In this work it was shown that the sound wave contribution to the gravitational wave signal could be obtained within a $\mathcal{O}(1)$ factor by replacing the standard parameter β with $1/\xi_{\rm DW}$. The appropriate value of R_* for the catalysed phase transition is the largest of (4.43) and (4.44).

Another important quantity that characterizes the transition is the energy released in the plasma, normalized to the radiation energy density at $T_{\rm p}$. This quantity is usually denoted by α and is given by (see e.g. [295])

$$\alpha = \frac{1}{\rho_{\rm rad}(T_{\rm p})} \left(\Delta V - \frac{1}{4} \frac{{\rm d}\Delta V}{{\rm d}T} \right) \Bigg|_{T=T_{\rm p}}, \tag{4.45}$$

where ΔV is the difference in energy between the true and false vacua at $T = T_{\rm p}$. The relation in (4.45) applies both to homogenous and catalysed phase transitions. For a dense domain wall network ($\xi \gg 1$) the catalysed transition will nucleate closer to the critical temperature due to the enhanced nucleation rate. For a given choice of parameters the energy released α and the size of colliding bubbles will be smaller than in the homogeneous transition.

4.2.3 Evolution of the bubble shape

Critical bubbles are nucleated with a disk–like shape due to the presence of the domain wall. It is then relevant to determine whether this shape is maintained during the subsequent expansion, or if instead bubbles tend to become spherical. A disk–like evolution requires that the size of the bubble along the direction orthogonal to the wall increases with a different velocity with respect to the size on the domain wall plane, otherwise the initial asymmetry would soon be erased. From this observation one can already conclude that in the absence of friction from the thermal plasma bubbles will become spherical as the wall velocity will everywhere reach the speed of light. Therefore, runaway bubbles will necessarily lose their initial non–spherical shape.

Let us now discuss the case in which friction implies a terminal velocity for the bubble wall, which could in principle be different in the orthogonal and parallel directions. The reason for this may be understood in terms of the energy that the bubble gains during the expansion: an increase of the bubble size along the domain wall plane comes with an additional gain from eating up the domain wall surface with respect to the orthogonal expansion, which is only fuelled by the energy difference between the false and true vacuum (vacuum pressure). However, the relative importance of the vacuum pressure with respect to the domain wall tension increases with the size of the bubble because of its volume–like scaling. To provide an estimate of this effect, let us consider an approximately spherical bubble of radius R, and let us indicate by ϵ the vacuum pressure and by σ and $\sigma_{\rm DW}$ the bubble and the domain wall tension, respectively. The energy gain when increasing from R to $R + {\rm d}R$ is then

$$\frac{{\rm d}E}{{\rm d}R} = -4\pi R^2 \epsilon + 8\pi R \left(\sigma - \frac{1}{4}\sigma_{\rm DW}\right) = -4\pi R^2 \epsilon \left(1 - \frac{R_c}{R}\right), \tag{4.46}$$

where $R_c = 2(\sigma - \sigma_{\rm DW}/4)/\epsilon$ is the critical radius. The only force that can unbalance the orthogonal vs parallel motion of the wall is the one proportional to $\sigma_{\rm DW}$, which is contained in R_c. Its relative importance with respect to the vacuum pressure scales as R_c/R, implying that once the overall size of the bubble has grown to be $R \gg R_c$ its motion is insensitive to the domain wall tension, and thus it is expected to be spherically symmetric. In fact, already when the size of the bubble has reached the would–be critical size in the absence of the domain wall, namely $R_c^{\rm hom} = 2\sigma/\epsilon$, the bubble can freely expand and we can again expect a minor impact of the domain wall tension.

On the other hand, as long as $R_c/R \sim 1$ the presence of the domain wall is crucial for the expansion of the bubble, implying a (short) period of non–spherical evolution.

4.3 Homogeneous vs. Seeded - Gravitational Wave Signal

The key parameters in determining the gravitational wave signal from a phase transition are the inverse timescale (β), the latent heat (α) and the bubble wall velocity (v_w). The influence of domain wall catalysis on β and α was discussed in section 4.2.2. The wall velocity is determined by balancing the latent heat driving the expansion of the bubble with the friction which comes from interactions of the wall with the thermal plasma [112]. The effect of domain wall catalysis doesn't change the friction on the wall, so the only difference in v_w from domain wall catalysis is due to the difference in α.

For the case of the electroweak phase transition, v_w will reach a terminal value due to transition radiation emitted as the W, Z bosons cross the bubble wall [113]. The main contribution to the gravitational wave comes from sound waves in the plasma. The peak frequency of the signal is set by the combination $H_{\rm p}R_*$, which is determined by β through equations (4.42) for the homogenous transition and equation (4.43) or (4.44) for the catalysed transition, depending on the domain wall network. The amplitude of the signal depends also on $H_{\rm p}R_*$ as well as the latent heat α.

In terms of these quantities the gravitational wave amplitude and peak frequency

today ($f_{p,0}$) are given by [102, 119–121]

$$\begin{aligned}\frac{d\Omega_{\rm gw\,,0}}{d\ln(f)} &= 4.13\times10^{-7}\,(H_{\rm p}R_*)\left(\frac{\kappa_{\rm sw}\alpha}{1+\alpha}\right)^2\left(\frac{100}{g_*}\right)^{1/3} S(f/f_{p,0})\,,\\ f_{p,0} &\simeq 26\left(\frac{1}{H_{\rm p}R_*}\right)\left(\frac{T_{\rm p}}{100\,{\rm GeV}}\right)\left(\frac{g_*}{100}\right)^{1/6}\mu{\rm Hz}\,.\\ S(x) &= x^3\left(\frac{7}{4+3x^2}\right)^{7/2}\end{aligned} \tag{4.47}$$

The factor $K = \kappa_{\rm sw}\alpha/(1+\alpha)$ is the kinetic energy fraction of the fluid. It depends on the velocity profile of the fluid and is given by [296]

$$K = \frac{4}{3}\bar{U}_f^2, \quad \bar{U}_f^2 = \frac{3}{v_w^3}\int_{c_s}^{v_w}\xi^2\frac{v^2}{1-v^2}d\xi\,. \tag{4.48}$$

The velocity profile $v(\xi)$ is the solution of [297]

$$\frac{2v}{\xi} = \frac{1-\xi v}{1-v^2}\left(\frac{1}{c_s^2}\frac{\xi-v}{1-\xi v^2}-1\right)\frac{dv}{d\xi} \tag{4.49}$$

with the boundary condition

$$v(v_w) = \frac{3\alpha}{2+3\alpha}. \tag{4.50}$$

Equation (4.50) is only true for relativistic wall velocities, $v_w \to 1$, which is the case for the examples we consider. The gravitational wave spectrum in (4.47) is accurate only when the time for shock formation is larger than one Hubble time, namely if

$$\frac{H_{\rm p}R_*}{\bar{U}_f} = H_{\rm p}R_*\sqrt{\frac{4(1+\alpha)}{3\kappa_{\rm sw}\alpha}} > 1. \tag{4.51}$$

When this inequality is not satisfied, Eq. (4.47) needs to include an additional suppression factor given $H_*R_*/\bar{U}_f$ [122].

4.3.1 Results

To compare the signal from a catalysed transition with the homogeneous transition we consider the case where $\eta = 1, m_S = 200$ GeV and vary the portal coupling κ. The results were obtained using a thin wall approximation to the catalysed transition rate, the results of which were verified using the MPT algorithm for representative κ values.

The nucleation and percolation temperatures for the phase transition as a function of κ are shown in the left panel of figure 4.2. The homogeneous phase transition fails

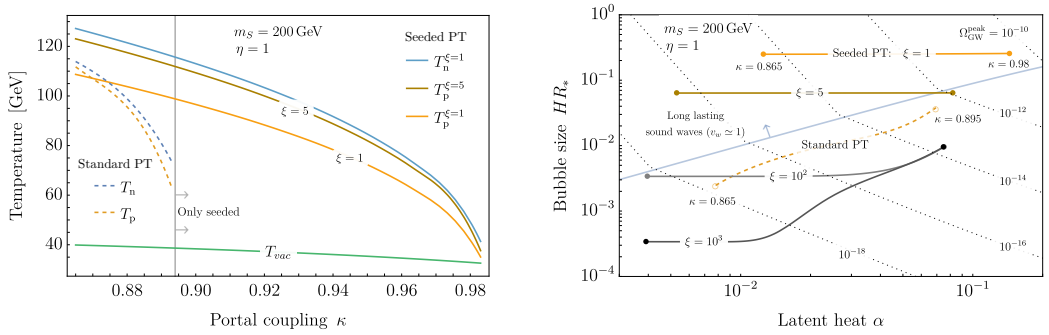

Figure 4.2: Left panel shows the nucleation and percolation temperatures for the both the homogeneous and catalysed transitions for varying portal couplings and $\eta = 1, m_S = 200$ GeV. The right panel shows the latent heat (α) and bubble size (HR_*) for the homogeneous transition (dashed line) and catalysed transitions (solid lines) for different ξ values. Moving left to right along any of the curves corresponds to increasing κ. The range of κ values for the homogeneous transition is $0.865 \leq \kappa \leq 0.895$ and $0.865 \leq \kappa \leq 0.983$ for the catalysed transitions.

to complete for $\kappa \gtrsim 0.9$, while the catalysed transition completes up to $\kappa \sim 0.98$. For the homogeneous transition the nucleation and percolation temperatures are always close together, however, for $\xi \sim 1$ the two temperatures are distinct. This is only true for very small ξ, already for $\xi = 5$ we can see that this effect is negligible.

The right panel of figure 4.2 shows the bubble size $H_p R_*$ and α for both the homogenous transition (dashed line) and the catalysed transition for different values of ξ (solid lines). These results highlight some of the features mentioned in section 4.2. For the homogeneous transition, $H_p R_*$ and α both increase as the transition becomes more strongly supercooled. This behaviour is also seen for the catalysed transition at large ξ values, where $H_p R_*$ is set by the bounce action. For $\xi = 1, 5$ the bubble size is determined by the domain wall separation and is therefore independent of α, as indicated by the straight lines in figure 4.2.

The contours of constant gravitational wave amplitude are shown as dotted lines in figure 4.2. Below the blue line equation (4.51) is not satisfied and the overall amplitude comes with an additional suppression factor, which leads to the different gradients above and below the line. For the homogeneous transition this condition is not satisfied for any of the points, as (4.51) is difficult to satisfy because $H_p R_*$ and α both increase as the transition becomes supercooled [122]. For a sparse domain wall network the bubbles are always expected to be hubble scale, making this condition is easier to satisfy. Combined with the fact that the catalysed transition allows the phase transition to complete at

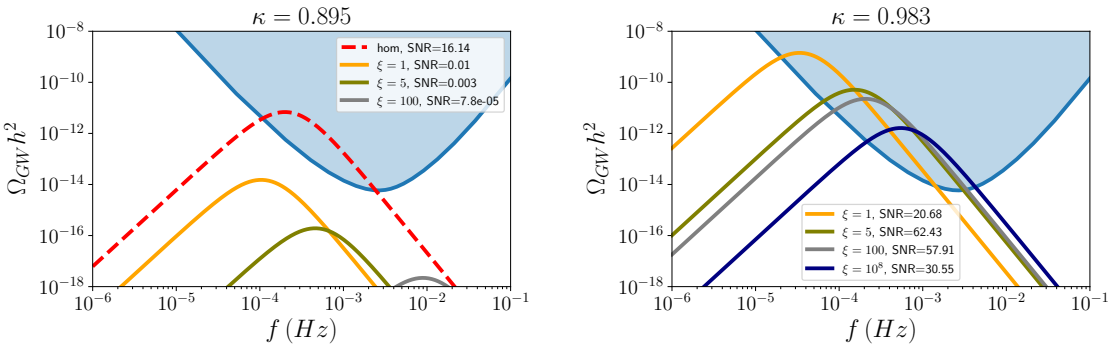

Figure 4.3: Figures showing the gravitational wave signal for $\kappa = 0.895$ (left) and $\kappa = 0.975$ (right). The orange curve, green, grey and blue curves show the catalysed transition for $\xi = 1, 5, 100, 10^8$ respectively. The red dashed curve shows the homogeneous transition, which only completes for $\kappa = 0.895$. Blue shaded region shows the LISA sensitivity [10].

larger κ values means that domain wall catalysis could lead to a large gravitational wave signal that can't be achieved in a homogeneous transition.

In the limiting case where $\xi = 1$ it is also possible that there is a mixed phase transition where both the bubbles nucleated on the domain walls and in the homogeneous vacuum are relevant. Bubbles are first nucleated on the domain walls, but before they can meet and collide bubbles nucleated from the homogeneous vacuum are nucleated and percolate. In this case $T_{\rm n}$ is set by the catalysed rate, but $T_{\rm p}$ comes from the homogeneous transition. Examples of this are the points for $\kappa \sim 0.88$ shown on the left plot of figure 4.2, where $T_{\rm p}^{\xi=1}$ is below the nucleation temperature for the homogeneous transition.

A comparison of the gravitational wave signal from each type of phase transition is shown in figure 4.3. The power-law integrated sensitivity curves for LISA are shown in blue, computed using the procedure outlined in ref. [298] for a signal to noise ratio (SNR) of 1. The left panel shows the spectra for $\kappa = 0.895$, which is the largest κ value where the homogeneous transition still completes. In this case the expected signal form a homogeneous transition is larger than the catalysed transitions for all choices of ξ. This is because the catalysed transition percolates closer to the critical temperature, leading to less energy being released in the transition. The signal from a catalysed transition is larger for smaller ξ values as the bubbles are larger at percolation. The $\xi = 10^8$ transition is not shown as the signal is negligible.

The right panel shows the signal for the catalysed transition at $\kappa = 0.983$, in the regime where the homogeneous transition does not finish. The signal for larger ξ values is larger and peaked at lower frequencies. For the $\xi = 100, 10^8$ transitions the bubble size is no longer set by the domain wall separation. The suppression of the signal at larger ξ in this case then comes from the faster transition rate due to the number of domain walls being larger.

Chapter 5

Conclusions

This thesis has focused on phase transitions in the early universe and some of their implications on early universe cosmology. The SM has a rich phase structure and undergoes two phase transitions in the early universe, while many BSM theories predict new phase transitions at high temperatures. These phase transitions could lead to gravitational wave signals in the coming years, which could provide the first experimental probe of the very early stages of the universe.

The focus of chapter 2 was the confining transition in the Randall Sundrum model, which in its basic form leads to eternal inflation, making it inconsistent with cosmological observations. The model is described at high temperature by an AdS black hole, with a transition to the RS phase proceeding via a first order phase transition which is exponentially suppressed by the large number N^2. The work of chapter 2 showed that this situation can be avoided by introducing new scalars which generate a potential that stabilises the IR brane at high temperatures, a mechanism we term avoided deconfinement. Provided the universe exits inflation in the RS phase, it remains there, never entering the BH phase.

There are also various phenomenological applications of this mechanism which were touched on. Avoided deconfinement changes the cosmological history in a unique way, where from the IR brane point of view it is effectively a model with a low reheat temperature, but from the UV brane point of view the temperature can be arbitrarily high. This allows the possibility that the electroweak and/or QCD phase transitions happen at very high temperatures. Furthermore, the AD model can lead to the production of dark matter in the $10 - 100$ TeV range with $\mathcal{O}(1)$ couplings to the SM. This scenario is difficult to

achieve in a standard cosmology, but becomes a viable expectation in the AD model due to the temperature dependence of the DM mass.

In chapters 3 and 4 the possibility that phase transitions could be catalysed by the presence of topological defects was considered. Most phase transitions are catalysed by defects or boundary effects in some way, so a natural question to ask whether cosmological transitions could be catalysed in a similar manner. When defects are present to catalyse the transition the bubble nucleation rate can be enhanced by many orders of magnitude. Given the importance of the rate for the phenomenological consequences of the transition, such as the degree of supercooling and the gravitational wave signal, catalysing effects can greatly influence the features of a phase transition.

The case where the catalysing defects are metastable magnetic monopoles was discussed in chapter 3. It was shown that the transition rate can be enhanced by many orders of magnitude by a population of monopoles acting to catalyse the phase transition. The requirement for monopoles to be metastable is that the field values at the monopole core are close to the true vacuum of the potential. These monopoles may be produced via the Kibble mechanism in a two-step phase transition, in high energy particle collisions or be emitted during black hole evaporation. In the presence of these defects the phase transition rate can be exponentially enhanced, and the expected gravitational wave signal caused by the phase transition may also be significantly modified. This may also have implications for the stability of the vacuum if some population of monopoles exists in the current universe.

In chapter 3 an algorithm was developed to find the saddle point solutions describing the transition. In chapter 4 this algorithm was applied to calculate the catalysing effects of domain walls on the electroweak phase transition, allowing the expected gravitational wave signal to be determined. The signal can be significantly altered due to the presence of domain walls, particularly in the case of a sparse domain wall network. In the catalysed transition the bubbles can be much larger when they collide, which shifts the peak frequency and increases the amplitude of the signal. The faster transition rate also means that parameter space which was previously thought to be ruled out by supercooling arguments become viable in the presence of domain walls.

Appendix A

Discretisation

While our discussion of the procedure in section 3.2.2 considered the functions h_α^n, u_α^n to be continuous in each of the variables τ, s and α, in order to implement the MPT algorithm it is necessary to discretise the problem. To do this, we first construct a lattice of points (s_i, τ_j, α_k), where we take the points s_i to be logarithmically spaced. The points were chosen to be in the intervals

$$10^{-2} \leq s \leq 2S, \quad 0 \leq \tau \leq 4T, \quad 0 \leq \alpha \leq 1, \tag{A.1}$$

for T, S taken from the super-critical solution given in equation (3.25). The functions are then written as tensors h_{ijk}, u_{ijk} such that

$$h_{ijk} = h_{\alpha_k}(\tau_j, s_i), \qquad u_{ijk} = u_{\alpha_k}(\tau_j, s_i). \tag{A.2}$$

In the discretised theory the Euclidean action becomes

$$\begin{aligned} S_E[h_{ijk}, u_{ijk}] = &\frac{4\pi}{g^2} \sum_{ij} s_i^2 ds_i d\tau \left\{ \frac{1}{2} \left(\dot{h}_{ijk}^2 + {h'}_{ijk}^2 \right) + \frac{1}{g^2} \left(\dot{u}_{ijk}^2 + {u'}_{ijk}^2 \right) \right. \\ &\left. + \frac{h_{ijk}^2 u_{ijk}^2}{s^2} + \frac{1}{2} \left(u_{ijk}^2 - 1 \right)^2 + \frac{\lambda}{g^2} V_h(h_{ijk}) \right\}, \end{aligned} \tag{A.3}$$

where $d\tau$ is the lattice spacing in the τ direction and ds_i the lattice spacing in s, which we note has an index because the lattice in the s-direction is logarithmically spaced. The derivatives are approximated as finite differences and we use the boundary conditions to compute the derivatives at the endpoints. For example, approximating $\dot{h}_{ijk}$ as a finite difference at a given point (τ_j, s_i) gives

$$\dot{h}_{ijk} = \frac{h_{i,j+1,k} - h_{i,j-1,k}}{2d\tau}. \tag{A.4}$$

At the endpoint (j such that $\tau_j = 4T$) we let $h_{i,j+1,k} = h_m(s_i)$, enforcing the boundary condition $h(\tau, s) \to h_m(s)$ at large τ. For the boundary condition at $\tau = 0$ we use the reflection symmetry $\tau \to -\tau$, at large s we require that $h \to 1, u \to 0$ and at small s we use a Taylor expansion.

The discretised action is used to calculate equation (3.26) for each value of k and determine the value $\bar{k}$ for which $I^n_{\alpha_{\bar{k}}}$ is a maximum at a given step n. The discretised form of equations (3.29) is then

$$\left(\frac{\delta \bar{I}}{\delta h^n_{\bar{\alpha}}}\right)_{ij} = -\frac{8\pi s_i^2}{g^2}\left(\ddot{h}_{ij\bar{k}} + h''_{ij\bar{k}} + \frac{2}{s_i}h'_{ij\bar{k}} - \frac{2h_{ij\bar{k}}u^2_{ij\bar{k}}}{s_i^2} - \lambda V'_h(h_{ij\bar{k}})\right), \tag{A.5}$$

$$\left(\frac{\delta \bar{I}}{\delta u^n_{\bar{\alpha}}}\right)_{ij} = -\frac{16\pi}{g^2}\left(\ddot{u}_{ij\bar{k}} + u''_{ij\bar{k}} - \frac{u_{ij\bar{k}}(u^2_{ij\bar{k}} - 1)}{s_i^2} - h^2_{ij\bar{k}}u_{ij\bar{k}}\right), \tag{A.6}$$

where derivatives are again approximated using finite difference methods as described above. The profiles are then updated according to the gradient descent algorithm as in equation (3.28)

$$\begin{aligned} h^{n+1}_{ijk} &= h^n_{ijk} - \beta_n F(\alpha_k, \alpha_{\bar{k}})\left(\frac{\delta \bar{I}}{\delta h^n_{\bar{\alpha}}}\right)_{ij}, \\ u^{n+1}_{ijk} &= u^n_{ijk} - \beta_n F(\alpha_k, \alpha_{\bar{k}})\left(\frac{\delta \bar{I}}{\delta u^n_{\bar{\alpha}}}\right)_{ij}. \end{aligned} \tag{A.7}$$

The step size β_n we choose depends on the value of $\bar{k}$ which maximises $I^n_{\alpha_k}$ and whether the value found at step n differs from the value at the previous step $n-1$. To calculate the step size we let $\vec{X}^n_k$ be the vector constructed from combining the components of (h^n_{ijk}, u^n_{ijk}) and $\delta\vec{X}^n_k = \vec{X}^n_k - \vec{X}^{n-1}_k$.The step size we use is [299]

$$\beta_n = \frac{\left|\left(\vec{X}^n_{\bar{k}} - \vec{X}^{n-1}_{\bar{k}}\right).\left(\delta\vec{X}^n_{\bar{k}} - \delta\vec{X}^{n-1}_{\bar{k}}\right)\right|}{\left\|\delta\vec{X}^n_{\bar{k}} - \delta\vec{X}^{n-1}_{\bar{k}}\right\|}. \tag{A.8}$$

Bibliography

[1] J. C. Pati and A. Salam, *Lepton Number as the Fourth Color*, *Phys. Rev. D* **10** (1974) 275.

[2] H. Georgi and S. L. Glashow, *Unity of All Elementary Particle Forces*, *Phys. Rev. Lett.* **32** (1974) 438.

[3] H. Fritzsch and P. Minkowski, *Unified Interactions of Leptons and Hadrons*, *Annals Phys.* **93** (1975) 193.

[4] R. D. Peccei and H. R. Quinn, *CP Conservation in the Presence of Instantons*, *Phys. Rev. Lett.* **38** (1977) 1440.

[5] R. D. Peccei and H. R. Quinn, *Constraints Imposed by CP Conservation in the Presence of Instantons*, *Phys. Rev. D* **16** (1977) 1791.

[6] V. A. Kuzmin, V. A. Rubakov and M. E. Shaposhnikov, *On the Anomalous Electroweak Baryon Number Nonconservation in the Early Universe*, *Phys. Lett. B* **155** (1985) 36.

[7] L. Randall and R. Sundrum, *A Large mass hierarchy from a small extra dimension*, *Phys. Rev. Lett.* **83** (1999) 3370 [hep-ph/9905221].

[8] P. Creminelli, A. Nicolis and R. Rattazzi, *Holography and the electroweak phase transition*, *JHEP* **03** (2002) 051 [hep-th/0107141].

[9] C. Caprini et al., *Science with the space-based interferometer eLISA. II: Gravitational waves from cosmological phase transitions*, *JCAP* **04** (2016) 001 [1512.06239].

[10] C. Caprini et al., *Detecting gravitational waves from cosmological phase transitions with LISA: an update*, *JCAP* **03** (2020) 024 [1910.13125].

[11] K. A. Intriligator and N. Seiberg, *Lectures on supersymmetric gauge theories and electric-magnetic duality*, *Nucl. Phys. B Proc. Suppl.* **45BC** (1996) 1 [hep-th/9509066].

[12] S. Weinberg, *A Model of Leptons*, *Phys. Rev. Lett.* **19** (1967) 1264.

[13] K. G. Wilson, *Confinement of Quarks*, *Phys. Rev. D* **10** (1974) 2445.

[14] A. M. Polyakov, *Compact Gauge Fields and the Infrared Catastrophe*, *Phys. Lett. B* **59** (1975) 82.

[15] G. 't Hooft, *Naturalness, chiral symmetry, and spontaneous chiral symmetry breaking*, *NATO Sci. Ser. B* **59** (1980) 135.

[16] D. A. Kirzhnits and A. D. Linde, *Macroscopic Consequences of the Weinberg Model*, *Phys. Lett. B* **42** (1972) 471.

[17] S. Weinberg, *Gauge and Global Symmetries at High Temperature*, *Phys. Rev. D* **9** (1974) 3357.

[18] L. Dolan and R. Jackiw, *Symmetry Behavior at Finite Temperature*, *Phys. Rev. D* **9** (1974) 3320.

[19] D. A. Kirzhnits and A. D. Linde, *Symmetry Behavior in Gauge Theories*, *Annals Phys.* **101** (1976) 195.

[20] Planck collaboration, *Planck 2018 results. I. Overview and the cosmological legacy of Planck*, *Astron. Astrophys.* **641** (2020) A1 [1807.06205].

[21] Planck collaboration, *Planck 2018 results. VII. Isotropy and Statistics of the CMB*, *Astron. Astrophys.* **641** (2020) A7 [1906.02552].

[22] Planck collaboration, *Planck 2018 results. VI. Cosmological parameters*, *Astron. Astrophys.* **641** (2020) A6 [1807.06209].

[23] A. H. Guth, *The Inflationary Universe: A Possible Solution to the Horizon and Flatness Problems*, *Phys. Rev. D* **23** (1981) 347.

[24] Planck collaboration, *Planck 2018 results. X. Constraints on inflation*, *Astron. Astrophys.* **641** (2020) A10 [1807.06211].

[25] F. L. Bezrukov and M. Shaposhnikov, *The Standard Model Higgs boson as the inflaton*, *Phys. Lett. B* **659** (2008) 703 [0710.3755].

[26] M. Persic, P. Salucci and F. Stel, *The Universal rotation curve of spiral galaxies: 1. The Dark matter connection*, *Mon. Not. Roy. Astron. Soc.* **281** (1996) 27 [astro-ph/9506004].

[27] D. Clowe, M. Bradac, A. H. Gonzalez, M. Markevitch, S. W. Randall, C. Jones et al., *A direct empirical proof of the existence of dark matter*, *Astrophys. J. Lett.* **648** (2006) L109 [astro-ph/0608407].

[28] A. D. Sakharov, *Violation of CP Invariance, C asymmetry, and baryon asymmetry of the universe*, *Pisma Zh. Eksp. Teor. Fiz.* **5** (1967) 32.

[29] V. A. Rubakov and M. E. Shaposhnikov, *Electroweak baryon number nonconservation in the early universe and in high-energy collisions*, *Usp. Fiz. Nauk* **166** (1996) 493 [hep-ph/9603208].

[30] M. E. Shaposhnikov, *Baryon Asymmetry of the Universe in Standard Electroweak Theory*, *Nucl. Phys. B* **287** (1987) 757.

[31] K. Kajantie, M. Laine, K. Rummukainen and M. E. Shaposhnikov, *Is there a hot electroweak phase transition at $m_H \gtrsim m_W$?*, *Phys. Rev. Lett.* **77** (1996) 2887 [hep-ph/9605288].

[32] Y. Aoki, G. Endrodi, Z. Fodor, S. D. Katz and K. K. Szabo, *The Order of the quantum chromodynamics transition predicted by the standard model of particle physics*, *Nature* **443** (2006) 675 [hep-lat/0611014].

[33] S. R. Coleman and E. J. Weinberg, *Radiative Corrections as the Origin of Spontaneous Symmetry Breaking*, *Phys. Rev. D* **7** (1973) 1888.

[34] C. Delaunay, C. Grojean and J. D. Wells, *Dynamics of Non-renormalizable Electroweak Symmetry Breaking*, *JHEP* **04** (2008) 029 [0711.2511].

[35] D. Curtin, P. Meade and H. Ramani, *Thermal Resummation and Phase Transitions*, *Eur. Phys. J. C* **78** (2018) 787 [1612.00466].

[36] K. Kajantie, M. Laine, K. Rummukainen and M. E. Shaposhnikov, *The Electroweak phase transition: A Nonperturbative analysis*, *Nucl. Phys. B* **466** (1996) 189 [hep-lat/9510020].

[37] F. Karsch, T. Neuhaus, A. Patkos and J. Rank, *Critical Higgs mass and temperature dependence of gauge boson masses in the SU(2) gauge Higgs model*, *Nucl. Phys. B Proc. Suppl.* **53** (1997) 623 [hep-lat/9608087].

[38] Y. Aoki, *Four-dimensional simulation of the hot electroweak phase transition with the SU(2) gauge Higgs model*, *Nucl. Phys. B Proc. Suppl.* **53** (1997) 609 [hep-lat/9608061].

[39] M. Gurtler, E.-M. Ilgenfritz and A. Schiller, *Where the electroweak phase transition ends*, *Phys. Rev. D* **56** (1997) 3888 [hep-lat/9704013].

[40] M. Laine and K. Rummukainen, *What's new with the electroweak phase transition?*, *Nucl. Phys. B Proc. Suppl.* **73** (1999) 180 [hep-lat/9809045].

[41] B. Svetitsky and L. G. Yaffe, *Critical Behavior at Finite Temperature Confinement Transitions*, *Nucl. Phys. B* **210** (1982) 423.

[42] R. D. Pisarski and F. Wilczek, *Remarks on the Chiral Phase Transition in Chromodynamics*, *Phys. Rev. D* **29** (1984) 338.

[43] H. H. Iacobson and D. J. Amit, *First Order Transitions Induced by Fluctuations in General ϕ^4 Theories*, *Annals Phys.* **133** (1981) 57.

[44] T. Bhattacharya et al., *QCD Phase Transition with Chiral Quarks and Physical Quark Masses*, *Phys. Rev. Lett.* **113** (2014) 082001 [1402.5175].

[45] G. 't Hooft, *A Planar Diagram Theory for Strong Interactions*, *Nucl. Phys. B* **72** (1974) 461.

[46] E. Witten, *Current Algebra Theorems for the U(1) Goldstone Boson*, *Nucl. Phys. B* **156** (1979) 269.

[47] M. Panero, *Thermodynamics of the QCD plasma and the large-N limit*, *Phys. Rev. Lett.* **103** (2009) 232001 [0907.3719].

[48] H. Meyer-Ortmanns, *Phase transitions in quantum chromodynamics*, *Rev. Mod. Phys.* **68** (1996) 473 [hep-lat/9608098].

[49] M. Pietroni, *The Electroweak phase transition in a nonminimal supersymmetric model*, *Nucl. Phys. B* **402** (1993) 27 [hep-ph/9207227].

[50] M. Carena, M. Quiros and C. E. M. Wagner, *Opening the window for electroweak baryogenesis*, *Phys. Lett. B* **380** (1996) 81 [hep-ph/9603420].

[51] D. Delepine, J. M. Gerard, R. Gonzalez Felipe and J. Weyers, *A Light stop and electroweak baryogenesis*, *Phys. Lett. B* **386** (1996) 183 [hep-ph/9604440].

[52] R. Apreda, M. Maggiore, A. Nicolis and A. Riotto, *Gravitational waves from electroweak phase transitions*, *Nucl. Phys. B* **631** (2002) 342 [gr-qc/0107033].

[53] S. J. Huber, T. Konstandin, G. Nardini and I. Rues, *Detectable Gravitational Waves from Very Strong Phase Transitions in the General NMSSM*, *JCAP* **03** (2016) 036 [1512.06357].

[54] E. Ponton, *TASI 2011: Four Lectures on TeV Scale Extra Dimensions*, in *Theoretical Advanced Study Institute in Elementary Particle Physics: The Dark Secrets of the Terascale*, pp. 283–374, 2013, DOI [1207.3827].

[55] J. M. Maldacena, *The Large N limit of superconformal field theories and supergravity*, *Adv. Theor. Math. Phys.* **2** (1998) 231 [hep-th/9711200].

[56] E. Witten, *Anti-de Sitter space and holography*, *Adv. Theor. Math. Phys.* **2** (1998) 253 [hep-th/9802150].

[57] S. S. Gubser, I. R. Klebanov and A. M. Polyakov, *Gauge theory correlators from noncritical string theory*, *Phys. Lett. B* **428** (1998) 105 [hep-th/9802109].

[58] E. Witten, *Anti-de Sitter space, thermal phase transition, and confinement in gauge theories*, *Adv. Theor. Math. Phys.* **2** (1998) 505 [hep-th/9803131].

[59] S. Kachru, R. Kallosh, A. D. Linde and S. P. Trivedi, *De Sitter vacua in string theory*, *Phys. Rev. D* **68** (2003) 046005 [hep-th/0301240].

[60] I. R. Klebanov and E. Witten, *Superconformal field theory on three-branes at a Calabi-Yau singularity*, *Nucl. Phys. B* **536** (1998) 199 [hep-th/9807080].

[61] I. R. Klebanov and A. A. Tseytlin, *Gravity duals of supersymmetric SU(N) x SU(N+M) gauge theories*, *Nucl. Phys. B* **578** (2000) 123 [hep-th/0002159].

[62] I. R. Klebanov and M. J. Strassler, *Supergravity and a confining gauge theory: Duality cascades and chi SB resolution of naked singularities*, *JHEP* **08** (2000) 052 [hep-th/0007191].

[63] L. Randall and R. Sundrum, *An Alternative to compactification*, *Phys. Rev. Lett.* **83** (1999) 4690 [hep-th/9906064].

[64] M. A. Luty and R. Sundrum, *Hierarchy stabilization in warped supersymmetry*, *Phys. Rev. D* **64** (2001) 065012 [hep-th/0012158].

[65] H. L. Verlinde, *Holography and compactification*, *Nucl. Phys. B* **580** (2000) 264 [hep-th/9906182].

[66] C. S. Chan, P. L. Paul and H. L. Verlinde, *A Note on warped string compactification*, *Nucl. Phys. B* **581** (2000) 156 [hep-th/0003236].

[67] F. Brummer, A. Hebecker and E. Trincherini, *The Throat as a Randall-Sundrum model with Goldberger-Wise stabilization*, *Nucl. Phys. B* **738** (2006) 283 [hep-th/0510113].

[68] L. Randall, *The Boundaries of KKLT*, *Fortsch. Phys.* **68** (2020) 1900105 [1912.06693].

[69] N. Arkani-Hamed, M. Porrati and L. Randall, *Holography and phenomenology*, *JHEP* **08** (2001) 017 [hep-th/0012148].

[70] R. Rattazzi and A. Zaffaroni, *Comments on the holographic picture of the Randall-Sundrum model*, *JHEP* **04** (2001) 021 [hep-th/0012248].

[71] S. S. Gubser, *AdS / CFT and gravity*, *Phys. Rev. D* **63** (2001) 084017 [hep-th/9912001].

[72] W. D. Goldberger and M. B. Wise, *Modulus stabilization with bulk fields*, *Phys. Rev. Lett.* **83** (1999) 4922 [hep-ph/9907447].

[73] S. W. Hawking and D. N. Page, *Thermodynamics of Black Holes in anti-De Sitter Space*, *Commun. Math. Phys.* **87** (1983) 577.

[74] J. S. Langer, *Statistical theory of the decay of metastable states*, *Annals Phys.* **54** (1969) 258.

[75] S. R. Coleman, *The Fate of the False Vacuum. 1. Semiclassical Theory*, *Phys. Rev. D* **15** (1977) 2929.

[76] C. G. Callan, Jr. and S. R. Coleman, *The Fate of the False Vacuum. 2. First Quantum Corrections*, *Phys. Rev. D* **16** (1977) 1762.

[77] S. R. Coleman, V. Glaser and A. Martin, *Action Minima Among Solutions to a Class of Euclidean Scalar Field Equations*, *Commun. Math. Phys.* **58** (1978) 211.

[78] A. D. Linde, *Decay of the False Vacuum at Finite Temperature*, *Nucl. Phys. B* **216** (1983) 421.

[79] A. H. Guth and E. J. Weinberg, *Could the Universe Have Recovered from a Slow First Order Phase Transition?*, *Nucl. Phys. B* **212** (1983) 321.

[80] A. H. Guth and E. J. Weinberg, *A Cosmological Lower Bound on the Higgs Boson Mass*, *Phys. Rev. Lett.* **45** (1980) 1131.

[81] A. H. Guth and E. J. Weinberg, *Cosmological Consequences of a First Order Phase Transition in the SU(5) Grand Unified Model*, *Phys. Rev. D* **23** (1981) 876.

[82] M. S. Turner, E. J. Weinberg and L. M. Widrow, *Bubble nucleation in first order inflation and other cosmological phase transitions*, *Phys. Rev. D* **46** (1992) 2384.

[83] LIGO Scientific, Virgo collaboration, *Binary Black Hole Mergers in the first Advanced LIGO Observing Run*, *Phys. Rev. X* **6** (2016) 041015 [1606.04856].

[84] N. Seto, S. Kawamura and T. Nakamura, *Possibility of direct measurement of the acceleration of the universe using 0.1-Hz band laser interferometer gravitational wave antenna in space*, *Phys. Rev. Lett.* **87** (2001) 221103 [astro-ph/0108011].

[85] KAGRA collaboration, *Detector configuration of KAGRA: The Japanese cryogenic gravitational-wave detector*, *Class. Quant. Grav.* **29** (2012) 124007 [1111.7185].

[86] B. Sathyaprakash et al., *Scientific Objectives of Einstein Telescope*, *Class. Quant. Grav.* **29** (2012) 124013 [1206.0331].

[87] C. S. Unnikrishnan, *IndIGO and LIGO-India: Scope and plans for gravitational wave research and precision metrology in India*, *Int. J. Mod. Phys. D* **22** (2013) 1341010 [1510.06059].

[88] LISA collaboration, *Laser Interferometer Space Antenna*, 1702.00786.

[89] MAGIS collaboration, *Mid-band gravitational wave detection with precision atomic sensors*, 1711.02225.

[90] B. Canuel et al., *Exploring gravity with the MIGA large scale atom interferometer*, *Sci. Rep.* **8** (2018) 14064 [1703.02490].

[91] S. Kawamura et al., *Space gravitational-wave antennas DECIGO and B-DECIGO*, *Int. J. Mod. Phys. D* **28** (2019) 1845001.

[92] MAGIS-100 collaboration, *Matter-wave Atomic Gradiometer InterferometricSensor (MAGIS-100) at Fermilab*, *PoS* **ICHEP2018** (2019) 021 [1812.00482].

[93] B. Canuel et al., *ELGAR—a European Laboratory for Gravitation and Atom-interferometric Research*, *Class. Quant. Grav.* **37** (2020) 225017 [1911.03701].

[94] AEDGE collaboration, *AEDGE: Atomic Experiment for Dark Matter and Gravity Exploration in Space*, *EPJ Quant. Technol.* **7** (2020) 6 [1908.00802].

[95] M.-S. Zhan et al., *ZAIGA: Zhaoshan Long-baseline Atom Interferometer Gravitation Antenna*, *Int. J. Mod. Phys. D* **29** (2019) 1940005 [1903.09288].

[96] D. Reitze et al., *Cosmic Explorer: The U.S. Contribution to Gravitational-Wave Astronomy beyond LIGO*, *Bull. Am. Astron. Soc.* **51** (2019) 035 [1907.04833].

[97] L. Badurina et al., *AION: An Atom Interferometer Observatory and Network*, *JCAP* **05** (2020) 011 [1911.11755].

[98] A. Kosowsky, M. S. Turner and R. Watkins, *Gravitational radiation from colliding vacuum bubbles*, *Phys. Rev. D* **45** (1992) 4514.

[99] A. Kosowsky, M. S. Turner and R. Watkins, *Gravitational waves from first order cosmological phase transitions*, *Phys. Rev. Lett.* **69** (1992) 2026.

[100] A. Kosowsky and M. S. Turner, *Gravitational radiation from colliding vacuum bubbles: envelope approximation to many bubble collisions*, *Phys. Rev. D* **47** (1993) 4372 [astro-ph/9211004].

[101] M. Kamionkowski, A. Kosowsky and M. S. Turner, *Gravitational radiation from first order phase transitions*, *Phys. Rev. D* **49** (1994) 2837 [astro-ph/9310044].

[102] M. Hindmarsh, S. J. Huber, K. Rummukainen and D. J. Weir, *Gravitational waves from the sound of a first order phase transition*, *Phys. Rev. Lett.* **112** (2014) 041301 [1304.2433].

[103] J. T. Giblin, Jr. and J. B. Mertens, *Vacuum Bubbles in the Presence of a Relativistic Fluid*, *JHEP* **12** (2013) 042 [1310.2948].

[104] J. T. Giblin and J. B. Mertens, *Gravitional radiation from first-order phase transitions in the presence of a fluid*, *Phys. Rev. D* **90** (2014) 023532 [1405.4005].

[105] A. Kosowsky, A. Mack and T. Kahniashvili, *Gravitational radiation from cosmological turbulence*, *Phys. Rev. D* **66** (2002) 024030 [astro-ph/0111483].

[106] C. Caprini and R. Durrer, *Gravitational waves from stochastic relativistic sources: Primordial turbulence and magnetic fields*, *Phys. Rev. D* **74** (2006) 063521 [astro-ph/0603476].

[107] T. Kahniashvili, A. Kosowsky, G. Gogoberidze and Y. Maravin, *Detectability of Gravitational Waves from Phase Transitions*, *Phys. Rev. D* **78** (2008) 043003 [0806.0293].

[108] T. Kahniashvili, L. Campanelli, G. Gogoberidze, Y. Maravin and B. Ratra, *Gravitational Radiation from Primordial Helical Inverse Cascade MHD Turbulence*, *Phys. Rev. D* **78** (2008) 123006 [0809.1899].

[109] T. Kahniashvili, L. Kisslinger and T. Stevens, *Gravitational Radiation Generated by Magnetic Fields in Cosmological Phase Transitions*, *Phys. Rev. D* **81** (2010) 023004 [0905.0643].

[110] C. Caprini, R. Durrer and G. Servant, *The stochastic gravitational wave background from turbulence and magnetic fields generated by a first-order phase transition*, *JCAP* **12** (2009) 024 [0909.0622].

[111] R. Jinno, T. Konstandin, H. Rubira and I. Stomberg, *Higgsless simulations of cosmological phase transitions and gravitational waves*, *JCAP* **02** (2023) 011 [2209.04369].

[112] D. Bodeker and G. D. Moore, *Can electroweak bubble walls run away?*, *JCAP* **05** (2009) 009 [0903.4099].

[113] D. Bodeker and G. D. Moore, *Electroweak Bubble Wall Speed Limit*, *JCAP* **05** (2017) 025 [1703.08215].

[114] I. Garcia Garcia, G. Koszegi and R. Petrossian-Byrne, *Reflections on Bubble Walls*, 2212.10572.

[115] C. Caprini, R. Durrer and G. Servant, *Gravitational wave generation from bubble collisions in first-order phase transitions: An analytic approach*, *Phys. Rev. D* **77** (2008) 124015 [0711.2593].

[116] S. J. Huber and T. Konstandin, *Gravitational Wave Production by Collisions: More Bubbles*, *JCAP* **09** (2008) 022 [0806.1828].

[117] C. Caprini, R. Durrer, T. Konstandin and G. Servant, *General Properties of the Gravitational Wave Spectrum from Phase Transitions*, *Phys. Rev. D* **79** (2009) 083519 [0901.1661].

[118] T. Konstandin, *Gravitational radiation from a bulk flow model*, *JCAP* **03** (2018) 047 [1712.06869].

[119] M. Hindmarsh, S. J. Huber, K. Rummukainen and D. J. Weir, *Numerical simulations of acoustically generated gravitational waves at a first order phase transition*, *Phys. Rev. D* **92** (2015) 123009 [1504.03291].

[120] M. Hindmarsh, S. J. Huber, K. Rummukainen and D. J. Weir, *Shape of the acoustic gravitational wave power spectrum from a first order phase transition*, *Phys. Rev. D* **96** (2017) 103520 [1704.05871].

[121] M. Lewicki, M. Merchand and M. Zych, *Electroweak bubble wall expansion: gravitational waves and baryogenesis in Standard Model-like thermal plasma*, *JHEP* **02** (2022) 017 [2111.02393].

[122] J. Ellis, M. Lewicki and J. M. No, *On the Maximal Strength of a First-Order Electroweak Phase Transition and its Gravitational Wave Signal*, *JCAP* **04** (2019) 003 [1809.08242].

[123] LIGO Scientific collaboration, *Advanced LIGO*, *Class. Quant. Grav.* **32** (2015) 074001 [1411.4547].

[124] A. M. Polyakov, *Particle Spectrum in Quantum Field Theory*, *JETP Lett.* **20** (1974) 194.

[125] G. 't Hooft, *Magnetic Monopoles in Unified Gauge Theories*, *Nucl. Phys. B* **79** (1974) 276.

[126] T. W. B. Kibble, *Topology of Cosmic Domains and Strings*, *J. Phys. A* **9** (1976) 1387.

[127] W. H. Zurek, *Cosmological Experiments in Superfluid Helium?*, *Nature* **317** (1985) 505.

[128] Y. B. Zeldovich, I. Y. Kobzarev and L. B. Okun, *Cosmological Consequences of the Spontaneous Breakdown of Discrete Symmetry*, *Zh. Eksp. Teor. Fiz.* **67** (1974) 3.

[129] A. Vilenkin, *Gravitational Field of Vacuum Domain Walls and Strings*, *Phys. Rev. D* **23** (1981) 852.

[130] A. Vilenkin, *Cosmic Strings and Domain Walls*, *Phys. Rept.* **121** (1985) 263.

[131] S. E. Larsson, S. Sarkar and P. L. White, *Evading the cosmological domain wall problem*, *Phys. Rev. D* **55** (1997) 5129 [hep-ph/9608319].

[132] J. Preskill, *Cosmological Production of Superheavy Magnetic Monopoles*, *Phys. Rev. Lett.* **43** (1979) 1365.

[133] E. N. Parker, *The Origin of Magnetic Fields*, *Astrophys. J.* **160** (1970) 383.

[134] M. S. Turner, E. N. Parker and T. J. Bogdan, *Magnetic Monopoles and the Survival of Galactic Magnetic Fields*, *Phys. Rev. D* **26** (1982) 1296.

[135] J. Kaplan, P. C. Schuster and N. Toro, *Avoiding an Empty Universe in RS I Models and Large-N Gauge Theories*, hep-ph/0609012.

[136] L. Randall and G. Servant, *Gravitational waves from warped spacetime*, *JHEP* **05** (2007) 054 [hep-ph/0607158].

[137] G. Nardini, M. Quiros and A. Wulzer, *A Confining Strong First-Order Electroweak Phase Transition*, *JHEP* **09** (2007) 077 [0706.3388].

[138] T. Konstandin, G. Nardini and M. Quiros, *Gravitational Backreaction Effects on the Holographic Phase Transition*, *Phys. Rev. D* **82** (2010) 083513 [1007.1468].

[139] T. Konstandin and G. Servant, *Natural Cold Baryogenesis from Strongly Interacting Electroweak Symmetry Breaking*, *JCAP* **07** (2011) 024 [1104.4793].

[140] B. M. Dillon, B. K. El-Menoufi, S. J. Huber and J. P. Manuel, *Rapid holographic phase transition with brane-localized curvature*, *Phys. Rev. D* **98** (2018) 086005 [1708.02953].

[141] B. von Harling and G. Servant, *QCD-induced Electroweak Phase Transition*, *JHEP* **01** (2018) 159 [1711.11554].

[142] S. Bruggisser, B. Von Harling, O. Matsedonskyi and G. Servant, *Baryon Asymmetry from a Composite Higgs Boson*, *Phys. Rev. Lett.* **121** (2018) 131801 [1803.08546].

[143] S. Bruggisser, B. Von Harling, O. Matsedonskyi and G. Servant, *Electroweak Phase Transition and Baryogenesis in Composite Higgs Models*, *JHEP* **12** (2018) 099 [1804.07314].

[144] E. Megías, G. Nardini and M. Quirós, *Cosmological Phase Transitions in Warped Space: Gravitational Waves and Collider Signatures*, *JHEP* **09** (2018) 095 [1806.04877].

[145] D. Bunk, J. Hubisz and B. Jain, *A Perturbative RS I Cosmological Phase Transition*, *Eur. Phys. J. C* **78** (2018) 78 [1705.00001].

[146] P. Baratella, A. Pomarol and F. Rompineve, *The Supercooled Universe*, *JHEP* **03** (2019) 100 [1812.06996].

[147] K. Agashe, P. Du, M. Ekhterachian, S. Kumar and R. Sundrum, *Cosmological Phase Transition of Spontaneous Confinement*, *JHEP* **05** (2020) 086 [1910.06238].

[148] K. Fujikura, Y. Nakai and M. Yamada, *A more attractive scheme for radion stabilization and supercooled phase transition*, *JHEP* **02** (2020) 111 [1910.07546].

[149] A. Azatov and M. Vanvlasselaer, *Phase transitions in perturbative walking dynamics*, *JHEP* **09** (2020) 085 [2003.10265].

[150] E. Megias, G. Nardini and M. Quiros, *Gravitational Imprints from Heavy Kaluza-Klein Resonances*, *Phys. Rev. D* **102** (2020) 055004 [2005.04127].

[151] K. Agashe, P. Du, M. Ekhterachian, S. Kumar and R. Sundrum, *Phase Transitions from the Fifth Dimension*, *JHEP* **02** (2021) 051 [2010.04083].

[152] B. Hassanain, J. March-Russell and M. Schvellinger, *Warped Deformed Throats have Faster (Electroweak) Phase Transitions*, *JHEP* **10** (2007) 089 [0708.2060].

[153] P. Meade and H. Ramani, *Unrestored Electroweak Symmetry*, *Phys. Rev. Lett.* **122** (2019) 041802 [1807.07578].

[154] I. Baldes and G. Servant, *High scale electroweak phase transition: baryogenesis \& symmetry non-restoration*, *JHEP* **10** (2018) 053 [1807.08770].

[155] A. Glioti, R. Rattazzi and L. Vecchi, *Electroweak Baryogenesis above the Electroweak Scale*, *JHEP* **04** (2019) 027 [1811.11740].

[156] O. Matsedonskyi and G. Servant, *High-Temperature Electroweak Symmetry Non-Restoration from New Fermions and Implications for Baryogenesis*, *JHEP* **09** (2020) 012 [2002.05174].

[157] P. Langacker and S.-Y. Pi, *Magnetic Monopoles in Grand Unified Theories*, *Phys. Rev. Lett.* **45** (1980) 1.

[158] P. Salomonson, B. S. Skagerstam and A. Stern, *On the Primordial Monopole Problem in Grand Unified Theories*, *Phys. Lett. B* **151** (1985) 243.

[159] G. R. Dvali, A. Melfo and G. Senjanovic, *Is There a monopole problem?*, *Phys. Rev. Lett.* **75** (1995) 4559 [hep-ph/9507230].

[160] G. R. Dvali and G. Senjanovic, *Is there a domain wall problem?*, *Phys. Rev. Lett.* **74** (1995) 5178 [hep-ph/9501387].

[161] R. N. Mohapatra and G. Senjanovic, *Soft CP Violation at High Temperature*, *Phys. Rev. Lett.* **42** (1979) 1651.

[162] R. N. Mohapatra and G. Senjanovic, *Broken Symmetries at High Temperature*, *Phys. Rev. D* **20** (1979) 3390.

[163] J. Orloff, *The UV price for symmetry nonrestoration*, *Phys. Lett. B* **403** (1997) 309 [hep-ph/9611398].

[164] N. Chai, S. Chaudhuri, C. Choi, Z. Komargodski, E. Rabinovici and M. Smolkin, *Thermal Order in Conformal Theories*, *Phys. Rev. D* **102** (2020) 065014 [2005.03676].

[165] M. Nee, *Meso-tuned WIMPs and Avoided Deconfinement*, 2211.07662.

[166] D. J. H. Chung, E. W. Kolb and A. Riotto, *Production of massive particles during reheating*, *Phys. Rev. D* **60** (1999) 063504 [hep-ph/9809453].

[167] G. F. Giudice, E. W. Kolb and A. Riotto, *Largest temperature of the radiation era and its cosmological implications*, *Phys. Rev. D* **64** (2001) 023508 [hep-ph/0005123].

[168] E. W. Kolb, A. Notari and A. Riotto, *On the reheating stage after inflation*, *Phys. Rev. D* **68** (2003) 123505 [hep-ph/0307241].

[169] N. Fornengo, A. Riotto and S. Scopel, *Supersymmetric dark matter and the reheating temperature of the universe*, *Phys. Rev. D* **67** (2003) 023514 [hep-ph/0208072].

[170] V. Berezinsky, M. Kachelriess and M. A. Solberg, *Supersymmetric superheavy dark matter*, *Phys. Rev. D* **78** (2008) 123535 [0810.3012].

[171] B. Feldstein, M. Ibe and T. T. Yanagida, *Hypercharged Dark Matter and Direct Detection as a Probe of Reheating*, *Phys. Rev. Lett.* **112** (2014) 101301 [1310.7495].

[172] E. W. Kolb and A. J. Long, *Superheavy dark matter through Higgs portal operators*, *Phys. Rev. D* **96** (2017) 103540 [1708.04293].

[173] E. Hardy, *Higgs portal dark matter in non-standard cosmological histories*, *JHEP* **06** (2018) 043 [1804.06783].

[174] M. A. G. Garcia and M. A. Amin, *Prethermalization production of dark matter*, *Phys. Rev. D* **98** (2018) 103504 [1806.01865].

[175] K. Griest and M. Kamionkowski, *Unitarity Limits on the Mass and Radius of Dark Matter Particles*, *Phys. Rev. Lett.* **64** (1990) 615.

[176] J. Smirnov and J. F. Beacom, *TeV-Scale Thermal WIMPs: Unitarity and its Consequences*, *Phys. Rev. D* **100** (2019) 043029 [1904.11503].

[177] C. Charmousis, R. Gregory and V. A. Rubakov, *Wave function of the radion in a brane world*, *Phys. Rev. D* **62** (2000) 067505 [hep-th/9912160].

[178] F. Coradeschi, P. Lodone, D. Pappadopulo, R. Rattazzi and L. Vitale, *A naturally light dilaton*, *JHEP* **11** (2013) 057 [1306.4601].

[179] W. D. Goldberger and M. B. Wise, *Phenomenology of a stabilized modulus*, *Phys. Lett. B* **475** (2000) 275 [hep-ph/9911457].

[180] A. Pomarol, O. Pujolas and L. Salas, *Holographic conformal transition and light scalars*, *JHEP* **10** (2019) 202 [1905.02653].

[181] F. Bigazzi, A. Caddeo, A. L. Cotrone and A. Paredes, *Fate of false vacua in holographic first-order phase transitions*, *JHEP* **12** (2020) 200 [2008.02579].

[182] S. Fichet, *Braneworld effective field theories — holography, consistency and conformal effects*, *JHEP* **04** (2020) 016 [1912.12316].

[183] Z. Chacko, R. K. Mishra, D. Stolarski and C. B. Verhaaren, *Interactions of a Stabilized Radion and Duality*, *Phys. Rev. D* **92** (2015) 056004 [1411.3758].

[184] T. Gherghetta and A. Pomarol, *Bulk fields and supersymmetry in a slice of AdS*, *Nucl. Phys. B* **586** (2000) 141 [hep-ph/0003129].

[185] R. Sundrum, *Gravity's scalar cousin*, hep-th/0312212.

[186] A. Hebecker and J. March-Russell, *Randall-Sundrum II cosmology, AdS / CFT, and the bulk black hole*, *Nucl. Phys. B* **608** (2001) 375 [hep-ph/0103214].

[187] K. Agashe, A. Delgado, M. J. May and R. Sundrum, *RS1, custodial isospin and precision tests*, *JHEP* **08** (2003) 050 [hep-ph/0308036].

[188] S. Casagrande, F. Goertz, U. Haisch, M. Neubert and T. Pfoh, *Flavor Physics in the Randall-Sundrum Model: I. Theoretical Setup and Electroweak Precision Tests*, *JHEP* **10** (2008) 094 [0807.4937].

[189] K. Agashe, G. Perez and A. Soni, *Flavor structure of warped extra dimension models*, *Phys. Rev. D* **71** (2005) 016002 [hep-ph/0408134].

[190] M. Bauer, S. Casagrande, U. Haisch and M. Neubert, *Flavor Physics in the Randall-Sundrum Model: II. Tree-Level Weak-Interaction Processes*, *JHEP* **09** (2010) 017 [0912.1625].

[191] K. Blum, M. Cliche, C. Csaki and S. J. Lee, *WIMP Dark Matter through the Dilaton Portal*, *JHEP* **03** (2015) 099 [1410.1873].

[192] CMS collaboration, *Search for physics beyond the standard model in high-mass diphoton events from proton-proton collisions at $\sqrt{s}$ = 13 TeV*, *Phys. Rev. D* **98** (2018) 092001 [1809.00327].

[193] CMS collaboration, *Combination of searches for Higgs boson pair production in proton-proton collisions at $\sqrt{s}$ = 13 TeV*, *Phys. Rev. Lett.* **122** (2019) 121803 [1811.09689].

[194] G. F. Giudice, Y. Kats, M. McCullough, R. Torre and A. Urbano, *Clockwork/linear dilaton: structure and phenomenology*, *JHEP* **06** (2018) 009 [1711.08437].

[195] F. Abu-Ajamieh, J. S. Lee and J. Terning, *The Light Radion Window*, *JHEP* **10** (2018) 050 [1711.02697].

[196] E. Masso and R. Toldra, *On a light spinless particle coupled to photons*, *Phys. Rev. D* **52** (1995) 1755 [hep-ph/9503293].

[197] J. Jaeckel and M. Spannowsky, *Probing MeV to 90 GeV axion-like particles with LEP and LHC*, *Phys. Lett. B* **753** (2016) 482 [1509.00476].

[198] B. Döbrich, J. Jaeckel, F. Kahlhoefer, A. Ringwald and K. Schmidt-Hoberg, *ALPtraum: ALP production in proton beam dump experiments*, *JHEP* **02** (2016) 018 [1512.03069].

[199] S. Ipek and T. M. P. Tait, *Early Cosmological Period of QCD Confinement*, *Phys. Rev. Lett.* **122** (2019) 112001 [1811.00559].

[200] D. Croon, J. N. Howard, S. Ipek and T. M. P. Tait, *QCD baryogenesis*, *Phys. Rev. D* **101** (2020) 055042 [1911.01432].

[201] D. Berger, S. Ipek, T. M. P. Tait and M. Waterbury, *Dark Matter Freeze Out during an Early Cosmological Period of QCD Confinement*, *JHEP* **07** (2020) 192 [2004.06727].

[202] Y. Cui, M. Lewicki, D. E. Morrissey and J. D. Wells, *Cosmic Archaeology with Gravitational Waves from Cosmic Strings*, *Phys. Rev. D* **97** (2018) 123505 [1711.03104].

[203] Y. Cui, M. Lewicki, D. E. Morrissey and J. D. Wells, *Probing the pre-BBN universe with gravitational waves from cosmic strings*, *JHEP* **01** (2019) 081 [1808.08968].

[204] Y. Watanabe and E. Komatsu, *Improved Calculation of the Primordial Gravitational Wave Spectrum in the Standard Model*, *Phys. Rev. D* **73** (2006) 123515 [astro-ph/0604176].

[205] R. Jinno, T. Moroi and K. Nakayama, *Probing dark radiation with inflationary gravitational waves*, *Phys. Rev. D* **86** (2012) 123502 [1208.0184].

[206] K. Saikawa and S. Shirai, *Primordial gravitational waves, precisely: The role of thermodynamics in the Standard Model*, *JCAP* **05** (2018) 035 [1803.01038].

[207] L. J. Hall, K. Jedamzik, J. March-Russell and S. M. West, *Freeze-In Production of FIMP Dark Matter*, *JHEP* **03** (2010) 080 [0911.1120].

[208] J. McDonald, *Thermally generated gauge singlet scalars as selfinteracting dark matter*, *Phys. Rev. Lett.* **88** (2002) 091304 [hep-ph/0106249].

[209] J. L. Feng, A. Rajaraman and F. Takayama, *Superweakly interacting massive particles*, *Phys. Rev. Lett.* **91** (2003) 011302 [hep-ph/0302215].

[210] K.-Y. Choi and L. Roszkowski, *E-WIMPs*, *AIP Conf. Proc.* **805** (2005) 30 [hep-ph/0511003].

[211] A. Kusenko, *Sterile neutrinos, dark matter, and the pulsar velocities in models with a Higgs singlet*, *Phys. Rev. Lett.* **97** (2006) 241301 [hep-ph/0609081].

[212] K. Petraki and A. Kusenko, *Dark-matter sterile neutrinos in models with a gauge singlet in the Higgs sector*, *Phys. Rev. D* **77** (2008) 065014 [0711.4646].

[213] Y. Mambrini, K. A. Olive, J. Quevillon and B. Zaldivar, *Gauge Coupling Unification and Nonequilibrium Thermal Dark Matter*, *Phys. Rev. Lett.* **110** (2013) 241306 [1302.4438].

[214] F. Elahi, C. Kolda and J. Unwin, *UltraViolet Freeze-in*, *JHEP* **03** (2015) 048 [1410.6157].

[215] P. Gondolo and G. Gelmini, *Cosmic abundances of stable particles: Improved analysis*, *Nucl. Phys. B* **360** (1991) 145.

[216] J. Edsjo and P. Gondolo, *Neutralino relic density including coannihilations*, *Phys. Rev. D* **56** (1997) 1879 [hep-ph/9704361].

[217] S. Davidson, M. Losada and A. Riotto, *A New perspective on baryogenesis*, *Phys. Rev. Lett.* **84** (2000) 4284 [hep-ph/0001301].

[218] P. Agrawal and M. Nee, *Avoided deconfinement in Randall-Sundrum models*, *JHEP* **10** (2021) 105 [2103.05646].

[219] Y. Bai, M. Carena and J. Lykken, *Dilaton-assisted Dark Matter*, *Phys. Rev. Lett.* **103** (2009) 261803 [0909.1319].

[220] A. Ahmed and S. Najjari, *Ultraviolet Freeze-in Dark Matter through the Dilaton Portal*, 2112.14261.

[221] L. Roszkowski, E. M. Sessolo and A. J. Williams, *Prospects for dark matter searches in the pMSSM*, *JHEP* **02** (2015) 014 [1411.5214].

[222] A. Hryczuk, K. Jodlowski, E. Moulin, L. Rinchiuso, L. Roszkowski, E. M. Sessolo et al., *Testing dark matter with Cherenkov light - prospects of H.E.S.S. and CTA for exploring minimal supersymmetry*, *JHEP* **10** (2019) 043 [1905.00315].

[223] L. Rinchiuso, O. Macias, E. Moulin, N. L. Rodd and T. R. Slatyer, *Prospects for detecting heavy WIMP dark matter with the Cherenkov Telescope Array: The Wino and Higgsino*, *Phys. Rev. D* **103** (2021) 023011 [2008.00692].

[224] CTA collaboration, *Sensitivity of the Cherenkov Telescope Array to a dark matter signal from the Galactic centre*, *JCAP* **01** (2021) 057 [2007.16129].

[225] H.E.S.S. collaboration, *Search for dark matter annihilations towards the inner Galactic halo from 10 years of observations with H.E.S.S*, *Phys. Rev. Lett.* **117** (2016) 111301 [1607.08142].

[226] HAWC collaboration, *Dark Matter Limits From Dwarf Spheroidal Galaxies with The HAWC Gamma-Ray Observatory*, *Astrophys. J.* **853** (2018) 154 [1706.01277].

[227] HAWC collaboration, *A Search for Dark Matter in the Galactic Halo with HAWC*, *JCAP* **02** (2018) 049 [1710.10288].

[228] PandaX-II collaboration, *Dark Matter Results From 54-Ton-Day Exposure of PandaX-II Experiment*, *Phys. Rev. Lett.* **119** (2017) 181302 [1708.06917].

[229] PandaX-II collaboration, *Results of dark matter search using the full PandaX-II exposure*, *Chin. Phys. C* **44** (2020) 125001 [2007.15469].

[230] XENON collaboration, *First Dark Matter Search Results from the XENON1T Experiment*, *Phys. Rev. Lett.* **119** (2017) 181301 [1705.06655].

[231] XENON collaboration, *Dark Matter Search Results from a One Ton-Year Exposure of XENON1T*, *Phys. Rev. Lett.* **121** (2018) 111302 [1805.12562].

[232] A. Sommerfeld, *Über die Beugung und Bremsung der Elektronen*, *Annalen Phys.* **403** (1931) 257.

[233] S. Cassel, *Sommerfeld factor for arbitrary partial wave processes*, *J. Phys. G* **37** (2010) 105009 [0903.5307].

[234] T. R. Slatyer, *The Sommerfeld enhancement for dark matter with an excited state*, *JCAP* **02** (2010) 028 [0910.5713].

[235] J. L. Feng, M. Kaplinghat and H.-B. Yu, *Sommerfeld Enhancements for Thermal Relic Dark Matter*, *Phys. Rev. D* **82** (2010) 083525 [1005.4678].

[236] P. J. Steinhardt, *Monopole Dissociation in the Early Universe*, *Phys. Rev. D* **24** (1981) 842.

[237] P. J. Steinhardt, *Monopole and Vortex Dissociation and Decay of the False Vacuum*, *Nucl. Phys. B* **190** (1981) 583.

[238] B. Kumar and U. Yajnik, *Graceful exit via monopoles in a theory with O'Raifeartaigh type supersymmetry breaking*, *Nucl. Phys. B* **831** (2010) 162 [0908.3949].

[239] B. Kumar, M. B. Paranjape and U. A. Yajnik, *Fate of the false monopoles: Induced vacuum decay*, *Phys. Rev. D* **82** (2010) 025022 [1006.0693].

[240] L. G. Jensen and P. J. Steinhardt, *DISSOCIATION OF ABRIKOSOV-NIELSEN-OLESEN VORTICES*, *Phys. Rev. B* **27** (1983) 5549.

[241] U. A. Yajnik, *PHASE TRANSITION INDUCED BY COSMIC STRINGS*, *Phys. Rev. D* **34** (1986) 1237.

[242] U. A. Yajnik and T. Padmanabhan, *ANALYTICAL APPROACH TO STRING INDUCED PHASE TRANSITION*, *Phys. Rev. D* **35** (1987) 3100.

[243] Y. Hosotani, *Impurities in the Early Universe*, *Phys. Rev. D* **27** (1983) 789.

[244] J. Preskill and A. Vilenkin, *Decay of metastable topological defects*, *Phys. Rev. D* **47** (1993) 2324 [hep-ph/9209210].

[245] A. Kusenko, *Phase transitions precipitated by solitosynthesis*, *Phys. Lett. B* **406** (1997) 26 [hep-ph/9705361].

[246] D. Metaxas, *Nontopological solitons as nucleation sites for cosmological phase transitions*, *Phys. Rev. D* **63** (2001) 083507 [hep-ph/0009225].

[247] L. Pearce, *Solitosynthesis induced phase transitions*, *Phys. Rev. D* **85** (2012) 125022 [1202.0873].

[248] W. A. Hiscock, *CAN BLACK HOLES NUCLEATE VACUUM PHASE TRANSITIONS?*, *Phys. Rev. D* **35** (1987) 1161.

[249] V. A. Berezin, V. A. Kuzmin and I. I. Tkachev, *O(3) Invariant Tunneling in General Relativity*, *Phys. Lett. B* **207** (1988) 397.

[250] P. B. Arnold, *GRAVITY AND FALSE VACUUM DECAY RATES: O(3) SOLUTIONS*, *Nucl. Phys. B* **346** (1990) 160.

[251] V. A. Berezin, V. A. Kuzmin and I. I. Tkachev, *Black holes initiate false vacuum decay*, *Phys. Rev. D* **43** (1991) 3112.

[252] R. Gregory, I. G. Moss and B. Withers, *Black holes as bubble nucleation sites*, *JHEP* **03** (2014) 081 [1401.0017].

[253] D. Canko, I. Gialamas, G. Jelic-Cizmek, A. Riotto and N. Tetradis, *On the Catalysis of the Electroweak Vacuum Decay by Black Holes at High Temperature*, *Eur. Phys. J. C* **78** (2018) 328 [1706.01364].

[254] A. Shkerin and S. Sibiryakov, *Black hole induced false vacuum decay from first principles*, *JHEP* **11** (2021) 197 [2105.09331].

[255] P. Burda, R. Gregory and I. Moss, *Gravity and the stability of the Higgs vacuum*, *Phys. Rev. Lett.* **115** (2015) 071303 [1501.04937].

[256] P. Burda, R. Gregory and I. Moss, *Vacuum metastability with black holes*, *JHEP* **08** (2015) 114 [1503.07331].

[257] P. Burda, R. Gregory and I. Moss, *The fate of the Higgs vacuum*, *JHEP* **06** (2016) 025 [1601.02152].

[258] K. Mukaida and M. Yamada, *False Vacuum Decay Catalyzed by Black Holes*, *Phys. Rev. D* **96** (2017) 103514 [1706.04523].

[259] K. Kohri and H. Matsui, *Electroweak Vacuum Collapse induced by Vacuum Fluctuations of the Higgs Field around Evaporating Black Holes*, *Phys. Rev. D* **98** (2018) 123509 [1708.02138].

[260] N. Oshita, M. Yamada and M. Yamaguchi, *Compact objects as the catalysts for vacuum decays*, *Phys. Lett. B* **791** (2019) 149 [1808.01382].

[261] R. Balkin, J. Serra, K. Springmann, S. Stelzl and A. Weiler, *Density Induced Vacuum Instability*, 2105.13354.

[262] M. K. Prasad and C. M. Sommerfield, *An Exact Classical Solution for the 't Hooft Monopole and the Julia-Zee Dyon*, *Phys. Rev. Lett.* **35** (1975) 760.

[263] M. G. Abed and I. G. Moss, *Bubble nucleation at zero and nonzero temperatures*, 2006.06289.

[264] A. Ambrosetti and P. H. Rabinowitz, *Dual variational methods in critical point theory and applications*, *Journal of Functional Analysis* **14** (1973) 349.

[265] H. Murayama and J. Shu, *Topological Dark Matter*, *Phys. Lett. B* **686** (2010) 162 [0905.1720].

[266] G. Johnson and J. March-Russell, *Hawking Radiation of Extended Objects*, *JHEP* **04** (2020) 205 [1812.10500].

[267] I. K. Affleck and N. S. Manton, *Monopole Pair Production in a Magnetic Field*, *Nucl. Phys. B* **194** (1982) 38.

[268] A. K. Drukier and S. Nussinov, *Monopole Pair Creation in Energetic Collisions: Is It Possible?*, *Phys. Rev. Lett.* **49** (1982) 102.

[269] S. Das and A. Hook, *Black hole production of monopoles in the early universe*, *JHEP* **12** (2021) 145 [2109.00039].

[270] D. Buttazzo, G. Degrassi, P. P. Giardino, G. F. Giudice, F. Sala, A. Salvio et al., *Investigating the near-criticality of the Higgs boson*, *JHEP* **12** (2013) 089 [1307.3536].

[271] M. Geller, A. Hook, R. Sundrum and Y. Tsai, *Primordial Anisotropies in the Gravitational Wave Background from Cosmological Phase Transitions*, *Phys. Rev. Lett.* **121** (2018) 201303 [1803.10780].

[272] J. McDonald, *Gauge singlet scalars as cold dark matter*, *Phys. Rev. D* **50** (1994) 3637 [hep-ph/0702143].

[273] C. P. Burgess, M. Pospelov and T. ter Veldhuis, *The Minimal model of nonbaryonic dark matter: A Singlet scalar*, *Nucl. Phys. B* **619** (2001) 709 [hep-ph/0011335].

[274] J. R. Espinosa and M. Quiros, *Novel Effects in Electroweak Breaking from a Hidden Sector*, *Phys. Rev. D* **76** (2007) 076004 [hep-ph/0701145].

[275] S. Profumo, M. J. Ramsey-Musolf and G. Shaughnessy, *Singlet Higgs phenomenology and the electroweak phase transition*, *JHEP* **08** (2007) 010 [0705.2425].

[276] V. Barger, P. Langacker, M. McCaskey, M. J. Ramsey-Musolf and G. Shaughnessy, *LHC Phenomenology of an Extended Standard Model with a Real Scalar Singlet*, *Phys. Rev. D* **77** (2008) 035005 [0706.4311].

[277] J. R. Espinosa, T. Konstandin, J. M. No and M. Quiros, *Some Cosmological Implications of Hidden Sectors*, *Phys. Rev. D* **78** (2008) 123528 [0809.3215].

[278] J. R. Espinosa, T. Konstandin and F. Riva, *Strong Electroweak Phase Transitions in the Standard Model with a Singlet*, *Nucl. Phys. B* **854** (2012) 592 [1107.5441].

[279] J. M. Cline and K. Kainulainen, *Electroweak baryogenesis and dark matter from a singlet Higgs*, *JCAP* **01** (2013) 012 [1210.4196].

[280] S. Profumo, M. J. Ramsey-Musolf, C. L. Wainwright and P. Winslow, *Singlet-catalyzed electroweak phase transitions and precision Higgs boson studies*, *Phys. Rev. D* **91** (2015) 035018 [1407.5342].

[281] L. Feng, S. Profumo and L. Ubaldi, *Closing in on singlet scalar dark matter: LUX, invisible Higgs decays and gamma-ray lines*, *JHEP* **03** (2015) 045 [1412.1105].

[282] D. Curtin, P. Meade and C.-T. Yu, *Testing Electroweak Baryogenesis with Future Colliders*, *JHEP* **11** (2014) 127 [1409.0005].

[283] N. Craig, H. K. Lou, M. McCullough and A. Thalapillil, *The Higgs Portal Above Threshold*, *JHEP* **02** (2016) 127 [1412.0258].

[284] P. Huang, A. J. Long and L.-T. Wang, *Probing the Electroweak Phase Transition with Higgs Factories and Gravitational Waves*, *Phys. Rev. D* **94** (2016) 075008 [1608.06619].

[285] V. Vaskonen, *Electroweak baryogenesis and gravitational waves from a real scalar singlet*, *Phys. Rev. D* **95** (2017) 123515 [1611.02073].

[286] G. Kurup and M. Perelstein, *Dynamics of Electroweak Phase Transition In Singlet-Scalar Extension of the Standard Model*, *Phys. Rev. D* **96** (2017) 015036 [1704.03381].

[287] D. Buttazzo, D. Redigolo, F. Sala and A. Tesi, *Fusing Vectors into Scalars at High Energy Lepton Colliders*, *JHEP* **11** (2018) 144 [1807.04743].

[288] T. Alanne, T. Hugle, M. Platscher and K. Schmitz, *A fresh look at the gravitational-wave signal from cosmological phase transitions*, *JHEP* **03** (2020) 004 [1909.11356].

[289] S. Blasi and A. Mariotti, *Domain walls seeding the electroweak phase transition*, 2203.16450.

[290] A. Katz and M. Perelstein, *Higgs Couplings and Electroweak Phase Transition*, *JHEP* **07** (2014) 108 [1401.1827].

[291] H. Casini and S. Sarkar, *No cosmological domain wall problem for weakly coupled fields*, *Phys. Rev. D* **65** (2002) 025002 [hep-ph/0106272].

[292] C. L. Wainwright, *CosmoTransitions: Computing Cosmological Phase Transition Temperatures and Bubble Profiles with Multiple Fields*, *Comput. Phys. Commun.* **183** (2012) 2006 [1109.4189].

[293] P. Agrawal and M. Nee, *The Boring Monopole*, *SciPost Phys.* **13** (2022) 049 [2202.11102].

[294] S. Blasi, R. Jinno, T. Konstandin, H. Rubira and I. Stomberg, *Gravitational waves from defect-driven phase transitions: domain walls*, 2302.06952.

[295] J. Ellis, M. Lewicki and V. Vaskonen, *Updated predictions for gravitational waves produced in a strongly supercooled phase transition*, *JCAP* **11** (2020) 020 [2007.15586].

[296] J. R. Espinosa, T. Konstandin, J. M. No and G. Servant, *Energy Budget of Cosmological First-order Phase Transitions*, *JCAP* **06** (2010) 028 [1004.4187].

[297] P. J. Steinhardt, *Relativistic Detonation Waves and Bubble Growth in False Vacuum Decay*, *Phys. Rev. D* **25** (1982) 2074.

[298] E. Thrane and J. D. Romano, *Sensitivity curves for searches for gravitational-wave backgrounds*, *Phys. Rev. D* **88** (2013) 124032 [1310.5300].

[299] J. Barzilai and J. M. Borwein, *Two-Point Step Size Gradient Methods*, *IMA Journal of Numerical Analysis* **8** (1988) 141.